UNIVERSITY OF CALIFORNIA SAN DIEGO

High-speed optical signal processing and detection: Toward efficient dispersion-engineered parametric devices controlled by few photons

A dissertation submitted in partial satisfaction of the
requirements for the degree Doctor of Philosophy

in

Electrical Engineering (Photonics)

by

Ana Pejkic

Committee in charge:

Professor Stojan Radic, Chair
Professor Dimitri Basov
Professor Vitaliy Lomakin
Professor Shayan Mookherjea
Professor Oleg Shpyrko

2015

The Dissertation of Ana Pejkic is approved, and it is acceptable in quality and form for publication on microfilm and electronically:

_____

_____

_____

_____

_____

Chair

University of California, San Diego

2015

DEDICATION

To my parents for a lifetime of love and support

And my beloved husband Miroslav for his luminous presence

TABLE OF CONTENTS

LIST OF FIGURES

LIST OF TABLES

LIST OF ABBREVIATIONS

IT	Internet Technology
OEO	Optical-electrical-optical
NIR	Near-infrared
NLS	Nonlinear Schrodinger
SPM	Self-phase modulation
XPM	Cross-phase modulation
FWM	Four wave mixing
FOPA	Fiber optical parametric amplifier
ZDW	Zero-dispersion wavelength
EC	External cavity
HNLF	Highly nonlinear fiber
OBPF	Optical band-pass filter
PD	Photodiode
FPM	Fiber parametric mixer
CW	Continuous wave
OSNR	Optical signal-to-noise ratio
ER	Extinction ratio
OSO	Optical sampling oscilloscope
MLL	Mode-locked laser
VOA	Variable optical attenuator

BER	Bit-error ratio
PRBS	Pseudo-random bit sequence
EDFA	Erbium-doped fiber amplifier
SNR	Signal-to-noise ratio
ROC	Receiver operating characteristics
SWIR	Short-wave-infrared

ACKNOWLEDGEMENTS

My sincere appreciation goes to many people who have helped in many ways in the completion of this dissertation. First, I owe my deepest gratitude to my advisor, Professor Stojan Radic, for support and understanding. His admirable scientific knowledge and endless motivation have inspired me to strive towards excellence. The balance of providing intellectual freedom and guidance have helped me reaching my full potential.

I would also like to thank other committee members, Professor Dimitri Basov, Professor Vitaliy Lomakin, Professor Shayan Mookherjea and Professor Oleg Shpyrko for their insightful comments, suggestions and dedicated time.

I am grateful to the Department of Electrical and Computer Engineering, University of California San Diego for providing the financial support over the past five years. I am also pleased to acknowledge the support of Intelligence Advance Research Project Agency for providing the funding for this work.

Numerous colleagues at the Photonic Systems Group: those who have taken different paths (Jose M. Chavez Boggio, Slaven Moro, Camille S. Bres, Sanja Zlatanovic, Zhi Tong, Faezeh Gholami, Ron R. Nissim and Lan Liu) and current members (Nikola Alic, Andreas O. J. Wiberg, Evgeny Myslivets, Bill P.-P. Kuo, Vahid Ataie, Daniel Esman, Kevin Young, Christopher K. Huynh, Eduardo Temprana, Motohiko Eto and Jin Zhang), who have been a source of much encouragement and constructive criticism - I am eternally indebted to.

Finally, my heartfelt appreciation goes to my family and friends who made this journey so much more enjoyable. Above all, I want to thank my beloved husband Miroslav for being an eternal source of joy and laughter.

Chapter 3, in part is a reprint of the material as it appears in the IEEE/OSA Journal of Lightwave Technology, volume 33, issue 24, 1-7 (2015), titled "Directional Phase-Matched Interaction in the Saturated Parametric Mixer" by Ana Pejkic, Ron R. Nissim, Evgeny Myslivets, Andreas O. J. Wiberg, Nikola Alic, and Stojan Radic. Chapter 3 also contains in part material submitted for publication as it may appear in the Progress of Quantum Electronics, titled "High speed parametric processing controlled by few photons," by Ana Pejkic, and Stojan Radic. The dissertation author was the primary investigator, and the primary author of these articles.

Chapter 4, in part is a reprint of the material as it appears in the IEEE/OSA Journal of Lightwave Technology, volume 33, issue 24, 1-7 (2015), titled "Directional Phase-Matched Interaction in the Saturated Parametric Mixer" by Ana Pejkic, Ron R. Nissim, Evgeny Myslivets, Andreas O. J. Wiberg, Nikola Alic, and Stojan Radic. Chapter 4, also contains in part material submitted for publication as it may appear in the Progress of Quantum Electronics, titled "High speed parametric processing controlled by few photons," by Ana Pejkic and Stojan Radic. The dissertation author was the primary investigator, and the primary author of these articles. Lastly, Chapter 4 in part is a reprint of the material as it appears in the Science Journal, volume 345, issue 6195,417-419 (2014), titled "Ultrafast optical control by few photons in engineered fiber" by Ron R. Nissim, Ana Pejkic, Evgeny Myslivets, Bill P.-P. Kuo, Nikola Alic,

and Stojan Radic. The dissertation author was the primary investigator, and the co-primary author of this article.

Chapter 5, in part is a reprint of the material as it appears in the IEEE/OSA Journal of Lightwave Technology, volume 33, issue 24, 1-7 (2015), titled "Directional Phase-Matched Interaction in the Saturated Parametric Mixer" by Ana Pejkic, Ron R. Nissim, Evgeny Myslivets, Andreas O. J. Wiberg, Nikola Alic, and Stojan Radic. Chapter 5, also contains in part material presented at the Optical Fiber Communication Conference 2015, paper W1K.2, titled "A study of a parametric mixer non-reciprocity dependence on the pump wavelength" by Ana Pejkic, Ron R. Nissim, Evgeny Myslivets, Andreas O. J. Wiberg, Nikola Alic, and Stojan Radic. Chapter 5 includes in part material that has been submitted for publication as it may appear in the Progress of Quantum Electronics, titled "High speed parametric processing controlled by few photons," by Ana Pejkic and Stojan Radic. The dissertation author was the primary investigator, and a primary author of the journal papers and was the presenter of the conference contribution. Lastly, Chapter 5 in part is a reprint of the material as it appears in the Science Journal, volume 345, issue 6195,417-9 (2014), titled "Ultrafast optical control by few photons in engineered fiber" by Ron R. Nissim, Ana Pejkic, Evgeny Myslivets, Bill P.-P. Kuo, Nikola Alic, and Stojan Radic. The dissertation author was the primary investigator, and the co-primary author of this article.

Chapter 6, in part is a reprint of the material as it appears in the Optics Express Journal, volume 22, issue 19, 23512-23527 (2014), titled "All-optical switching in a highly efficient parametric fiber mixer: design study" by Ana Pejkic, Ron R. Nissim, Evgeny Myslivets, Andreas O. J. Wiberg, Nikola Alic, and Stojan Radic. Chapter 6, in

part is currently being prepared for submission for publication of the material by Ana Pejkic, Evgeny Myslivets, Nikola Alic and Stojan Radic. The dissertation author was the primary investigator, and the primary author of these articles.

Chapter 7, in part or in full is currently being prepared for submission for publication of the material by Ana Pejkic, Daniel. J. Esman, Andreas O. J. Wiberg, Nikola Alic and Stojan Radic. The dissertation author was the primary investigator, and the primary author of this article.

VITA

2010	Bachelor of Science, Physics (Applied Physics and Informatics), University of Belgrade, Belgrade, Serbia.
2012	Master of Science, Electrical Engineering (Photonics), University of California, San Diego, USA.
2015	Doctor of Philosophy, Electrical Engineering (Photonics), University of California, San Diego, USA.

PUBLICATIONS

Journal articles:

Ana Pejkic, and Stojan Radic, "High speed parametric processing controlled by few photons," Progress in Quantum Electronics, 44, 01-13 (2015). Advanced online publication: DOI:10.1016/j.pquantelec.2015.08.002.

Ana Pejkic, Ron R. Nissim, Evgeny Myslivets, Andreas O. J. Wiberg, Nikola Alic, and Stojan Radic, "Directional phase-matched interaction in the saturated parametric mixer," Journal of Lightwave Technology, 33(24), 01-7 (2015). Advanced online publication: DOI: 10.1109/JLT.2015.2461537.

Ron R. Nissim, **Ana Pejkic**, Evgeny Myslivets, Nikola Alic , and Stojan Radic, "Origin of non-reciprocal response in fiber optic parametric amplifiers," Journal of Lightwave Technology, 33(2), 495 (2015).

Ana Pejkic, Evgeny Myslivets, Nikola Alic, and Stojan Radic, "Error-free performance of a low energy switch with 100 GHz operating speed," (in preparation).

Ana Pejkic, Daniel J. Esman, Andreas O. J. Wiberg, Nikola Alic, and Stojan Radic, "Photonic sampler aided few photon detection at 10 GB/s and beyond," (in preparation).

Ana Pejkic, Ron Nissim, Evgeny Myslivets, Andreas O.J. Wiberg, Nikola Alic and Stojan Radic, "All-optical switching in highly efficient parametric fiber mixer: design study," Optics Express, 22(19) (2014).

Ron Nissim*, **Ana Pejkic***, Evgeny Myslivets, Bill P. Kuo, Nikola Alic, and Stojan Radic, "Ultrafast optical control by few photons in engineered fiber," Science 345(6195), 417–419 (2014).
*These authors have contributed equally to this work

Slaven Moro, **Ana Peric**, Nikola Alic, Arthur A. J. Anderson, Colin J. McKinstrie, and Stojan Radic, "Continuous-wave parametric amplifier with 6.9-ExaHz gain-bandwidth product," IEEE Photon. Techn. Lett. 23, 1532-1534 (2011).

Bill P.-P. Kuo, Evgeny Myslivets, Andreas O. J. Wiberg, Sanja Zlatanovic, Camille-Sophie Brès, Slaven Moro, Faezeh Gholami, **Ana Peric**, Nikola Alic, and Stojan Radic, "Transmission of 640-Gb/s RZ-OOK channel over 100-km SSMF by wavelength-transparent conjugation," *IEEE/OSA* J. Lightwave Technol. 29, 516-523 (2011).

Slaven Moro, **Ana Peric**, Nikola Alic, Bryan Stossel, and Stojan Radic, "Phase noise in fiber-optic parametric amplifiers and converters and its impact on sensing and communication systems," Opt. Express 18, 21449-21460 (2010).

Conference proceedings:

Ana Pejkic, Ron R. Nissim, Evgeny Myslivets, Andreas O. J. Wiberg, Nikola Alic, and Stojan Radic, "A study of a saturated parametric mixer non-reciprocity dependence on the pump wavelength," in Optical Fiber Communication Conference, Los Angeles (2015).

Eduardo Temprana, Vahid Ataie, **Ana Peric**, Nikola Alic and Stojan Radic, "Wavelength conversion of QPSK signals in single-pump FOPA with 20 dB conversion efficiency," in Optical Fiber Communication Conference (2013).

Ana Peric, Slaven Moro, Nikola Alic, Arthur J. Anderson, Colin J. McKinstrie and Stojan Radic, "Two-pump fiber-optic parametric amplifier with 66dB gain and errorless performance," in Frontiers in Optics Conference, (2010).

Slaven Moro, **Ana Peric**, Nikola Alic, Bryan Stossel, and Stojan Radic, "Spectral dependence of nonlinear phase noise in one-pump fiber-optic parametric amplifiers," Photonics Society Summer Topical Meeting Series (2010).

Slaven Moro, **Ana Peric**, Nikola Alic, Bryan Stossel, and Stojan Radic, "Nonlinear phase noise in one-pump fiber-optic parametric amplifiers," in Latin America Optics and Photonics Conference, OSA Technical Digest (CD) (Optical Society of America, 2010), paper ThD4.

Slaven Moro, **Ana Peric**, Nikola Alic, Colin J. McKinstrie, and S. Radic, "Experimental demonstration of a low-noise-figure phase-insensitive parametric amplifier," IEEE Photonics Society 2010 Annual Meeting, Denver, CO, paper WN3 (2010).

Evgeny Myslivets, Bill P.-P. Kuo, Andreas O. J. Wiberg, Sanja Zlatanovic, Slaven Moro, Faezeh Gholami, **Ana Peric**, Camille-Sophie Brès, Nikola Alic, and Stojan Radic, "Transmission of 640 Gbps RZ-OOK channel over 100 km of SSMF by wavelength-transparent conjugation," in Optical Fiber Communication Conference, OSA Technical Digest (CD) (Optical Society of America, 2010), post deadline paper PDPC6.

ABSTRACT OF THE DISSERTATION

High-speed optical signal processing and detection: Toward efficient dispersion-engineered parametric devices controlled by few photons

by

Ana Pejkic

Doctor of Philosophy in Electrical Engineering (Photonics)

University of California, San Diego, 2015

Professor Stojan Radic, Chair

In this Internet era, rapid transitioning of many aspects of medical, defense and commercial applications to digital platforms dictates their heavy reliance on optical communication systems. This trend places severe challenges on contemporary

communication systems, expected to provide wide-bandwidth services and high degree of information security, with minimum energy dissipation. To meet the rising bandwidth demand, current bandwidth limited technology requires implementation of parallel processing; however, energy dissipation of such a system is globally and environmentally significant. A solution to this problem is envisioned in a form of an optical processor, a device recognized for its high speed, low loss and signal quality preservation. In this dissertation we investigate two optical processor roles: direct signal processing role (all-optical switching) and preprocessing role in preamplified few photon detection.

In the direct signal processing role, an optical switch controls the state of one wave by a low-energy control signal. It is realized in a highly nonlinear fiber, a medium acclaimed for its inherent femtosecond response time, a low loss and a high figure of merit. The switching functionality is implemented by employing the four wave mixing process in the depleted pump regime. To maximize the energy exchange, we revisit the saturated parametric mixer phase matching condition and propose a novel dispersion engineering method enhancing the performance. This study advances the understanding of the phase-matched interaction in the saturated parametric mixer and enables the first realization of a few-photon controlled silica-fiber-based device.

In the preprocessing role, the all-fiber photonic sampler is implemented prior to detection of a preamplified few photon signal with a low duty cycle; the sampler function is limited to amplified spontaneous emission noise alleviation. The proposed few photon detection method shows an order of magnitude improvement in the Bit

Error Ratio and detection efficiency with respect to conventional preamplified receiver, and operates at speed beyond the reach of current single photon detector technology.

1. Introduction

1.1. The photon

The history of the term "photon" is as interesting as the science behind the quantum of electromagnetic radiation [1]. It was introduced long before 1920 in the field of visual science and psychology, with no known relations to the quantum of electromagnetic radiation. The photon concept, on the other hand, was pioneered by Planck in 1900 in an attempt to explain the blackbody spectra [2] and adapted by Einstein in 1905 who further ascribed a role of an "energy quanta" of free, monochromatic electromagnetic radiation to it. Neither Planck nor Einstein used the term "photon" in their theories. It was Lewis who introduced it in 1926, however, with no connection to Einstein's "energy quanta". Einstein's theory was largely unaccepted in the scientific community, even though it provided an explanation for the photoelectric effect; however experiments in X-ray scattering and Dirac's quantum theory of radiation provided the confirmation of the theory and linked the term "photon" to the quantum of electromagnetic radiation concept.

The modern particle physics associates the photon to an elementary particle, the one whose substructure is unknown and unpredicted by any existing theory. According to the Standard model, elementary particles are divided into two groups: fermions, the matter constituents, and bosons, the field particles mediating the interaction among fermions. Elementary particles are divided by their fundamental properties: the charge, the spin and the mass. This is the origin of a key distinction between an

electron and a photon. Namely, an electron, as a fermion particle, has the spin of 1/2, the mass of $9.1.10^{-31}$kg, the charge of -1 and a positron as an antiparticle. Because of its charge, electrons can interact via electromagnetic interaction. Photons, on the other hand, are bosons, having an integer spin value of 1, no mass, no charge and themselves as antiparticles. As a charge-free particle, photons in the vacuum cannot interact [3], but they can interact by means of a nonlinear medium. These fundamental differences between the two particles have, to date, limited their deployment in modern technology: we use photons to transmit information in an optical fiber, and electrons to process the signal.

1.2. The Internet era

As witnesses of rapid technological developments, we can observe how our everyday lives are being reshaped constantly. Where only seven decades ago computer deployment was limited to military, government, universities and large corporations, today these technologies are an integral part of almost every household. One of the world's first general-purpose electronic computers, Electronic Numerical Integrator and Computer (ENIAC), weighted over 25 tons with an area of approximately 680 square feet, consumed about 160 kW of power and was priced $500,000 (corresponding to about $6,000,000 today, adjusted for inflation) [4]. With the invention of the transistor in 1947, development of integrated circuits in late 1950s and fast technological advances in the following years, computers became smaller and more affordable [5],[6] (See Figure 1.1).

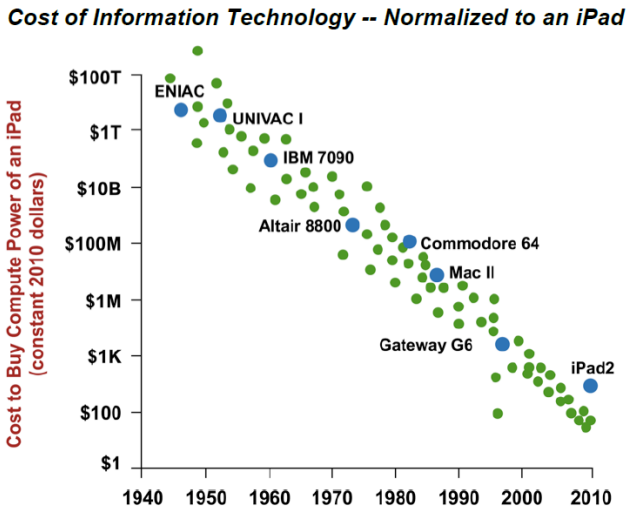

Figure 1.1: Cost of computers as a function of time - normalized to and iPad **[7]**,**[8]**.

Fast progress in the hardware technology has driven the growth of the software technology and the Internet. These advances have affected every aspect of human life: from communication, through education and businesses to entertainment.

Where only five decades ago, communication media were limited to oral, telephone and traditional mail [5], today people mostly communicate by mobile telephones and the internet technology (IT). Indeed, the IT has already penetrated into every pore of our system. In view of the modern educational systems, online homework, tests, grading, reading material and communication with instructor via e-mail are among its central parts. Another aspect of the contemporary education is increasing interest in affordable online classes, where video-based lectures are delivered over the Internet [9], [10]. With new scientific advances, our education system is likely to continue evolving to meet all our needs.

Large corporations were among the first experiencing substantial transformation with the availability of the Internet technology [5]. While personal meeting is still the preferred way of business communication, it is, nevertheless, often replaced with video conference call or telephone conference call. The traditional letters typed by a typewriter are now replaced with e-mail and computers. Novel applications such as cloud computing, provide dependable, consistent and inexpensive access to advance computational capacity, but rely heavily on the broadband Internet connection. With all this in mind, corporations are expected to continue exploiting the benefits of modern technological advances.

Following the technological trends, even the way people entertain is similarly altered as the aforementioned aspects of our lives. Online gaming, online shopping, social networking, "Internet of Things", video on demand and 3D high-definition television are among numerous ways the IT have transformed the way we connect and entertain. Moreover, as the availability and the affordability of variety of electronic devices becomes prevalent, the number of (Internet) connected devices per user is increasing, reaching 2.9 in the United States in 2014 [11]. Surrounded by the fruits of the technological advances, an average user is rarely familiar with consequences of such a multi-device communication-, study-, work- and entertainment-routine and its impact on modern communication systems and energy dissipation. In the following section, I attempt to familiarize the reader with trends and challenges in the modern communication systems and their potential evolution paths.

1.3. Trends and challenges in modern information and telecommunication networks

Our growing desire to communicate, connect and entertain is continuously shaping optical communication networks. According to recent forecast prepared by Cisco [12], Internet traffic has increased five-fold in the past 5 years, while three-fold increase is expected in the next three years; the busiest traffic in 60 minutes per day is likely to increase at even higher rate. Global Internet traffic of 100 GB per day in 1992. is expected to reach 400 Tb/s by 2018, the latter being simply restated by Cisco [12] as "the equivalent of 148 million people streaming Internet HD video simultaneously, all day, every day".

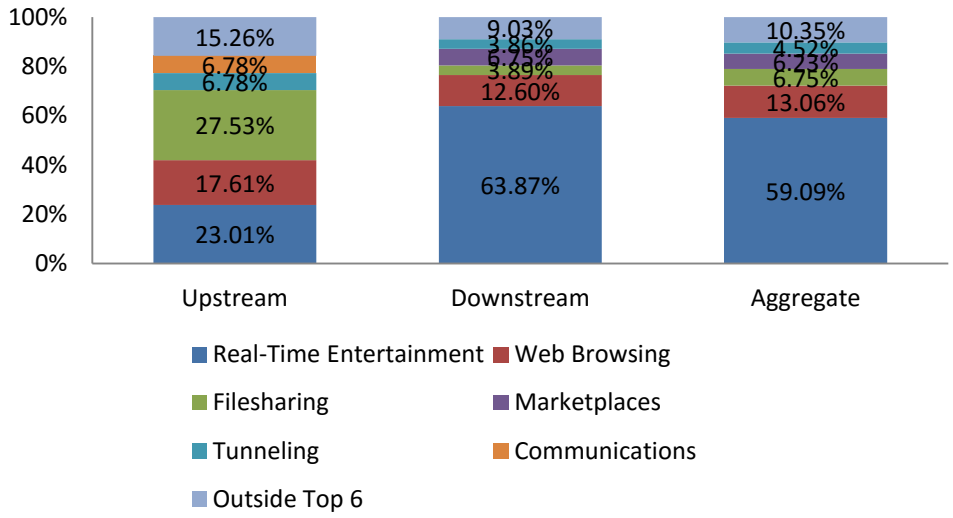

Figure 1.2: Peak period Internet traffic composition. North America **[13]**

It is clear from Figure 1.2 that a large portion of this traffic is attributed to the wide-bandwidth real time services, such as video on demand or cloud computing.

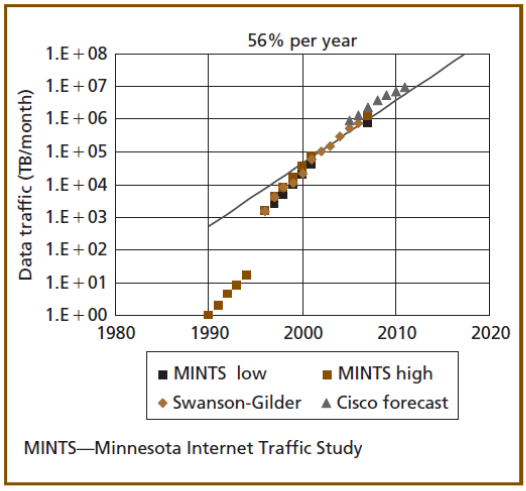

Figure 1.
North American Internet traffic by year.

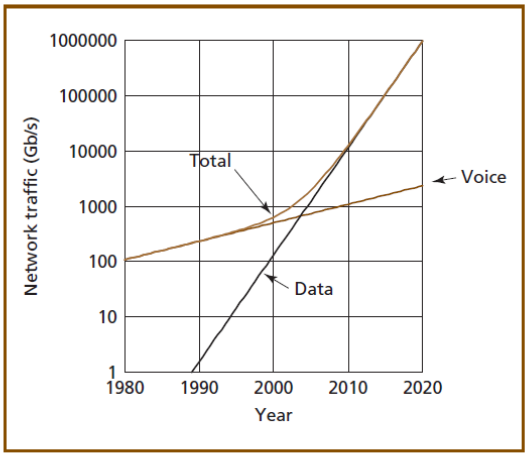

Figure 2.
Total North American network traffic including voice.

Figure 1.3: Internet traffic in North America **[14]**

Furthermore, the dominant part of the increasing total network traffic has shifted from voice to data, as depicted in Figure 1.3. This predicted data traffic growth is attributed not only to real-time entertainment, but also to the emerging applications such as those in healthcare (e.g. DNA sequencing, online healthcare) or car industry (e.g. smart car). But this extensive use of modern technology also bring some concerns, the major being related to the optical network capacity, power consumption and information security.

In view of the optical communication networks, the aforementioned trends place severe challenges to the existing technology, since these networks serve as a backbone of the Internet. Specifically, optical communication networks cannot support the increasing bandwidth demand, due to optical telecommunication system capacity limits

[15]. There are several proposals to approach this problem [15],[16], each with its own performance trade-offs, but the clear path is still not evident.

Even if one could circumvent the problem with optical transmission technology, information and telecommunication infrastructure power consumption is increasing consistently, thus eventually becoming unsustainable. In 2011 [17], information and telecommunication infrastructure consumed about 5% of the of the total power, while today this number has risen to 10% [18]. Unfortunately, this demanding problem raises even more concerns; more disturbing for any environmentalist is association of large power consumption with climate change, bringing more attention to the current information and communication systems, responsible for 2-4% of total carbon emission [19]. Why do these networks consume so much power?

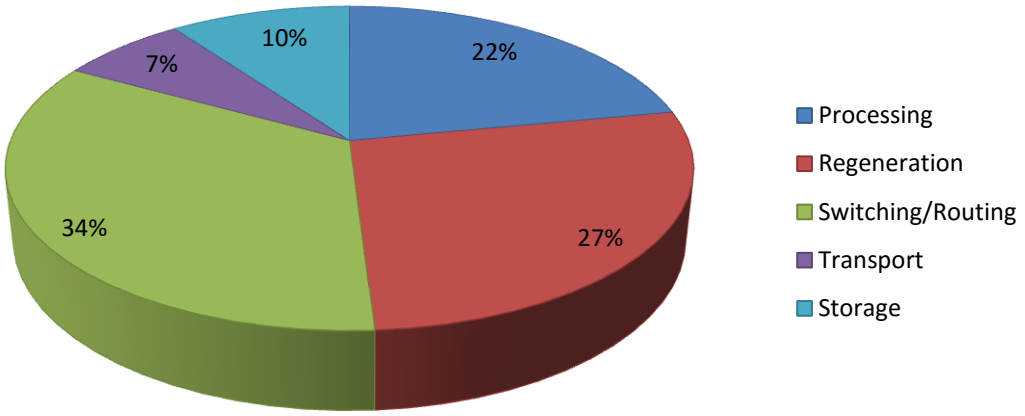

Figure 1.4: Information and telecommunication infrastructure power consumption sorted by network functionality **[20]**

Figure 1.4 represents fractional power consumption within the information and telecommunication system, categorized by network functionality. According to this study, large portion of the power is attributed to the switching/routing, the regeneration and the processing, because these network elements demand high degree of signal quality preservation to meet rigorous signal error detection criteria. Among the three, switches and routers are the major power dissipation elements. This is hardly surprising, since a slow electronic switch requires an optical-electrical-optical (OEO) converter and a demultiplexer to perform switching operation [21], thus adding to the overall energy consumption. As a solution to this problem, an all-optical switch has long been proposed as a low-energy- and high-speed-alternative to an electronic switch [22]. Its low-energy potential was referenced to elimination of an OEO converter and, if operating at high speeds, a demultiplexer. After gaining some maturity, nearly four decades after its inception, this technology is still facing some obstacles in its actual implementation. It is now clear that optical switching is promising, but also apparent that a lot of work remains before its practical implementation.

Lastly, among the major concerns over the past few years has certainly been cyber security. The widespread use of Internet technology often requires transmission and storage of sensitive information (e.g. credit card numbers, social security numbers) over optical networks, therefore leading to increasing number of security violations. The growing number of security breaches is damaging not only to corporations, but can also have severe consequences for an average user. On the financial side, according to the recent study, 7% of corporations reported a loss of one million dollar or more in 2013 in the United States [23]. On the information security side, nearly 20% of

customers across different industries, including banking, finance, government, healthcare, telecom and insurance, were subjects to sensitive personal information compromise or theft [24]. In addressing the existing problems, quantum communication systems are envisioned as means of alleviating information privacy concerns, and promise of revolutionizing optical networks [25]. One of the main obstacles in delivering quantum information today is limited functionality of existing single-photon detector technology [26].

This dissertation aims at addressing some of the above mentioned concerns, specifically those related to optical switching and means of detecting a few-photon signal at high bit rates.

1.4. Overview of existing technology

In this section, an overview of the existing optical switching and the single-photon detection technology is provided. Main device quality parameters are identified and performance cross-section summarized.

1.4.1. Optical switching

Due to their weak interaction, photons are nearly ideal candidates for information transmission. All signal processing tasks, on the other hand, are currently performed by electrons, due to their charged nature. However, these bandwidth-limited electronic devices, require heavy data scaling to match the increasing bandwidth

requirement, ultimately leading to unsustainable energy dissipation. Developing an efficient all-optical signal processing device is, therefore, of great technological and practical importance.

The idea of practical, direct light manipulation originates in 1980s when Smith [22] articulated the notion of all-optical switching devices with potential to overcome total energy consumption and speed limitations inherent to electronic switching devices. An all-optical switch is a device that regulates the transmission of light, itself controlled by an optical signal. Its design relies on photon-photon interaction, mediated by the nonlinear medium (through which photons propagate) via refractive index modulation. The role of energy consumption and switching time was long recognized as critical [22]. Strong dependence of these parameters on the choice of the platform has been verified repeatedly. Of equal importance are other switch parameters: propagation and coupling loss, operating temperature, operating wavelength, switching extinction ratio and bit error ratio. Unfortunately, the well-documented trade-off between some parameters prohibits simultaneous realization of all metrics.

All-optical switching has been demonstrated in a number of different platforms since, but, arguably, none offered performance compelling enough to displace conventional electronic devices. One of the main reasons for the lack of performance is reliance of majority of all-optical switching devices on refractive index modulation, dictating high power dissipation per switching event. Additionally, the integrity of the switched signal, a critical consideration in communication links, is often ignored. However, with progress across multiple physical platforms, optical switching is now realized at significantly lower energy. In a number of recent publications high-speed

switching devices triggered by low photon count have been developed, motivating another look at the utility of optical switching devices. A cross-section of recently reported work is summarized in [27].

Table 1.1: Optical switching devices: review of recent reports. Acronyms: Ref-Refernce; E-Energy; ER-Extinction ratio.

Ref.	**Operating temperature [K]**	**E_{pump}/pulse [J]**	**$E_{control}$/pulse [J]**	**Switching time [ps]**	**ER [dB]**	**Operating wavelength [nm]**	**Loss [dB]**
[28]	300	22e-12	0.2e-12	0.3	<1[1]	1281.4	-
[29]	5-7	1.3e-17	1.3e-17	50	0.3[1]	937	20
[30]	300	3.5e-5	1.9e-19	0.2	7[1]	800	-
[31]	38	1.4e-15[2] (4.3e-17)[3]	1.4e-15[2] (4.3e-17)[3]	17	1[1]	913	15
[32]	300	8.3e-15[2] (0.66e-15)[3]	-	35 off 100 on	10	1567.5	28
[33]	300	1.5e-12[2] (300e-15)[3]	-	14	3.6	1570	14
[34]	300	4.3e-12	1.9e-17	4.8	3	1546	0.74

[1]Estimated from the figure
[2]Power estimated before the coupling loss
[3]Reported power coupled into the waveguide

In contrast to the work reported only a decade ago, the advance is reflected in energy levels: the probe energy per bit has reached a single photon level and the total device energy that of fJ. As expected from the diversity of physical platforms and operating principles, the underlying response time and dissipation vary widely. While

the devices employing a photonic-crystal nanocavity [32],[33] consume low energy per pulse, these have relatively long switching time and high coupling and propagation loss. Conversely, technologies reported in [28],[29],[30],[34] are comparatively fast, but require high pump energies for optimal performance. In [29],[31] a probe energy/pulse has reached a few-photon level, but have long switching time, high loss and require cryogenic environment, adding to the overall energy dissipation. Summarizing the above, one can recognize considerable progress in optical switching, however energy-switching time tradeoff is still present across all platforms. More importantly, the switched signal quality inspection is often absent in recent publications, directly preventing serious consideration of these devices for practical implementation.

1.4.2. Few photon detection

Although rapidly increasing interest in quantum information applications has been a major drive for the development of single-photon detectors, many other applications would derive even higher benefit from the highly sensitive photon sensor. Indeed, a single- and a few-photon receiver can readily be deployed in a variety of applications, spanning medical applications (e.g. DNA sequencing, tissue spectroscopy), astronomy, industrial process control (e.g. remote toxic analysis, environmental monitoring, tablet hardness analysis) and light detection and ranging. However, precise requirements for the single photon detector performance are commonly referenced to quantum information applications [35].

Presently, practical single photon detector types rely on photon-to-electron conversion and subsequent generation of a signal by a different, internal mechanism. This description includes photomultipliers, single photon avalanche photodiodes, superconducting single photon detectors and hybrid detector types [35]. Alternatively, other approaches exploit mixing of a single photon with a strong optical field, followed by detection by a conventional process. Such devices rely on homodyne detection [36], [37], frequency resolved optical gating with spectral interferometry [38] or nonlinear interaction [39], [40]. Not surprisingly, each photon detection device and method has a specific performance trade-off and is typically designed for targeted application.

Traditional single photon detector technology performance can be mutually compared using common detector parameters [26]:

a) Detection efficiency is a probability of an incident photon being registered by the detector and its electronics. The strict definition of this parameter is represented as a product of several efficiencies, $\eta = \eta_{couple}\eta_{absorb}\eta_{QE}\eta_{threshold}$, where η_{couple} is the fraction of incident light reaching the active detector area; η_{absorb} is the fraction of light reaching the active area getting absorbed by the medium; η_{QE} is the fraction of absorbed light producing the macroscopic signal; and $\eta_{threshold}$ is the fraction of the macroscopic signal being registered.

b) Dark count rate is an average number of counts per second generated by the detector with no signal present.

c) Dead time is the time interval between the two consecutive photon counts registration. This parameter represents the major obstacle to single photon detector speed increase.

d) Timing jitter is the uncertainty in the timing latency; timing latency is a parameter representing a period between the photon absorption and registration of a count.

To compare detector performance, we use the Figure of Merit definition after [26]:

$$FOM = \frac{\eta}{D\Delta t} \tag{1}$$

where η is detection efficiency, D is dark count rate and Δt is timing jitter.

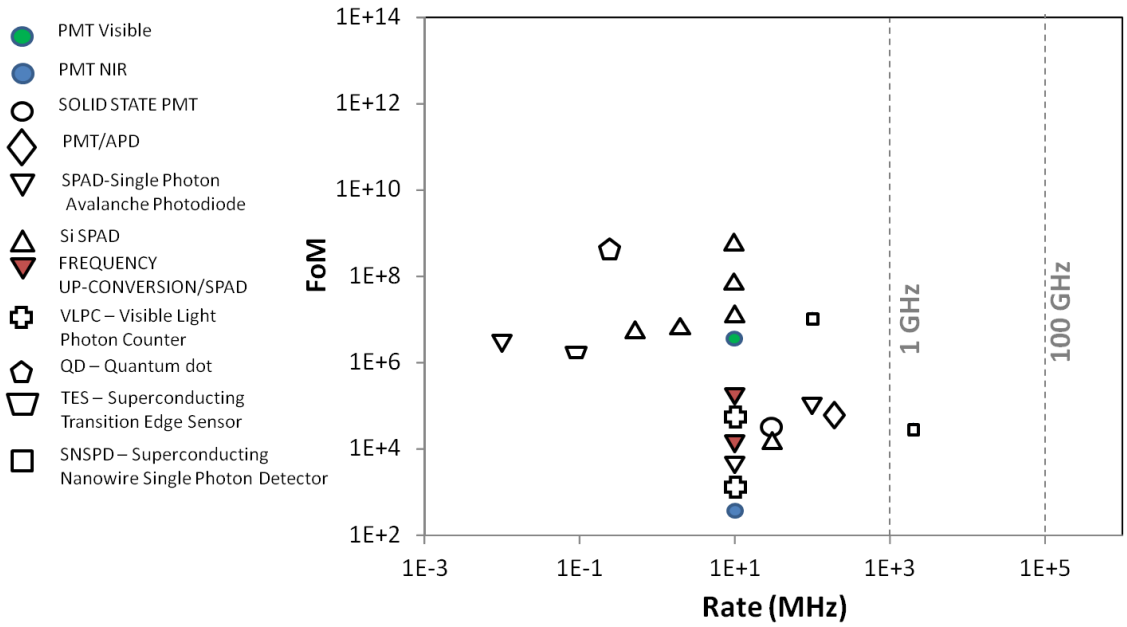

Figure 1.5: Single-photon detector Figure of Merit as a function of maximum count rate **[26]**

Figure 1.5 represents the cross-section of the single photon detector technology. Most devices to date operate at speeds significantly lower than those required in telecommunication systems. Majority of devices are limited to speed on the order of 10 MHz, however with current speed increase attempts some devices have potential to operate at ~1 GHz rate. In these publications, the performance at higher rates was not characterized, and is expected to deteriorate, due to the dark count rate rise with speed. While further efforts are needed to design a fast NIR single photon detector, its operation at 10 GHz rate or higher is far from realization.

1.5. Dissertation organization

This dissertation begins with trends and challenges in modern telecommunication systems, placed by the widespread use of Internet technology. Recognizing main problems, we find solutions by identifying an appropriate set of photonic devices relying on photon interaction. Chapter 2 is devoted to introduction of underlying mechanisms mediating photon interaction in dielectric media, and, more specifically, silica fiber. Both the photon interaction physics and fundamental interaction speed limit are discussed. In Chapter 3, the concept of linear, single-pump, frequency-nondegenerate parametric mixer is introduced and the optimum fiber dispersion maximizing the energy exchange identified. Chapter 4 is dedicated to the study of the nonlinear (saturated) parametric mixer, its design and dispersion engineering. In the following chapter, the experimental demonstration of the static measurement is presented and high-speed, low-energy photon-photon control potential

of the system is highlighted. The main topic of Chapter 6 is the all-optical switching in the saturated parametric mixer, its design and performance. In Chapter 7, parametrically aided few photon detection was investigated in real time. The final chapter is concerned with the future directions of the described technology.

2. Photon-photon interaction

As boson members, with no charge, photons in vacuum do not interact; they can, however, interact indirectly. Depending on the photon energy, there are two types of interaction [41]:

a) In the high photon energy limit, when $\hbar\omega \sim m_e c^2$, the probability of two photon annihilation and electron-positron pair creation is maximal (where m_e is electron mass and c speed of light).

b) In the low photon energy limit, when $\hbar\omega << m_e c^2$, this probability decreases. For near-infrared (NIR) light, it becomes negligible. But NIR photon interaction is still viable, because it can be mediated by the nonlinear medium [42].

The main focus of this dissertation is the photon interaction in dielectric media in the near-infrared wavelength region. The theoretical framework presented in the following chapters is a cross-section of the theories developed in [43], [44], [45], [46], [47], [48] and [49].

2.1. Photon interaction in dielectric media

In describing photon interaction in dielectric media, one can envision it as a two-step process. First, when intense beam propagates through dielectric media, it modifies its properties. An intuitive, but rather crude, model of representing this

modification is based on the Lorentz model [43], [44], [45], [46]. According to this model, a dielectric medium is represented as a collection of coupled harmonic oscillators. An atom, as a dielectric medium constituent, can be depicted as a light electron bound to a heavy nucleus by a spring-like force. In the absence of any external fields, this system is in the equilibrium position. However, when the electric field is applied, the electron is displaced from its equilibrium position, moving in the direction opposite of that of the applied field. This can be depicted as spring compression and extension. As a result of this displacement, an electrostatic force arises to counteract it. A convenient atom illustration, based on the Lorentz model, represents an atom as an oscillating dipole (a harmonic oscillator), when displacement is much smaller than the wavelength of light. The electronic cloud, therefore, oscillates in the direction perpendicular to that of the intense wave propagation, and collinearly with the electric field. An oscillating dipole emits radiation, similar to that of an antenna, in the direction perpendicular to the oscillation. Therefore, in the second step, the medium responds by emitting radiation.

In view of the mathematical representation, the electron motion is governed by the following equation [45]:

$$m[\frac{d^2x(\omega,t)}{dt^2}+2\Gamma\frac{dx(t)}{dt}+\Omega^2x(t)-(\xi^{(2)}x(t)^2+\xi^{(3)}x(t)^3+...)]=-eE(t) \quad (2)$$

Damping term — Restoring force — External field

where x is the electron displacement from the mean position, m is the electron mass, Γ is the damping term and Ω is the resonance frequency.

Linear response

By neglecting anharmonic terms $(\xi^{(2)}x^2 + \xi^{(3)}x^3 + ...)$ in the Eq. (2), linear medium response to external radiation is easily obtained [46], [43]:

$$m[\frac{d^2x(t)}{dt^2} + 2\Gamma\frac{dx(t)}{dt} + \Omega^2 x(t)] = -eE(t) \tag{3}$$

Fourier transform of the Eq. (3) can be expressed as:

$$m\left[(-i\omega)^2 x(\omega) + 2\Gamma(-i\omega)x(\omega) + \Omega^2 x(\omega)\right] = -eE(\omega) \tag{4}$$

The electron displacement is then simply found from Eq. (4):

$$x(\omega) = -\frac{eE(\omega)}{m}\frac{1}{\Omega^2 - 2i\Gamma\omega - \omega^2} \tag{5}$$

The oscillating dipole produces a time varying dipole moment $p(t)$:

$$p(t) = -ex(t) \tag{6}$$

in turn generating the material polarization:

$$P(\omega) = -Nex(\omega) = \frac{Ne^2E(\omega)}{m}\frac{1}{\Omega^2 - 2i\Gamma\omega - \omega^2} \tag{7}$$

The electric displacement *D* of an isotropic, linear medium is related to the polarization and the electric field in the following manner:

$$D = \varepsilon E = \varepsilon_0 E + P \tag{8}$$

Additionally, the polarization in the linear optics depends linearly on the electric field $E(t')$:

$$P(t) = \int_{-\infty}^{\infty} \varepsilon_0 \chi^{(1)}(t-t')E(t')dt' \tag{9}$$

where $\chi^{(1)}(t)$ is the electric susceptibility. This is simply the convolution of the electric field with the medium impulse response $\chi^{(1)}(t)$. Fourier transform of the last equation is of the form:

$$P(\omega) = \varepsilon_0 \chi^{(1)}(\omega)E(\omega) \tag{10}$$

where $\chi^{(1)}(\omega) = \int_{-\infty}^{\infty} \chi^{(1)}(t)e^{-i\omega t}dt$. From these equations, one can easily derive the expression for the linear electric susceptibility:

$$P(\omega) = \frac{Ne^2}{m}\frac{1}{\Omega^2 - 2i\Gamma\omega - \omega^2}E(\omega) = \varepsilon_0\chi^{(1)}(\omega)E(\omega) \tag{11}$$

$$\begin{aligned}\chi^{(1)}(\omega) &= \frac{Ne^2}{m\varepsilon_0}\frac{1}{\Omega^2 - 2i\Gamma\omega - \omega^2} = \\ &= \frac{Ne^2}{m\varepsilon_0}\frac{\Omega^2 - \omega^2}{(\Omega^2 - \omega^2)^2 + (2\Gamma\omega)^2} + i\frac{Ne^2}{m\varepsilon_0}\frac{2\Gamma\omega}{(\Omega^2 - \omega^2)^2 + (2\Gamma\omega)^2}\end{aligned} \tag{12}$$

The linear electric susceptibility is related to the medium index of refraction, *n*, and the absorption coefficient, α, in the following manner:

$$\varepsilon(\omega) = 1 + \mathrm{Re}\left(\chi^{(1)}(\omega)\right) + i\,\mathrm{Im}\left(\chi^{(1)}(\omega)\right) = \left(n + \frac{i\alpha c}{2\omega}\right)^2 \approx n^2 + i\frac{\alpha c n}{\omega} \tag{13}$$

$$n(\omega) = \sqrt{1 + \mathrm{Re}[\chi^{(1)}(\omega)]} \approx 1 + \frac{1}{2}\mathrm{Re}[\chi^{(1)}(\omega)] = 1 + \frac{Ne^2}{2m\varepsilon_0}\frac{\Omega^2 - \omega^2}{(\Omega^2 - \omega^2)^2 + (2\Gamma\omega)^2} \tag{14}$$

$$\alpha(\omega) = \frac{\omega}{nc}Im[\chi^{(1)}(\omega)] = \frac{1}{nc}\frac{Ne^2}{m\varepsilon_0}\frac{2\Gamma\omega^2}{(\Omega^2 - \omega^2)^2 + (2\Gamma\omega)^2} \tag{15}$$

We can now investigate the derived formulae in different frequency limits [43]:

a) In the low frequency limit: $\omega \to 0$

$$\begin{aligned} n(\omega \to 0) &= 1 + \frac{Ne^2}{2m\varepsilon_0}\frac{1}{\Omega^2} \\ \alpha(\omega \to 0) &= 0 \end{aligned} \tag{16}$$

b) In the high frequency limit: $\omega \to \infty$

$$\begin{aligned} n(\omega \to \infty) &= 1 \\ \alpha(\omega \to \infty) &= 0 \end{aligned} \tag{17}$$

c) At frequencies close to the resonance frequency: $\omega \to \Omega$

$$\begin{aligned} n(\Delta\omega) &= 1 - \frac{Ne^2}{2m\varepsilon_0\Omega^2}\frac{2\Omega\Delta\omega}{4(\Delta\omega)^2 + (2\Gamma)^2} \\ \alpha(\Delta\omega) &= \frac{Ne^2}{n(\Delta\omega)cm\varepsilon_0}\frac{4\Gamma}{4(\Delta\omega)^2 + 4\Gamma^2} \end{aligned} \tag{18}$$

This model gives a behavior prediction of an atom with the single resonance frequency. In reality, an atom can have many resonant frequencies corresponding to different atomic transitions, and each transition having an associated probability. To account for this probability in this classical model, an oscillator strength f_j is assigned to each transition:

$$\chi^{(1)}(\omega) = 1 + \frac{Ne^2}{m\varepsilon_0}\sum_j \frac{f_j}{\Omega_j{}^2 - 2i\Gamma_j\omega - \omega^2} \tag{19}$$

This simple model gives quite reasonable prediction of the silica glass refractive index and the absorption spectrum., represented in Figure 2.1.

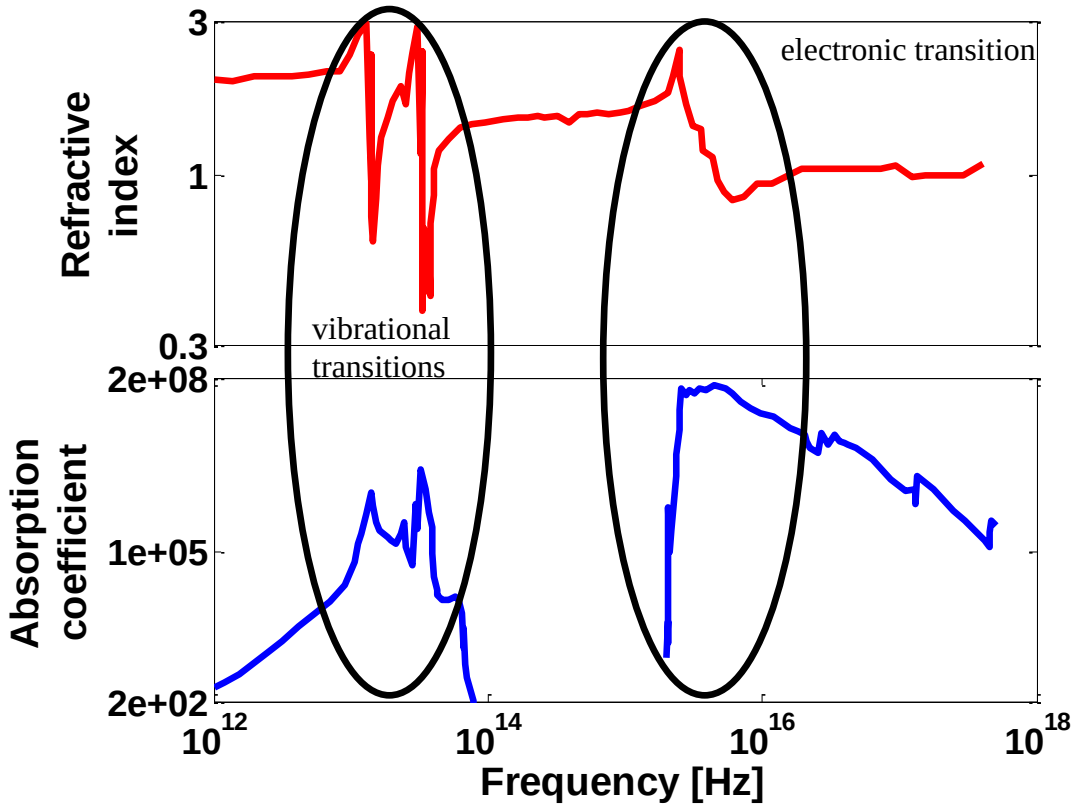

Figure 2.1: Silica refractive index and absorption coefficient as a function of frequency **[47]**

Taking a closer look at the experimental measurement, one can make the following observations [43] :

a) As a glass, silica is an amorphous material. The absorption in the infrared spectrum is, therefore, contributed to excitation of vibrational quanta. There are two peaks in this region: the first one at 1.4×10^{13} Hz (21μm) and the second one at 3.3×10^{13} Hz (9.1μm). In the far-infrared region, refractive index is 2.

b) The absorption in the ultraviolet spectral region is contributed to interband electronic transitions. The main absorption peak is observed at $3x10^{15}$ Hz (100 nm), followed by two secondary peaks at $3x10^{16}$ Hz (10 nm) and $1.3x10^{17}$ Hz (2.3 nm), all initiated by the transition of the inner core electrons of the silicon and the oxygen atom. The absorption threshold is observed at $2x10^{15}$ Hz (150 nm), further allowing for the band gap calculation, $E_g = hf_{resonant} \approx 8.3eV$. In the ultraviolet spectral region, the refractive index approaches unity.

c) In the transparency region, where the loss is minimal, the index of refraction has small variation around the value of 1.5. It is actually increasing from 1.4 at $8x10^{13}$ Hz (3.5 μm) to 1.55 at $1.5x10^{15}$ Hz (200 nm); this increase is ascribed to the low frequency wings of the UV spectral region and the high frequency wings of the NIR spectral region. This frequency region is the main focus of this dissertation.

The derived equations describe the medium response to the applied external field. As a consequence of its interaction with light, the medium modulates the properties of the propagating wave. The refractive index is a parameter affecting the velocity of the propagating wave. The higher the refractive index, the lower the wave group velocity. Refractive index frequency dependence causes the frequency dependent group velocity of the light travelling along the silica medium as follows :

$$v_g(\omega) = \frac{c}{n(\omega)}\left(1 - \frac{k}{n(\omega)}\frac{dn(\omega)}{dk}\right) \tag{20}$$

From this relation, one can obtain higher order dispersion parameters guiding the pulse propagation [48], [49]:

$$\beta_1(\omega) = \frac{1}{v_g(\omega)} = \frac{1}{c}\left(n(\omega) + \omega \frac{dn(\omega)}{d\omega} \right) \tag{21}$$

$$\beta_2(\omega) = \frac{d\beta_1(\omega)}{d\omega} = \frac{1}{c}\left(2\frac{dn(\omega)}{d\omega} + \omega \frac{d^2n(\omega)}{d\omega^2} \right) \tag{22}$$

$$\beta_3(\omega) = \frac{d\beta_2(\omega)}{d\omega} = \frac{1}{c}\left(3\frac{d^2n(\omega)}{d\omega^2} + \omega \frac{d^3n(\omega)}{d\omega^3} \right) \tag{23}$$

$$\beta_4(\omega) = \frac{d\beta_3(\omega)}{d\omega} = \frac{1}{c}\left(4\frac{d^3n(\omega)}{d\omega^3} + \omega \frac{d^4n(\omega)}{d\omega^4} \right) \tag{24}$$

These equations can be expressed in terms of the fiber dispersion, *D*, the dispersion slope, *S*, and the dispersion slope dispersion, $\frac{dS}{d\lambda}$, representing the most commonly characterized fiber parameters [49]:

$$\beta_2(\lambda) = -\frac{\lambda^2}{2\pi c} D(\lambda) \tag{25}$$

$$\beta_3(\lambda) = \frac{\lambda}{(2\pi c)^2}\left(\lambda S(\lambda) + 2D(\lambda) \right) \tag{26}$$

$$\beta_4(\lambda) = -\frac{\lambda}{(2\pi c)^3}\left(\lambda^2 \frac{dS}{d\lambda} + 6\lambda S(\lambda) + 6D(\lambda) \right) \tag{27}$$

Besides the refractive index, the absorption coefficient represents an additional parameter affecting the wave propagation. It manifests thought exponential wave intensity decrease with distance. Fortunately, the absorption coefficient in silica fiber at

λ = 1550 nm is low, reaching 0.1 dB/km. This is the main reason for the wide fiber deployment in modern communications systems.

As a consequence of the external electric field presence, the electron shifts from its equilibrium position, creating a dipole. This harmonic electric field, in fact, produces an oscillating dipole, a system radiating electromagnetic energy. The radiated electromagnetic wave can be retrieved from the retarded potential:

$$E_{rad} = -\theta \frac{p_0}{4\pi\varepsilon_0 r} \frac{\omega^2}{c^2} \sin\theta \cos\left(\omega\left(t - \frac{r}{c}\right)\right) \tag{28}$$

where $p_0 = -ex_0$ is the dipole moment amplitude, θ the radiation direction and r is the observation distance with respect to the dipole. An interesting feature of the last equations is its directional dependence. The dipole oriented along the z axis, radiates the electromagnetic field in the perpendicular direction with the described angular dependence. The radiated power can be derived using the Poynting vector as:

$$P = \frac{p_0^2}{12\pi\varepsilon_0} \frac{\omega^4}{c^3} \tag{29}$$

Note its frequency dependence is of the order of ω^4, the form recognized in an effect known as the Rayleigh scattering. These equations simply imply that an atom affected by an external field radiates the electromagnetic field in all directions, with frequency-dependent power.

Nonlinear response

The linear medium response is observed regardless of the external electric field intensity. Conversely, nonlinear effects are present only at high light intensities. To understand the origin of nonlinear effects, we go back to the atom representation. In the linear model, we have assumed small electron displacement from its equilibrium position, *x,* making the harmonic model valid. However, with high electrical field intensity, the linear model no longer holds, due to a large electron displacement. To estimate the intensity value leading to a linear model failure, we revisit the atom model. Namely, an electron in an atom is bound to a nucleus by an electric filed with intensity $E_{at} = e/(4\pi\varepsilon_0 a_0^2) \approx 5.14\times10^{11} V/m$, where $a_0 = 4\pi\varepsilon_0\hbar^2/(me^2)$ is the Bohr radius of the hydrogen atom [46]. When the external light field intensity approaches the value $I_{at} = 0.5\varepsilon_0 c E_{at}^2 \approx 3.5\times10^{20} W/m^2$, nonlinear effects are observable. However, nonlinear effects can appear at significantly lower intensities, due to coherent addition of emitted light from different parts of the medium, an effect appearing only when emitted light is in phase, often referred to as the phase matching condition (this will be discussed in detail, later in the chapter).

The nonlinear medium response depends to a large extent to material properties. Specifically, crystal symmetry properties play the critical role in determining the response [46] Out of 32 crystal classes, only 11 possess inversion symmetry and silica is an important member of this group. To represent nonlinear response mathematically, we go back to the harmonic oscillator model:

$$m[\frac{d^2\tilde{x}(t)}{dt^2}+2\Gamma\frac{dx(t)}{dt}+\Omega^2\tilde{x}(t)-(\xi^{(2)}\tilde{x}(t)^2+\xi^{(3)}\tilde{x}(t)^3+...)]=-e\tilde{E}(t) \quad (30)$$

where the fourth term on the left hand side is relevant for the non-centrosymmetric crystal, and the fifth term for the centrosymmetric crystal response. A feature of the centrosymmetric crystal response is that the second order response (corresponding to the fourth term) vanishes, having the following final form:

$$m[\frac{d^2\tilde{r}(t)}{dt^2}+2\Gamma\frac{d\tilde{r}(t)}{dt}+\Omega^2\tilde{r}(t)-\xi^{(3)}(\tilde{r}(t)\cdot\tilde{r}(t))\tilde{r}(t)]=-eE(t) \quad (31)$$

where r is the electron displacement in the $\boldsymbol{r}$ direction. To model the perturbation strength imposed by the external field, the perturbation parameter, λ (having values between 0 and 1), is added to the electric field, thus modifying the $E(t)$ to $\lambda E(t)$. Electron response to the applied field of the high intensity is no longer linear and it evolves in the following manner:

$$\tilde{r}(t)=\lambda\tilde{r}^{(1)}(t)+\lambda^2\tilde{r}^{(2)}(t)+\lambda^3\tilde{r}^{(3)}(t)+... \quad (32)$$

The electron evolution equation now becomes:

$$m[\frac{d^2\tilde{r}(t)}{dt^2}+2\Gamma\frac{d\tilde{r}(t)}{dt}+\Omega^2\tilde{r}(t)-\xi^{(3)}(\tilde{r}(t)\cdot\tilde{r}(t))\tilde{r}(t)]=-\lambda eE(t) \quad (33)$$

Separating parameters of the same λ order, the following equation set is retrieved:

$$m[\frac{d^2\tilde{r}^{(1)}(t)}{dt^2}+2\Gamma\frac{d\tilde{r}^{(1)}(t)}{dt}+\Omega^2\tilde{r}^{(1)}(t)]=-e\tilde{E}(t) \quad (34)$$

$$\frac{d^2\tilde{r}^{(2)}(t)}{dt^2}+2\Gamma\frac{d\tilde{r}^{(2)}(t)}{dt}+\Omega^2\tilde{r}^{(2)}(t)=0 \quad (35)$$

$$\frac{d^2\tilde{r}^{(3)}(t)}{dt^2}+2\Gamma\frac{d\tilde{r}^{(3)}(t)}{dt}+\Omega^2\tilde{r}^{(3)}(t)-\xi^{(3)}(\tilde{r}^{(1)}(t)\cdot\tilde{r}^{(1)}(t))\tilde{r}^{(1)}(t)=0 \tag{36}$$

From Eq. (34), we can obtain $\chi^{(1)}$ of the same form as in the linear case. The steady state solution of the Eq. (35) vanishes. To find $\chi^{(3)}$, we first need to substitute solution for $r^{(1)}$ into Eq. (36):

$$\frac{d^2\tilde{r}^{(3)}(t)}{dt^2}+2\Gamma\frac{d\tilde{r}^{(3)}(t)}{dt}+\Omega^2\tilde{r}^{(3)}(t)=-\sum_{mnp}\frac{\xi^{(3)}e^3[E(\omega_m)\cdot E(\omega_n)]E(\omega_p)}{m^3D(\omega_m)D(\omega_n)D(\omega_p)}e^{-i(\omega_m+\omega_n+\omega_p)t} \tag{37}$$

where $D(\omega)=\Omega^2-\omega^2-2i\omega\Gamma$. Fourier transform of this Equation is of the form:

$$\begin{aligned}&(-i\omega)^2r^{(3)}(\omega)+2\Gamma(-i\omega)r^{(3)}(\omega)+\Omega^2r^{(3)}(\omega)=\\&=-\sum_{mnp}\frac{\xi^{(3)}e^3[E(\omega_m)\cdot E(\omega_n)]E(\omega_p)}{m^3D(\omega_m)D(\omega_n)D(\omega_p)}\delta(\omega-(\omega_m+\omega_n+\omega_p))\end{aligned} \tag{38}$$

By simple substitution, one can get the following expression for the electron displacement:

$$r_q^{(3)}(\omega_q)=-\sum_{mnp}\frac{\xi^{(3)}e^3[E(\omega_m)\cdot E(\omega_n)]E(\omega_p)}{m^3D(\omega_m)D(\omega_n)D(\omega_p)D(\omega_q)} \tag{39}$$

where $\omega_q=\omega_m+\omega_n+\omega_p$. The polarization also acquires a modified form:

$$\begin{aligned}\tilde{P}(\omega)=\varepsilon_0\chi(\omega)\tilde{E}(\omega)=\varepsilon_0\left(\chi^{(1)}(\omega)+\chi^{(2)}(\omega)\tilde{E}(\omega)+\chi^{(3)}(\omega)(\tilde{E}(\omega))^2+...\right)\tilde{E}(\omega)=\\\equiv\tilde{P}^{(1)}(\omega)+\tilde{P}^{(2)}(\omega)+\tilde{P}^{(3)}(\omega)+...\end{aligned} \tag{40}$$

In the case of centrosymmetric crystals, like silica, the second order effects disappear, modifying the nonlinear polarization expression:

$$\tilde{P}(\omega)\approx\varepsilon_0\left(\chi^{(1)}(\omega)\tilde{E}(\omega)+\chi^{(3)}(\omega)(\tilde{E}(\omega))^3\right)=\tilde{P}^{(1)}(\omega)+\tilde{P}^{(3)}(\omega) \tag{41}$$

The first- and the third-order polarization can be expressed in the form:

$$P^{(1)}(\omega) = -Ner^{(1)}(\omega) \tag{42}$$

$$P_i^{(1)}(\omega) = \varepsilon_0 \sum_j \chi_{ij}^{(1)}(\omega) E_j(\omega) \tag{43}$$

$$\chi_{ij}^{(1)}(\omega) = \chi^{(1)}(\omega)\delta_{ij} \tag{44}$$

$$P^{(3)}(\omega_q) = -Ner^{(3)}(\omega_q) \tag{45}$$

$$P_i^{(3)}(\omega_q) = \varepsilon_0 \sum_{jkl} \sum_{mnp} \chi_{ijkl}^{(3)}(\omega_q, \omega_m, \omega_n, \omega_p) E_j(\omega_m) E_k(\omega_n) E_l(\omega_p) \tag{46}$$

By simple substitution one can then find the expression for the third order susceptibility:

$$\begin{aligned} \chi_{ijkl}^{(3)}(\omega_q, \omega_m, \omega_n, \omega_p) &= \frac{N\xi^{(3)} e^4 (\delta_{jk}\delta_{il} + \delta_{ik}\delta_{jl} + \delta_{il}\delta_{jk})}{3\varepsilon_0 m^3 D(\omega_q) D(\omega_m) D(\omega_n) D(\omega_p)} = \\ &= \frac{\xi^{(3)} m \varepsilon_0^3}{3N^3 e^4} \left(\chi^{(1)}(\omega_q) \chi^{(1)}(\omega_m) \chi^{(1)}(\omega_n) \chi^{(1)}(\omega_p) \right) \left(\delta_{jk}\delta_{il} + \delta_{ik}\delta_{jl} + \delta_{il}\delta_{jk} \right) \end{aligned} \tag{47}$$

Due to permutation symmetry and mutual dependence of different susceptibility tensor elements, the nonlinear susceptibility elements can be expressed in the compact form:

$$\chi_{ijkl}^{(3)} = \chi_{1122}^{(3)} \delta_{ij}\delta_{kl} + \chi_{1212}^{(3)} \delta_{ik}\delta_{jl} + \chi_{1221}^{(3)} \delta_{il}\delta_{jk} \tag{48}$$

$$\chi_{1122}^{(3)} = \chi_{1212}^{(3)} = \chi_{1221}^{(3)} \tag{49}$$

$$\chi_{ijkl}^{(3)} = \chi_{1122}^{(3)} (\delta_{ij}\delta_{kl} + \delta_{ik}\delta_{jl} + \delta_{il}\delta_{jk}) \tag{50}$$

$$\chi_{1111}^{(3)} = 3\chi_{1122}^{(3)} \tag{51}$$

This further simplifies the nonlinear polarization expression, by removing the summation:

$$P_i^{(3)}(\omega_q) = \varepsilon_0 D \sum_{jkl} \chi_{ijkl}^{(3)}(\omega_q, \omega_m, \omega_n, \omega_p) E_j(\omega_m) E_k(\omega_n) E_l(\omega_p) \tag{52}$$

where D is the number of distinct permutations of the frequencies ω_m, ω_n and ω_p.

The constant $\xi^{(3)}$ can be estimated by assuming comparability of the linear and the nonlinear part of the restoring force when electron displacement approaches the atomic dimension d:

$$m\Omega^2 d = m\xi^{(3)} d^3 \tag{53}$$

$$\xi^{(3)} = \frac{\Omega^2}{d^2} \tag{54}$$

To determine the intensity dependent refractive index and the absorption coefficient, one can start from the following relation:

$$\hat{\varepsilon}(\omega) = 1 + \mathrm{Re}(\chi) + i\,\mathrm{Im}(\chi) = \left(\hat{n} + \frac{i\hat{\alpha}c}{2\omega}\right)^2 \approx \hat{n}^2 + i\frac{\hat{\alpha}c}{\omega n} \tag{55}$$

and further attain the intensity dependent refractive index as follows

$$\hat{n}^2 = 1 + \mathrm{Re}(\chi) \tag{56}$$

The right hand side of the Eq. (55) can be rewritten in the following form:

$$\hat{n}^2 = \left(n_0 + n_2 < I(t) >\right)^2 = \left(n_0 + n_2 c\varepsilon_0 n_0 |E|^2\right)^2 = {n_0}^2 + 2n_2 c\varepsilon_0 {n_0}^2 |E|^2 \tag{57}$$

The left hand side of the Eq. (55) can also be re-expressed:

$$1 + \mathrm{Re}(\chi) = 1 + \mathrm{Re}\left(\chi^{(1)}\right) + \frac{3}{4}\mathrm{Re}\left({\chi_{xxxx}}^{(3)}\right)|E|^2 \tag{58}$$

The Eq. (55) then takes the following form:

$$n_0^{\,2} + 2n_2 c\varepsilon_0 n_0^{\,2} \mid E \mid^2 = 1 + \mathrm{Re}\left(\chi^{(1)}\right) + \frac{3}{4}\mathrm{Re}\left(\chi_{xxxx}^{\,(3)}\right) \mid E \mid^2 \tag{59}$$

From the last expression one can recognize the linear index of refraction, $n_{0,}$ defined previously in Eq. (14) as $n_0^{\,2} = 1 + \mathrm{Re}\left(\chi^{(1)}\right)$. The nonlinear refractive index, n_2, can then be derived in the form:

$$n_2 = \frac{3}{8c\varepsilon_0 n_0^{\,2}}\mathrm{Re}\left(\chi_{xxxx}^{\,(3)}\right) \tag{60}$$

Similarly, the intensity dependent absorption can be obtained in the following manner

$$\alpha_0 + \alpha_2 < I >= \frac{\omega}{n_0 c} Im\left(\chi^{NL}(\omega)\right) \tag{61}$$

The right hand side can be rewritten in the form:

$$\alpha_0 + \alpha_2 < I >= \alpha_0 + \alpha_2 \mid E \mid^2 \tag{62}$$

while the left hand side can be expressed as:

$$\frac{\omega}{n_0 c} Im\left(\chi(\omega)\right) = \frac{\omega}{n_0 c} Im\left(\chi^{(1)}(\omega)\right) + \frac{3}{4}\frac{\omega}{n_0 c} Im\left(\chi_{xxxx}^{(3)}(\omega)\right) \mid E \mid^2 \tag{63}$$

The final form of Eq. (61) is:

$$\alpha_0 + 2\alpha_2 \mid E \mid^2 = \frac{\omega}{n_0 c} Im\left(\chi^{(1)}(\omega)\right) + \frac{3}{4}\frac{\omega}{n_0 c} Im\left(\chi_{xxxx}^{(3)}(\omega)\right) \mid E \mid^2 \tag{64}$$

From the last expression one can recognize the absorption coefficient, α_0, defined previously as $\alpha_0 = \frac{\omega}{n_0 c} Im\left(\chi^{(1)}(\omega)\right)$. The two-photon absorption coefficient, $\alpha_{2,}$ is given by relation:

$$\alpha_2 = \frac{3\omega}{4n_0 c} Im\left(\chi^{(3)}_{xxxx}(\omega)\right) \tag{65}$$

Influence of intensity dependent variations on the external field driving it is described in the next section.

2.2. Photon interaction in the silica fiber in the near-infrared frequency range

Maxwell's equations [48] represent an equation set describing electric and magnetic field generation and modification:

$$\nabla \times E = -\frac{\partial B}{\partial t} \tag{66}$$

$$\nabla \times H = J + \frac{\partial D}{\partial t} \tag{67}$$

$$\nabla \cdot D = \rho_f \tag{68}$$

$$\nabla \cdot B = 0 \tag{69}$$

where E and H is the electric and the magnetic field respectively, D and B is the corresponding electric and the magnetic flux density, J is the current density and ρ_f is the charge density. In the absence of free charges in the optical fiber, we can set $J = 0$ and $\rho_f = 0$. When the medium is interacting with external electric or magnetic fields, the flux densities D and B occur and are mutually related through the following relations:

$$D = \varepsilon_0 E + P \tag{70}$$

$$B = \mu_0 H + M \tag{71}$$

where μ_0 is the vacuum permeability and *M* is the induced magnetic polarization. The latter can be set to 0 for fiber, due to its inherently weak magnetic properties.

There are two different energy flow interpretation methods: the photon interpretation and the wave interpretation.

Photon interpretation

Electromagnetic energy conservation is given by the Poynting theorem (with the current density *J* = 0)[50]:

$$\frac{\partial u}{\partial t} \equiv -\nabla S = -\nabla (E \times H) = \left(\frac{1}{2}\right) \frac{\partial \left(\varepsilon_0 E^2 + \mu_0 H^2\right)}{\partial t} + E \frac{\partial P}{\partial t} + \sigma : EE \tag{72}$$

where *u* is the electromagnetic energy density, *S* is the Poynting vector and σ is the conductivity. The three terms on the right hand side of the last equation represent contributions from different effects:

1. The first term characterizes the temporal change of electromagnetic field energy density in the vacuum;
2. The second term describes the energy density change due to the medium polarization.
3. The third term represents contribution from the conductivity.

From this equation it is easily envisioned how the medium polarization alters the electromagnetic field(s) inducing it. For the purpose of this work we are interested

in the second term. Namely, the time averaged rate of the energy density change can be represented in the following form assuming the presence of many monochromatic waves:

$$p_l \equiv < E\frac{\partial P}{\partial t} >_t = \sum_r p_{lr} = \sum_r \frac{i\omega_r}{4}\sum_i \left[E_i^*(f_r)P_i(f_r) - E_i(f_r)P_i^*(f_r) \right] \tag{73}$$

We investigate interaction among four monochromatic waves where $\omega_q = \omega_m + \omega_n - \omega_p$. The induced material polarization at each frequency component is of the form:

$$\begin{aligned}
P_i(f_q = f_m + f_n - f_p) &= \varepsilon_0 \sum \chi_{ijkl}(-f_q, f_m, f_n, -f_p)E_j(f_m)E_k(f_n)E_l(-f_p) \\
P_i(f_m = f_q - f_n - f_p) &= \varepsilon_0 \sum \chi_{ijkl}(-f_m, f_q, -f_n, -f_p)E_j(f_q)E_k(f_n)E_l(-f_p) \\
P_i(f_n = f_q - f_m - f_p) &= \varepsilon_0 \sum \chi_{ijkl}(-f_n, f_q, -f_m, -f_p)E_j(f_q)E_k(f_m)E_l(-f_p) \\
P_i(f_p = -f_q + f_m + f_n) &= \varepsilon_0 \sum \chi_{ijkl}(-f_p, -f_q, f_m, f_n)E_j(-f_q)E_k(f_m)E_l(f_n)
\end{aligned} \tag{74}$$

One can then express the energy density per unit frequency (the photon number per unit time per unit volume) as follows:

$$\begin{aligned}
\Delta N_q &= \frac{p_{lq}}{\hbar\omega_q} = \frac{i\varepsilon_0}{4\hbar}\sum [\chi_{ijkl}(-f_q, f_m, f_n, -f_p)E_i(-f_q)E_j(f_m)E_k(f_n)E_l(-f_p) - c.c.] \\
\Delta N_m &= \frac{p_{lm}}{\hbar\omega_m} = \frac{i\varepsilon_0}{4\hbar}\sum [\chi_{ijkl}(-f_m, f_q, -f_n, f_p)E_i(-f_m)E_j(f_q)E_k(-f_n)E_l(f_p) - c.c.] \\
\Delta N_n &= \frac{p_{\ln}}{\hbar\omega_n} = \frac{i\varepsilon_0}{4\hbar}\sum [\chi_{ijkl}(-f_n, f_q, -f_m, f_p)E_i(-f_n)E_j(f_q)E_k(-f_m)E_l(f_p) - c.c.] \\
\Delta N_p &= \frac{p_{1p}}{\hbar\omega_p} = \frac{i\varepsilon_0}{4\hbar}\sum [\chi_{ijkl}(-f_p, -f_q, f_m, f_n)E_i(-f_p)E_j(-f_q)E_k(f_m)E_l(f_n) - c.c.]
\end{aligned} \tag{75}$$

One can easily show that for the lossless process, where $p_l = 0$, the Manley-Rowe equations are obtained:

$$\Delta N_q = \Delta N_p = -\Delta N_m = -\Delta N_n$$
$$\frac{p_{lq}}{\hbar\omega_q} = \frac{p_{lp}}{\hbar\omega_p} = -\frac{p_{lm}}{\hbar\omega_m} = -\frac{p_{\ln}}{\hbar\omega_n} \tag{76}$$

This equation set implies that two photons at frequencies ω_m and ω_n are generated simultaneously, as a consequence of annihilation of two photons at frequencies ω_p and ω_q. This process thus conserves energy. In other words, the medium does not absorb energy, it has only passive role in mediating photon interaction.

Wave interpretation

.

The wave equation, describing wave propagation, can be derived from the Maxwell equations by taking the curl of the Eq. (66) and combining it with the Eq. (67):

$$\nabla\times\nabla\times E = -\frac{1}{c^2}\frac{\partial^2 E}{\partial t^2} - \mu_0\frac{\partial^2 P}{\partial t^2} \tag{77}$$

$$P = P_L + P_{NL} \tag{78}$$

Assuming P_{NL} is a small perturbation of the total induced polarization, using the identity $\nabla\times\left(\nabla\times E\right) = \nabla(\nabla\cdot E) - \nabla^2 E$ and taking the Fourier transform of the wave equation, one can derive the Helmholtz equation:

$$\nabla^2 E(\omega) + \varepsilon(\omega)\frac{\omega^2}{c^2}E(\omega) = 0 \tag{79}$$

where $\varepsilon(\omega)$ can be expressed as:

$$\varepsilon(\omega) = 1 + \chi^{(1)}(\omega) + \frac{3}{4}\chi_{xxxx}{}^{(3)} \mid E \mid^2 \tag{80}$$

To solve the Helmholtz equation, one can use the separation of variables, assuming the solution in the following form:

$$E(r, \omega - \omega_0) = F(x, y)A(z, \omega - \omega_0)\exp(i\beta_0 z) \tag{81}$$

The transverse field component is of the following form:

$$\frac{\partial^2 F}{\partial x^2} + \frac{\partial^2 F}{\partial y^2} + [\varepsilon(\omega)k_0^2 - \tilde{\beta}^2]F = 0 \tag{82}$$

while the longitudinal field evolution is guided by the following equation:

$$2i\beta_0 \frac{\partial \tilde{A}}{\partial z} + \left(\tilde{\beta}^2 - \beta_0^2\right)\tilde{A} = 0 \tag{83}$$

where $\tilde{\beta}(\omega)$ is given by

$$\tilde{\beta}(\omega) = \beta(\omega) + \Delta\beta(\omega) \tag{84}$$

In the last equation $\Delta\beta(\omega)$ is defined as:

$$\Delta\beta(\omega) = \frac{\omega^2 n(\omega)}{c^2 \beta(\omega)} \frac{\int\int_{-\infty}^{\infty} \Delta n \mid F(x, y) \mid^2 dxdy}{\int\int_{-\infty}^{\infty} \mid F(x, y) \mid^2 dxdy} \tag{85}$$

$$\Delta n = n_2 \mid E \mid^2 + \frac{i\widehat{\alpha}}{2k_0} \tag{86}$$

and $\beta(\omega)$ can be expressed by the Taylor expansion around the frequency ω_0

$$\begin{aligned} \beta(\omega) = \beta(\omega_0) + (\omega - \omega_0)\beta_1(\omega_0) + \frac{1}{2}(\omega - \omega_0)^2 \beta_2(\omega_0) + \\ + \frac{1}{6}(\omega - \omega_0)^3 \beta_3(\omega_0) + \frac{1}{24}(\omega - \omega_0)^4 \beta_4(\omega_0) + \ldots \end{aligned} \tag{87}$$

$$\beta_0 \equiv \beta(\omega_0) \tag{88}$$

From these equations one can derive the nonlinear Schrodinger (NLS) equation in the form:

$$\frac{\partial A}{\partial z} + \beta_1 \frac{\partial A}{\partial t} + \frac{i\beta_2}{2}\frac{\partial^2 A}{\partial t^2} + \frac{\alpha}{2}A = i\gamma(\omega_0)\,|A|^2\,A \tag{89}$$

where γ is the nonlinear parameter defined as:

$$\gamma(\omega_0) = \frac{n_2(\omega_0)\omega_0}{cA_{eff}} \tag{90}$$

and A_{eff} is the effective mode area defined as:

$$A_{eff} = \frac{\left(\int\int_{-\infty}^{\infty} |F(x,y)|^2\,dxdy\right)^2}{\int\int_{-\infty}^{\infty} |F(x,y)|^4\,dxdy} \tag{91}$$

From the nonlinear Schrodinger equation, a set of coupled wave equations is easily obtained, assuming the optical field consists of multiple monochromatic frequency components of constant amplitude ($\frac{\partial A}{\partial t} = 0$):

$$\frac{dA_l}{dz} = i\gamma\left[|A_l|^2 A_l + 2\sum_{j\neq l=1}^{4} |A_j|^2 A_l + 2A_m A_n A_k^* e^{i\varepsilon\Delta kz}\right] \qquad l = 1-4 \tag{92}$$

where Δk is the linear phase mismatch guiding the energy exchange:

$$\Delta k = \beta(\omega_m) + \beta(\omega_n) - \beta(\omega_k) - \beta(\omega_l) \tag{93}$$

The three terms on the right hand side of the Eq. (86) describe nonlinear phenomena present in optical fiber. The first term is the self phase modulation (SPM) phenomenon, an effect causing self-intensity-driven phase modulation. This effect becomes particularly important in the short pulse propagation, where the intensity modulation

transfers to phase modulation. This time-dependent phase variation leads to frequency chirping, thus effectively resulting in spectral broadening. The second term is the cross phase modulation (XPM) phenomenon where one wave modulates the phase of the second wave. Its effect is similar to the SPM, differing in the effect strength (due to the presence of factor of 2 in the Eq. (86)). Finally, the last term represents the four wave mixing, an effect in charge of both the amplitude and the phase modulation of interacting waves. Its nature allows for a new frequency components generation and amplification.

2.3. The fundamental speed limit of photon interaction in the silica fiber

Photon interaction is mediated by the nonlinear medium, having a finite response time [46]. This response time originates from the bound electron recovery time, a time interval needed for an electron cloud to become distorted as a response to the external electric field. This determines the maximum speed available for photon manipulation, strongly depending on the medium properties.

Recent measurement of silica response time suggests its inverse relation to the damping rate as follows [51]:

$$\tau = \Gamma^{-1} = \left(3.5 \cdot 10^{14} \frac{E_g}{n^2} \right)^{-1} = 0.8\, fs \tag{94}$$

where the band-gap energy, E_g, is expressed in electron volts. Ultrafast nature of this interaction contributed to its wide acceptance as instantaneous. In fact, a single optical

cycle at 1550 nm is about 5 fs long, and in this regard the medium response time can be considered quasi-instantaneous.

Although desirable, this ultimate speed limit is nearly impossible to reach, since it is typically masked by dispersion effects leading to pulse reshaping. Therefore, the speed of devices relying on nonlinear effects in a silica fiber is likely to be dominated by the silica fiber dispersion properties. Furthermore, devices exploiting the bandwidth-constrained amplification are additionally limited to speed ranges proportional to the inverse of the amplifier bandwidth.

3. Linear parametric mixer: design and dispersion engineering

In this dissertation, the linear parametric mixer concept is associated with a notion of a device capable of both amplifying a signal and generating new frequency components via the four wave mixing process in a nonlinear element such as a highly nonlinear fiber [49]. In this process, from a quantum mechanical point of view, two pump photons, one from each pump at frequencies ω_1 and ω_2 are annihilated to create the signal photon at frequency ω_3 and the idler at ω_4, satisfying the energy and the momentum conservation law. Practical ease of achieving an efficient energy exchange among interacting photons led to variety of mixer designs, capable of performing under different operating regimes. In its simplest implementation, often referred to as a one-pump fiber optical parametric amplifier (FOPA), the energy is transferred from the pump to the signal and the idler wave. It can be realized in the frequency degenerate form, where $\omega_1=\omega_2=\omega_3=\omega_4$, or the frequency non-degenerate form, where $\omega_1=\omega_2\neq\omega_3\neq\omega_4$. In the case of the two-pump FOPA, the energy is transferred from two frequency non-degenerate pumps to the signal and the idler, $\omega_1\neq\omega_2\neq\omega_3\neq\omega_4$. In this section, we focus on the single pump, frequency non-degenerate mixer.

Using the classical notation, the interaction of three waves at frequencies ω_1, ω_3 and ω_4, can be described by the set of coupled wave equations [52]:

$$\frac{dA_1}{dz} = -2\gamma A_3 A_4 A_1 \sin\phi \tag{95}$$

$$\frac{dA_3}{dz} = \gamma A_4 A_1^2 \sin\phi \tag{96}$$

$$\frac{dA_4}{dz} = \gamma A_3 A_1^2 \sin\phi \tag{97}$$

$$\frac{d\phi}{dz} = \Delta k_L + \gamma\left[2A_1^2 - \left(A_3^2 + A_4^2\right)\right] + \gamma\left[A_1^2\left(\frac{A_3}{A_4} + \frac{A_4}{A_3}\right) - 4A_3A_4\right]\cos\phi \tag{98}$$

$$\phi = \Delta k_L z + \phi_3 + \phi_4 - 2\phi_1 \tag{99}$$

$$\Delta k_L = \beta^{(2)}\Delta\omega^2 + \frac{\beta^{(4)}}{12}\Delta\omega^4 \tag{100}$$

where A_j, $j=1,3,4$ is the amplitude of the pump, the signal and the idler respectively, ϕ_j the phase of the pump, the signal and the idler respectively, γ the nonlinear parameter, Δk_L the linear phase mismatch, $\Delta\omega$ the frequency separation between the pump and the signal and $\beta^{(2)}$ and $\beta^{(4)}$ the second and the fourth order dispersion coefficient respectively. Direction of the power flow depends on the phase relation among interacting waves, ϕ. The maximal power transfer from the pump to the signal and the idler is achieved when $\phi = \pi/2$, recognized as the phase matched condition. The exact phase matched condition form depends on the operating regime. In the linear operating regime, pump depletion is neglected and the pump power remains nearly constant during pump-signal-idler propagation. Furthermore, the normalized phase mismatch parameter can be introduced in the following form [47]:

$$\kappa \equiv \frac{\Delta k_L}{\gamma P_0} \tag{101}$$

where $P_0 = A_1^2(0) + A_3^2(0) + A_4^2(0)$ is the total power circulating in the system. The maximal FOPA gain is reached when the linear phase mismatch (Eq. 100) compensates the nonlinear phase mismatch contribution, $\Delta k_{NL} = \gamma\left[2A_1^2 - \left(A_3^2 + A_4^2\right)\right]$ (or κ = -2).

This condition shows strong gain bandwidth and frequency positioning dependence on the fiber dispersion properties, therefore allowing for a degree of freedom in the mixer design.

To investigate the linear parametric mixer gain reciprocity, the coupled mode equations are solved by using the following parameter set: nonlinear parameter γ= 12.5 $W^{-1}km^{-1}$, dispersion slope S = 0.025 ps/(nm^2km), pump power P_1= 1.44 W, pump wavelength λ_1=1554 nm, pump phase ϕ_1=-π/4, signal power P_3= 0.31 μW, signal wavelength λ_3=1565 nm, signal phase ϕ_3=0, idler power P_4= 0.79 nW, idler phase ϕ_4=0 and fiber length L = 200 m. The equations in the linear regime are solved for three cases, differing in the longitudinal zero dispersion wavelength (ZDW) profile: In the first case, the longitudinal zero-dispersion wavelength is constant, having a value of 1538.506 nm. In the second case, we find a longitudinal profile by sectioning the fiber into 2000 segments and following the nonlinear-phase mismatch evolution. Lastly, the obtained profile is directionally reversed, and the equation set, yet again, solved. As expected form the well-known theory [53], the signal gain, under described conditions, is reciprocal. In fact, no significant difference between the three cases is observed, as depicted in Figure 3.1. The normalized phase mismatch remains centered around -2, and $\phi(z)$ at $\pi/2$, thus demonstrating that the phase matched condition is met.

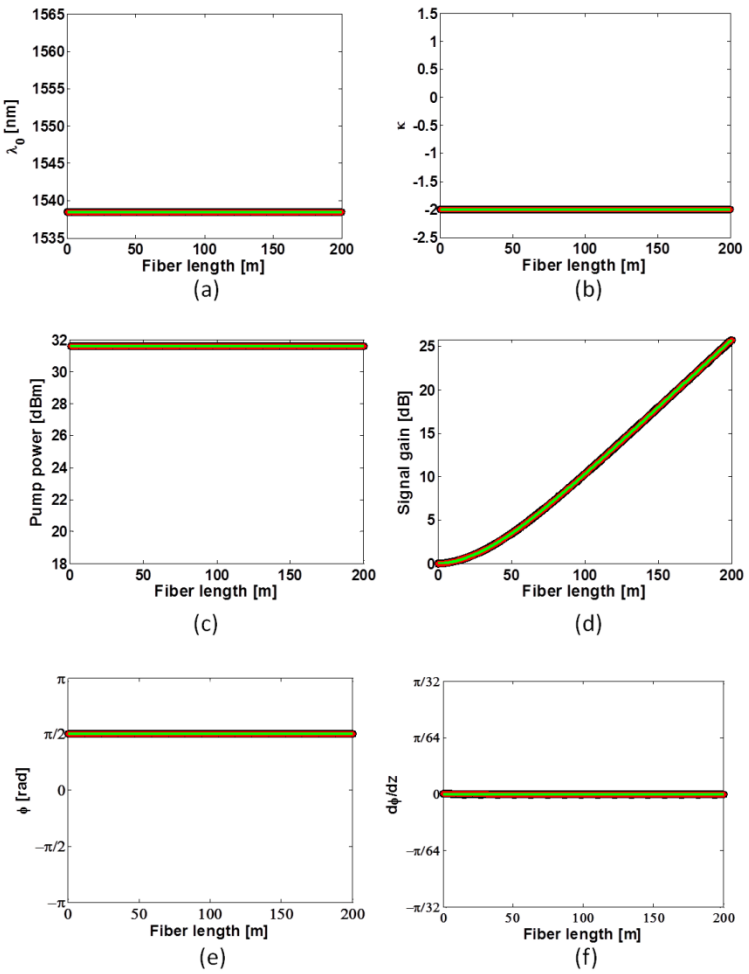

Figure 3.1: Parametric amplifier in the linear propagation regime. a) Longitudinal zero-dispersion wavelength profile. b) Normalized phase mismatch vs. fiber length. c) Pump power vs. fiber length. d) Signal gain vs. fiber length. e) $\phi(z)$ vs. fiber length. f) $d\phi/dz$ given by Eq. (98) vs. fiber length. Green curve - uniform ZDW. Black curve - ZDW profile realized by following the nonlinear phase mismatch evolution. Red curve - directional inverse of the obtained profile.

While using dispersion parameters to design mixer response for specific implementation simplifies its construction, this strategy can also have detrimental effect on the mixer performance. Indeed, in conventional design, only the global dispersion is considered, in spite of the fact that random longitudinal fluctuations in the ZDW of the fiber [54] can qualitatively change the four-photon mixing process. Although during the fabrication process, the fiber core radius is maintained as strictly uniform, it is

practically always characterized by small fluctuations. Highly nonlinear fiber core radius fluctuations of only 0.1% result in approximately 1-nm ZDW fluctuations [55]. The scale of core fluctuation is comparable to the silica ring size (~0.6 nm), prohibiting a direct, fabrication-controlled suppression techniques leading to a strictly uniform waveguide.

In the linear parametric mixer, characterized by the constant pump power, the nonlinear phase mismatch remains nearly constant, thus requiring the constant linear phase mismatch and, by implication, a uniform fiber to achieve the phase matched condition. Until recently, optimum gain performance was limited by longitudinal ZDW fluctuations. However, recent advances in fiber engineering now allow for a fiber fabrication with ZDW fluctuations reduced by an order of magnitude [56].

Chapter 3 in part is a reprint of the material as it appears in the IEEE/OSA Journal of Lightwave Technology, volume 33, issue 24, 1-7 (2015), titled "Directional Phase-Matched Interaction in the Saturated Parametric Mixer" by Ana Pejkic, Ron R. Nissim, Evgeny Myslivets, Andreas O. J. Wiberg, Nikola Alic, and Stojan Radic. Chapter 3, also contains in part material submitted for publication as it may appear in the Progress of Quantum Electronics, titled "High speed parametric processing controlled by few photons," by Ana Pejkic, and Stojan Radic. The dissertation author was the primary investigator, and the primary author of these articles.

4. Nonlinear parametric mixer: design and dispersion engineering

In contrast to the linear parametric mixer, characterized by nearly constant pump power along the interaction length, the nonlinear mixer is a subject to a different operating condition. In the latter case, efficient energy exchange among interacting waves and new frequency generation leads to appreciable pump power depletion. This regime was recognized early by Marhic [49] for a mixer operated in the phase insensitive regime. With no idler wave present at the device input, it can be shown that the maximal pump depletion is related to the following parameters [45]:

$$\Delta k_L - \gamma\left[A_S^2(0) - \frac{A_I^2(0)}{2}\right] = 0 \tag{102}$$

where Δk_L is given by Eq. (100). In contrast to the phase matching condition in the linear operating regime leading to gain maximization, the condition given by Eq. (102) is designed to minimize the pump power level. In practice, there are more than three waves participating in the mixing process, thus limiting the predictive accuracy of the thee-wave model described in the second section.

Surprisingly, no study analyzing the impact of the ZDW fluctuations on the pump depletion existed until recently [57]. The model relying on the NLS equation [48] was deployed to simulate the propagation of the multiple frequency components in the fiber with a varying ZDW. Furthermore, the predictive accuracy the model was further enhanced by incorporating the effect of vacuum fluctuation.

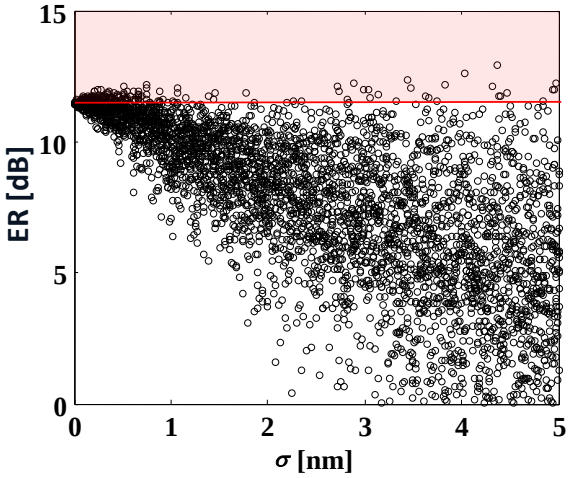

Figure 4.1: Pump extinction ratio as a function of zero-dispersion wavelength standard deviation. Solid red line-uniform zero dispersion wavelength

The extinction ratio (ER) defined as the pump output power ratio in the presence and in the absence of the signal was presented as a function of the ZDW standard deviation [57]. The uniform fiber, having $\sigma = 0$ is indicated by the red line and is used as a performance reference. Each point represents a single ensemble member possessing a unique, randomly generated ZDW profile; all members have the same global fiber parameters. This model predicted not only detrimental effect of the ZDW fluctuations on the ER, but also ER enhancement, as noted in the shaded red area in Figure 4.1. To explain such a counterintuitive behavior, we revisit Eq. (98) corresponding to the simple, three-wave model. Nonlinear phase mismatch $\Delta k_{NL} = \gamma\left[2A_1^2 - \left(A_3^2 + A_4^2\right)\right]$ is a subject to change along propagation due to the non-constant pump power and comparable pump, signal and idler power levels. If fiber is segmented into sections having a constant but mutually varying ZDW, optimal phase matching condition can be achieved only if the linear phase mismatch follows the nonlinear phase

mismatch evolution at each segment - one way to achieve this is to vary the ZDW in a controlled manner.

To gain more insight into directional phase matched interaction we solve the coupled mode equations employing the following parameter set: nonlinear parameter γ= 12.5 $W^{-1}km^{-1}$, dispersion slope S = 25 s/m^3, pump power P_1= 1.44 W, pump wavelength λ_1=1554 nm, pump phase ϕ_3=-$\pi/4$, signal power P_3= 0.31 μW, signal wavelength λ_3=1565 nm, signal phase ϕ_3=0, idler power P_4= 0.79 nW, idler phase ϕ_4=0 and fiber length L = 520 m. Equations are solved for the same three cases described in the linear regime. Figure 4.2 shows simulation results in the saturated regime, shown to significantly differ from those in the linear operation. While gain in the linear regime remains reciprocal, this in no longer true in the saturation. The longitudinal ZDW profile recovered by following the nonlinear phase mismatch evolution is shown to have the performance superior to that obtained with the other two investigated profiles. An interesting feature of the normalized phase mismatch is its evolution from the value of -2, corresponding to the phase matched condition in the linear regime, to 1. The latter value can be acquired by matching the linear and the nonlinear phase mismatch contribution, $\Delta k_L = -\Delta k_{NL}$, from which it follows $\kappa \equiv \frac{\Delta k_L}{\gamma P_0} = -\frac{2A_1^2(z) - A_2^2(z) - A_3^2(z)}{A_1^2(0) + A_2^2(0) + A_3^2(0)}$. In the case when pump energy is completely transferred to the signal and the idler ($A_1^2(z)$ = 0), this parameter converges to 1. Another important distinction from the other two profiles is that $\phi(z) = \pi/2$ throughout

the entire interaction length, ensuring the power flow from the pump to the signal and the idler.

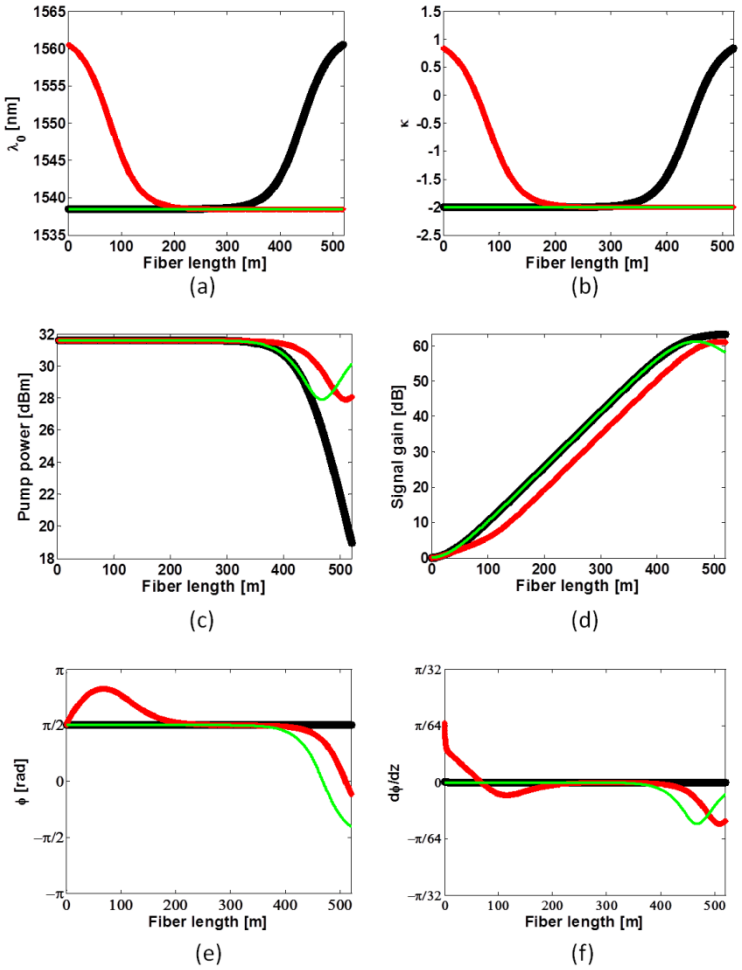

Figure 4.2: Parametric amplifier in the saturation regime. a) Longitudinal zero-dispersion wavelength profile. b) Normalized phase mismatch vs. fiber length. c) Pump power vs. fiber length. d) Signal gain vs. fiber length. e) $\phi(z)$ vs. fiber length. f) $d\phi / dz$ given by Eq.(98) vs. fiber length. Green curve - uniform ZDW. Black curve - ZDW profile attained by following the nonlinear phase mismatch evolution. Red curve - directional inverse of the obtained profile.

Although the case presented here demonstrates the existence of the phase matched interaction when the linear phase mismatch compensates the nonlinear phase mismatch contribution, this condition might be insufficient in general. Taking a closer look at the Eq. (98) one can observe the existence of the third term on the right hand

side, in general, affecting the phase matched interaction. When the signal power approaches the pump power or when the FOM takes the value twice as large as the one described in this section, this term needs to be included.

Summarizing the discussion above, there are two important notions characteristic for the saturated parametric mixer operation:

a) Gain non-reciprocity can be predicted by the simple three wave model;

b) The longitudinally-dispersion-uniform fiber is suboptimal.

While this approach gives an intuitive explanation of the observed trend, an attempt to apply it in the measurement modeling fails, because the model does not take into account higher order mixing products. These newly generated frequency components contribute to further increase in the depletion level and, possibly, variation in the ZDW, difficult to tract. Therefore, only the full model utilizing the NLS leads to optimum profile detection.

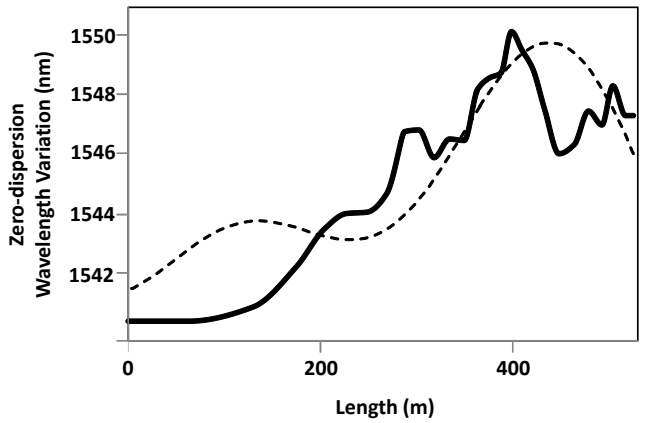

Figure 4.3: Longitudinal zero dispersion wavelength profile of the fiber. Solid line-experiment. Dashed line-simulation

One of the longitudinal profiles resulting in the ER higher than that of the uniform fiber is represented by the dashed line in Figure 4.3. However, as explained in the previous section, fabrication of such a fiber is challenging, because it requires a nanometer-scale control over a fiber radius. Alternative way to produce the obtained profile is to map the ZDW profile of a fiber and find sections with similar trend. The mapping was performed by the Brillouin scanner technique [58] and the attained profile represented by the solid curve on Figure 4.3. This result has opened the door to a new set of experiments that aim at exploring the ultimate efficiency and speed of few-photon controlled wave propagation.

Chapter 4 in part is a reprint of the material as it appears in the IEEE/OSA Journal of Lightwave Technology, volume 33, issue 24, 1-7 (2015), titled "Directional Phase-Matched Interaction in the Saturated Parametric Mixer" by Ana Pejkic, Ron R. Nissim, Evgeny Myslivets, Andreas O. J. Wiberg, Nikola Alic, and Stojan Radic. Chapter 4, also contains in part material submitted for publication as it may appear in the Progress of Quantum Electronics, titled "High speed parametric processing controlled by few photons," by Ana Pejkic, and Stojan Radic. The dissertation author was the primary investigator, and the primary author of these articles. Lastly, Chapter 4 in part is a reprint of the material as it appears in the Science Journal, volume 345, issue 6195,417-419 (2014), titled "Ultrafast optical control by few photons in engineered fiber" by Ron R. Nissim, Ana Pejkic, Evgeny Myslivets, Bill P.-P. Kuo, Nikola Alic, and Stojan Radic. The dissertation author was the primary investigator, and the co-primary author of this article.

5. Photon interaction in the dispersion engineered nonlinear parametric mixer

Pursuit of an ideal photon interaction mediator is motivated by a long envisioned dream of a fast and energy efficient optical signal processing device. In an attempt to design such a device, we have discovered a qualitatively new insight into saturated parametric amplifier response [57]. These new findings relate the optimum longitudinal dispersion profile, with resonant energy exchange among interacting four wave mixing frequency components, widely known as the phase matched condition. The longitudinal dispersion dependence of the phase matching condition is shown to be a major contributor to the non-reciprocal saturated mixer response, contrary to the well established linear parametric mixer theory [53].

In the traditional linear parametric mixer, resonant energy exchange among different frequency components is associated with the phase matching condition of a constant form. In other words, resonant energy exchange appears in an ideal fiber having the uniform longitudinal dispersion. Indeed, many experimental demonstrations confirmed this notion, specifically, those relating the randomly varying longitudinal dispersion with mixer performance deterioration [54] [59]. This phase matching uniformity, in turn, prohibits the non-reciprocal nature of the linear parametric mixer response [53].

How the saturated parametric mixer responds to the longitudinal dispersion variations was largely unexplored until recently. It was Marhic [49] who first

recognized the new condition minimizing the pump power, differing from the phase matching condition. This result directly enabled the first demonstration of nearly complete pump power depletion [60], later followed by new results with reduced signal energy levels [34]. However, it was the new prospects in longitudinal fiber dispersion characterization [58], that allowed us to expand the understanding of the saturated mixer. We now know that this operating regime allows the non-reciprocal response, as a consequence of the power-dependent phase matching condition.

In the following chapters we present experimental verification of the non-reciprocal response at different pump wavelengths and power levels in the continuous wave regime and affirm the feasibility of the photon-photon interaction with a pulsed signal.

5.1. Photon interaction in the continuous wave regime

In this section we present experimental verification of the non-reciprocal response at different pump wavelengths and power levels.

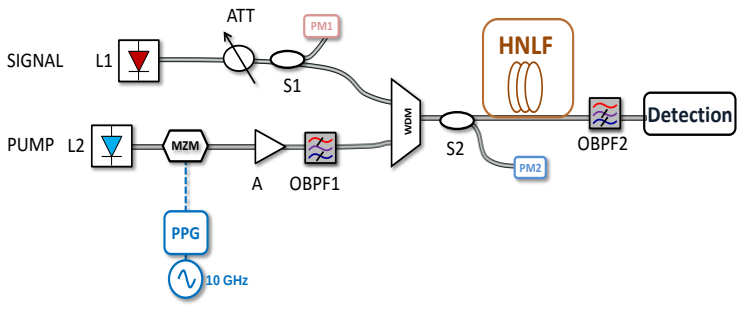

Figure 5.1: Experimental setup for non-reciprocity characterization. Acronyms: L-laser, ATT- attenuator, S-splitter, PM - power meter, MZM- Mach Zehnder modulator, PPG-pattern generator, A-amplifier, OBPF-optical band-pass filter, WDM-wavelength division multiplexer, HNLF-highly nonlinear fiber.

The experimental setup for non-reciprocity characterization at different pump wavelengths and pump powers is shown in Figure 5.1 [61]. The stimulated Brillouin scattering was suppressed by amplitude modulating a tunable external cavity (EC) pump laser; its pulsewidth was 1 ns, with 63.1 ns period. The modulated pump was then amplified to 14 dBm average power. Another tunable EC laser, serving as a signal wave, was attenuated, combined with the amplified pump and sent to a 520 m long highly nonlinear fiber (HNLF) with the nonlinear coefficient of 12.3 $W^{-1}km^{-1}$, the propagation loss of 1.1 dB/km and the longitudinal ZDW profile characterized by the Brillouin counter colliding scanner [58] shown in Figure 4.3 (solid line). The pump was filtered by a 2 nm optical band pass filter (OBPF) at the output of the HNLF and detected by a photodiode (PD). The equivalent time oscilloscope was next employed to characterize the pump depletion level: the sampling point at the center of the pulse was identified and used to eliminate the roll-off at the edges imposed by the finite response time of the modulator and the pattern generator. The pump depletion was measured as the pump output power ratio with the signal present and absent and is further characterized as a function of the signal wavelength and the signal power. The signal wavelength was tuned from 5 to 15 nm away from the pump, in 0.1 nm steps, whereas the signal power was varied from -20 dBm to -40 dBm, with 1 dB step. First, the described characterization was performed in both propagation directions (corresponding to the ZDW profile from Figure 4.3 (solid line) (forward) and its directional inverse (i.e. backwards)) and at three pump wavelengths: 1552nm, 1554 nm and 1556nm.

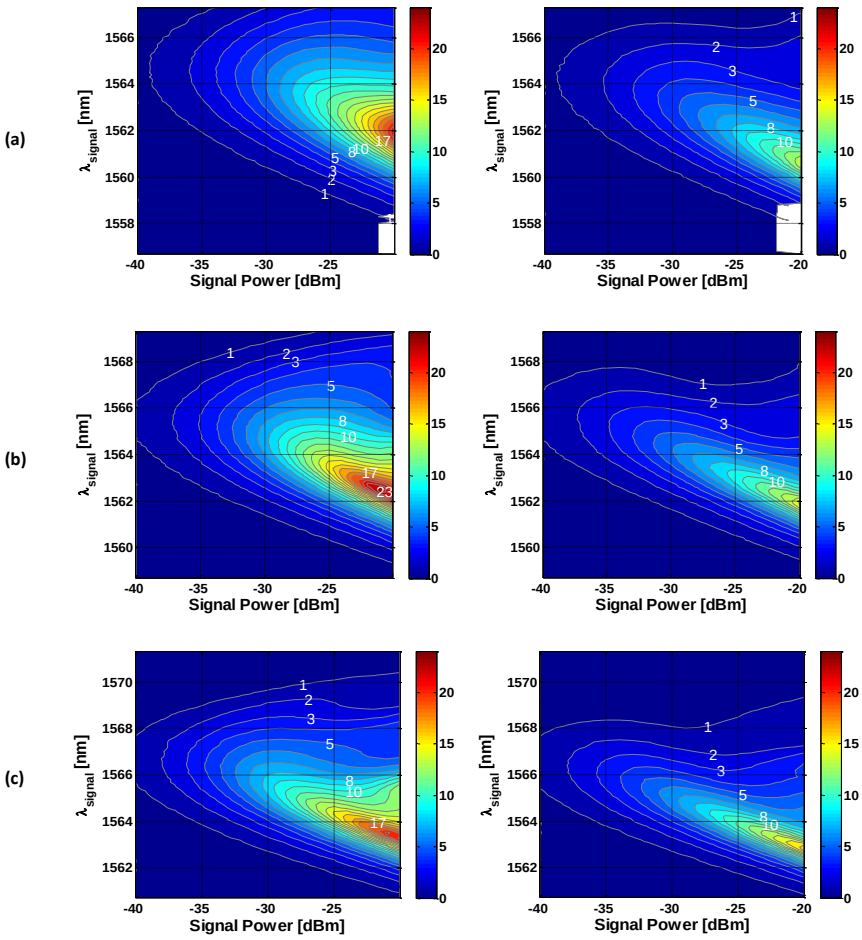

Figure 5.2: Pump power depletion as a function of signal power and signal wavelength characterized for different pump wavelengths and two propagation directions. (a) λp=1552 nm; Left-forward propagation; Right-backward propagation. (b) λp=1554 nm; Left-forward propagation; Right-backward propagation. (c) λp=1556 nm; Left-forward propagation; Right-backward propagation.

As seen in Figure 5.2.(a)-(c), the presence of directional phase-matched interaction is evident at all three pump wavelengths, revealed by the characteristic sharp difference in the corresponding system responses for the two directions. Specifically, both the amount of depletion and the depletion bandwidth decrease in the 'backward' propagation direction at signal power levels higher than -38 dBm. The perceived contrast is diminished at signal power lower than -38 dBm. This non-reciprocity variation is attributed to two effects: First, for moderate amounts of saturation, the

FOPA response approaches that of the linear system, which is reciprocal **[53]**. Second, the phase matching in the saturated system is demonstrably signal power dependent, implying the existence of an optimum ZDW profile at each signal power level, leading to the depletion maximization. As evident from the results in Figure 5.2, the chosen profile maximizes the depletion at higher signal power levels.

We next study the existence of the optimum pump wavelength, maximizing the performance. To aid the performance estimation, 3 dB and 10 dB depletion bandwidths are plotted as a function of the input signal power in Figure 5.3(a) and Figure 5.3(c). This information was then used to estimate the average signal photon number initiating the depletion**.** In particular, the photon number is estimated assuming it being pertinent to a transform limited Gaussian pulse having a peak power corresponding to that of the CW signal and the bandwidth matching the 3 dB or 10 dB depletion bandwidth. While admittedly characterized by a limited accuracy, the conceived estimation method was used for the determination of the optimal pump position. The depletion bandwidth decreases with the pump wavelength in the backward propagation direction for higher signal power, while just the opposite behavior is observed at lower signal power levels, as represented in Figure 5.3(a) and Figure 5.3(c). A similar trend is present in the forward direction.

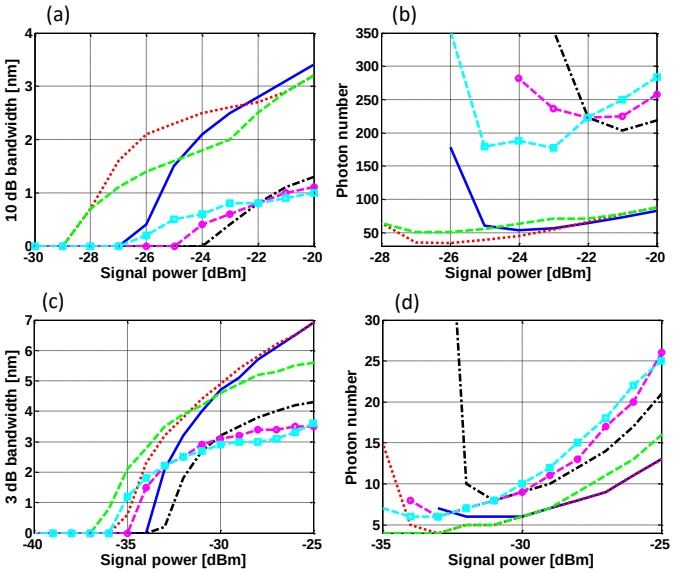

Figure 5.3: Pump depletion bandwidth and average signal photon number as a function of signal power characterized for different pump wavelengths and propagation directions. (a) 10 dB depletion bandwidth as a function of signal power. (b) Photon number for 10 dB depletion as a function of signal power. (c) 3 dB depletion bandwidth as a function of signal power. (d) Photon number for 3 dB depletion as a function of signal.

Next, the existence of the optimal pump wavelength position was determined as follows: the most favorable pump wavelength was identified as that allowing for a 3 dB, (or 10 dB) depletion level with the lowest average signal photon number over the widest available signal power range. The optimal wavelength is inferred from the results shown in Figure 5.3(c) and Figure 5.3(d), corresponding to 1554 nm in both propagation directions. Specifically, the obtained results predict a 3 dB-strong depletion attained with as few as 4 photons (within the assumed transform limited Gaussian pulse profile) on average, while a minimum of 35 photons are needed to achieve the 10 dB level of pump depletion.

Lastly, the non-reciprocity dependence on the pump power was studied by mapping the fiber response at two different pump power levels.

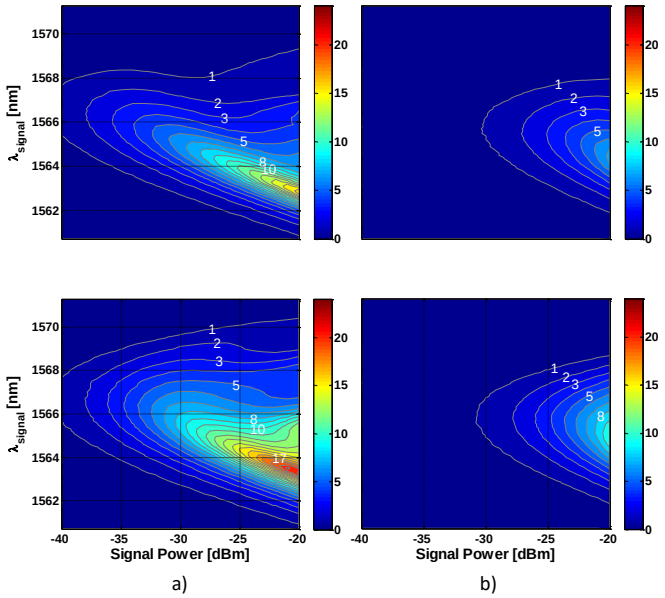

Figure 5.4: Pump power depletion as a function of signal power and signal wavelength characterized for different pump powers and two propagation directions. Pump wavelength is λp=1556 nm. (a) <Pp> = 14 dBm; Up-'backward' propagation; Down-'forward' propagation. (b) <Pp> = 13 dBm; Up-'backward' propagation; Down-'forward' propagation.

Figure 5.4 represents the pump depletion dependence on the pump power and propagation direction at λp=1556 nm. The response closely follows the outlined predictions; depletion level decreases with pump power over the investigated signal power range, with non-reciprocal response being present at both pump power levels.

To estimate the limits of few-photon control, we use the same approach for average signal photon number estimation, as in the first case.

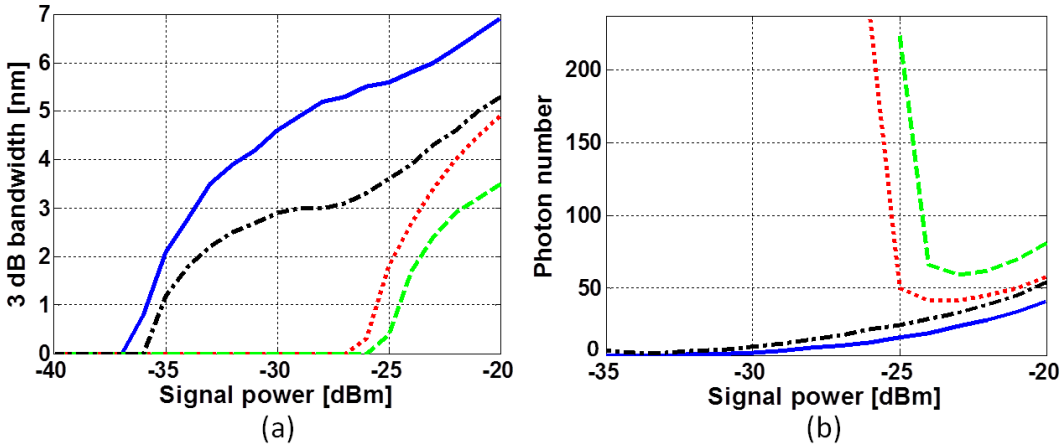

Figure 5.5: Pump depletion bandwidth and average signal photon number as a function of signal power characterized for different pump powers and propagation directions. (a) 3 dB depletion bandwidth as a function of signal power. (b) Photon number for 3 dB depletion as a function of signal power. Green dashed curve <Pp> = 13 dBm (backward). Red dotted curve <Pp> = 13 dBm (forward). Blue solid curve <Pp> = 14 dBm (forward). Black dotted dashed curve $<P_p>$= 14 dBm (backward).

Although the depletion bandwidth decreases with the pump power in both propagation directions, "forward" propagation direction has improved performance with respect to its directionally inverse at both investigated pump power levels, as depicted in Figure 5.5(a). Furthermore, the presence of directional phase matching is observed in Figure 5.5(b), representing 3 dB strong depletion achieved with minimal average signal photon number. This measurement confirms performance superiority of "forward" propagating waves, with respect to the "backward" at both pump power levels.

It is important to note that this static measurement presumes monochromatic phase matching and has only limited role in a dynamic (pulsed) interaction prediction.

5.2. Photon interaction in the pulsed-signal regime

The key topic of the current section is the feasibility of few- and many-photon interaction in the pulsed signal regime. We study the interaction of the pulsed, few-photon signal and the continuous wave (CW) pump in the dispersion engineered fiber by monitoring the pump depletion level initiated by the weak signal.

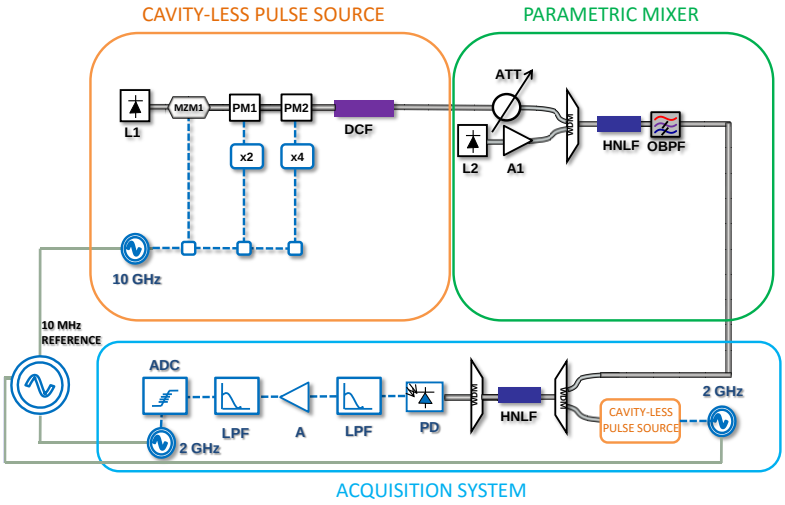

Figure 5.6: Experimental setup for pump depletion characterization driven by short pulses . Acronyms: L-laser, MZM-Mach-Zehnder modulator, PM-phase modulator, DCF - dispersion compensating fiber, ATT-attenuator, A-amplifier, WDM - wavelength division multiplexer, HNLF - highly nonlinear fiber, OBPF - optical band-pass filter, PD - photodiode, LPF - low-pass filter, ADC - analog to digital convertor.

The three main parts compose the system, as shown in Figure 5.6 a source of a weak Poisson signal, an engineered mixer and an acquisition system capable of acquiring fast changes in a depleted pump waveform. The source was engineered as a cavity-less pulse source with 2.5 ps pulse width and 10 GHz repetition rate [62], classically attenuated to achieve the desired photon number. The average photon number is

estimated by measuring the average power. This classically attenuated source was then combined with the amplified, 31.6 dBm-strong CW pump and sent to the parametric mixer. At the output of the mixer, the pump was filtered and detected by the customized acquisition system [63]. In this step, the pump waveform was parametrically sampled by combining the pump with the sampling source (designed using the cavity-less architecture). The sampling pump had 2 GHz repetition rate and a small frequency offset with respect to the weak signal source; both waves were sent to a highly nonlinear fiber acting as a gating element. Newly generated idler, containing the samples of the depleted pump wave was detected and digitized. This sampling system has several advantages over the existing optical sampling instruments: it allows for free control of the sampling rate and, more importantly, frequency-locking of the sampling pulse to the transmitter source. The latter is a critical feature because it reduces the timing jitter, otherwise severely affecting the detection process. Moreover, it also allows for full control over the shape and the bandwidth of the electrical filter, shaping the noise performance during the acquisition of the arbitrary pump waveform.

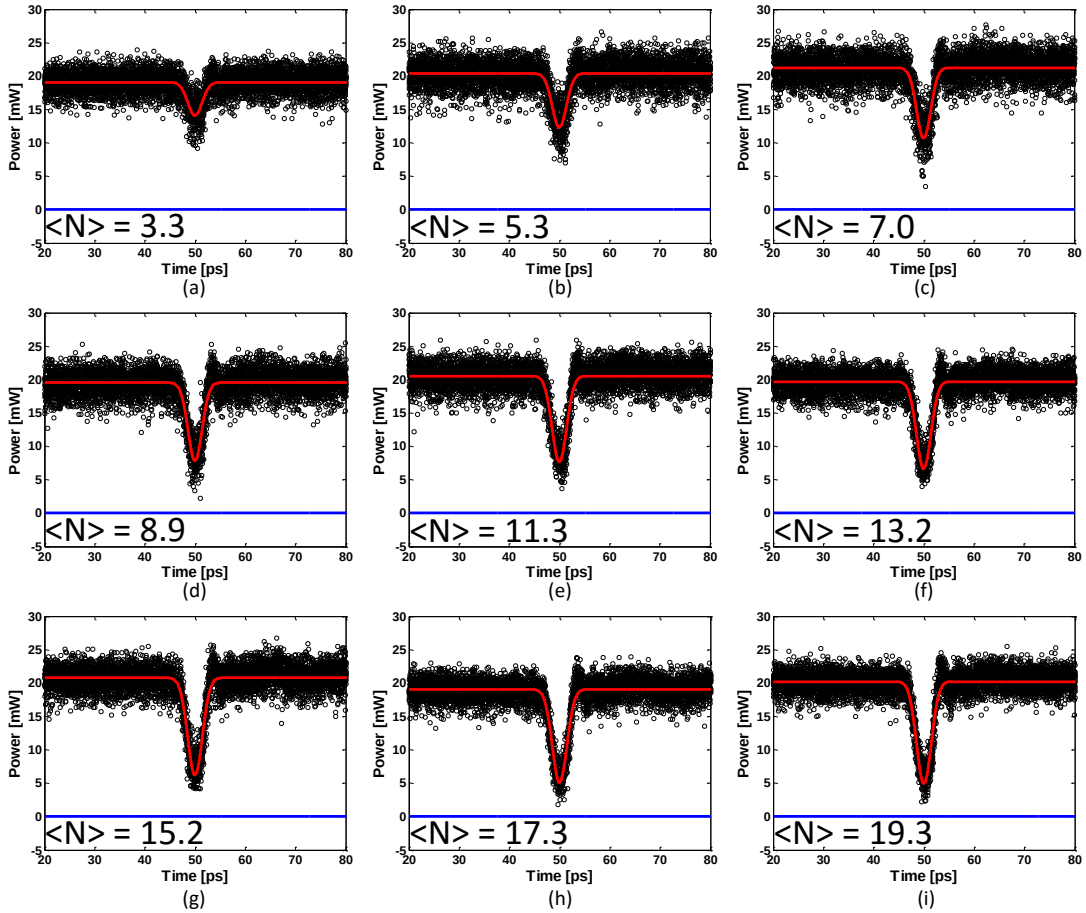

Figure 5.7: Time domain measurement of pump depletion induced by 2.5 ps pulses with an average number of photons <N> of (a) <N> = 3.3. (b) <N> = 5.3. (c) <N> = 7. (d) <N> = 8.9. (e) <N> = 11.3. (f) <N> = 13.2. (g) <N> = 15.2. (h) <N> = 17.3. (i) <N> = 19.3.

The detected pump waveform with a signal footprint corresponding to a different average signal photon number is represented in Figure 5.7. An increase in extinction ratio with signal energy is evident, as predicted by the static measurement. Furthermore, the designed detection system has the ability to detect only three photons on average, and differentiate a stronger signal. This simple observation leads to an important conclusion: an efficient interaction between few- and many-photon beams in

the highly nonlinear fiber is practically feasible, thus opening the door to new possibilities in optical switching and quantum information processing.

Chapter 5 in part is a reprint of the material as it appears in the IEEE/OSA Journal of Lightwave Technology, volume 33, issue 24, 1-7 (2015), titled "Directional Phase-Matched Interaction in the Saturated Parametric Mixer" by Ana Pejkic, Ron R. Nissim, Evgeny Myslivets, Andreas O. J. Wiberg, Nikola Alic, and Stojan Radic. Chapter 5, also contains in part material presented at the Optical Fiber Communication Conference 2015, paper W1K.2, titled "A study of a parametric mixer non-reciprocity dependence on the pump wavelength" by Ana Pejkic, Ron R. Nissim, Evgeny Myslivets, Andreas O. J. Wiberg, Nikola Alic, and Stojan Radic. Chapter 5 includes in part material that has been submitted for publication as it may appear in Progress of Quantum Electronics, titled "High speed parametric processing controlled by few photons," by Ana Pejkic, and Stojan Radic. The dissertation author was the primary investigator, and a primary author of the journal papers and was the presenter of the conference contribution. Lastly, Chapter 5 in part is a reprint of the material as it appears in the Science Journal, volume 345, issue 6195,417-9 (2014), titled "Ultrafast optical control by few photons in engineered fiber" by Ron R. Nissim, Ana Pejkic, Evgeny Myslivets, Bill P.-P. Kuo, Nikola Alic, and Stojan Radic. The dissertation author was the primary investigator, and the co-primary author of this article.

6. Optical switching in the dispersion engineered nonlinear parametric mixer

Static and dynamic measurements introduced in the previous chapter reveal a possibility of controlling a strong pump beam with a signal consisting of few photons only. This photon-photon control mechanism opens new opportunities in optical switch design. The present section is devoted to investigation and demonstration of the fast and energy efficient all-optical switch in the telecom wavelength band (1550 nm).

Key motivation for the fiber parametric mixer (FPM) use in development of a direct light gate is its inherent femtosecond response time, enabling operation at a high bit rate. Of equal importance is the availability of long interaction lengths, relaxing the total energy requirement. Optical switching in a highly nonlinear fiber was previously demonstrated using the continuous wave (CW) pump and the pulsed signal [34]. However, complex dynamics of a short pulse propagation in the vicinity of the fiber zero-dispersion wavelength conceals the four wave mixing process, thus inhibiting the switching operation. With this constraint, demonstration of switching with short pulses (for both the pump and the signal wave) becomes critical. In the following sections we show the transfer response of the FPM switching architecture allowing for a control of a 100 Gbps-fast OOK input.

6.1. Switch modeling

In its simplest implementation, an all-optical switch can be realized, at least in principle, by controlling the pump state in a FPM. The pump depletion is a direct function of the signal input power: even a very weak signal can initiate a strong change of the pump level if the parametric energy exchange is designed efficiently (See Figure 6.1). The operation of the FPM in the saturation regime was first investigated theoretically by Chen [64], and the stability of states was later studied by Cappellini [52]. This simple, three-wave model provided an insight into energy transfer among continuous waves in the nonlinear fiber and is often used to estimate pump depletion levels.

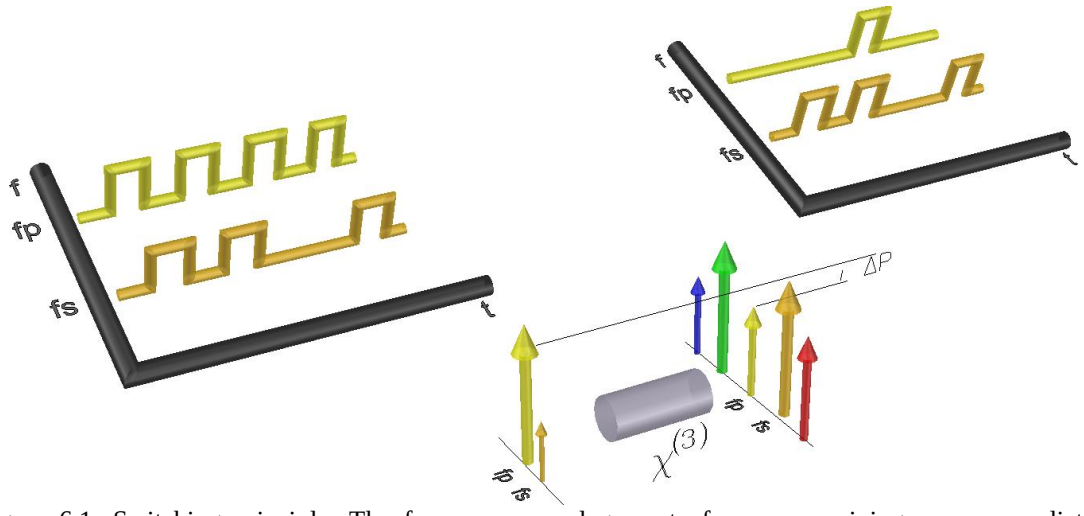

Figure 6.1: Switching principle. The frequency non-degenerate four wave mixing process mediates signal-induced energy depletion of the pump wave. This pump depletion process causes pump pulse switching when these two pulses temporally overlap.

In practice, there are more than three waves participating in the mixing process, thus limiting the predictive accuracy of such approach. Consequently, an increase in prediction accuracy is achieved by relying on a model with a capability to incorporate higher-order terms and account for impairment mechanisms expected in a physical fiber. The broadband nonlinear Schrödinger description, while computationally expensive, accounts for the loss, dispersion fluctuation, multiple-tone generation and is used as a second step in the design process.

The nonlinear Schrödinger equation describing forward propagation of multiple frequency components in a nonlinear fiber is given by [48]:

$$\frac{\partial}{\partial z}A(T) = -\frac{\alpha}{2}A(T) + \hat{D}\,A(T) + \hat{N}\,A(T) \tag{103}$$

where $A(t)$ is the complex envelope of the field, α is the attenuation coefficient, $\hat{D}$ is the differential operator accounting for the dispersion in a linear medium, $\hat{N}$ is the nonlinear operator governing the nonlinear effects. The aforementioned operators are given by the following set of equations:

$$\hat{D} = -\frac{i\beta_2}{2}\frac{\partial^2}{\partial T^2} + \frac{\beta_3}{6}\frac{\partial^3}{\partial T^3} \tag{104}$$

$$\hat{N} = i\gamma\left(\left|A(T)\right|^2\right) \tag{105}$$

While the model supports higher order nonlinear effects and the Raman scattering, these effects were omitted from the simulations shown in this work, because they provide no significant contribution to the system response, but do considerably extend the simulation time.

Two main switch quality parameters are the switching time and the switching energy. In the first step of switch characterization, we investigate the switching time, by estimating the FPM bandwidth. The switching bandwidth of the FPM device is largely defined by the physical characteristics of the fiber. The first step in the bandwidth estimation is the static system response characterization. The simplest technique for the static transfer response investigation relies on the CW pump and the tunable probe, employed to estimate the switch bandwidth. To model the device, the 31.6 dBm CW pump centered at 1554 nm was combined with a white noise source; the noise source representing vacuum fluctuations had a level of fluctuations of 0.5 photons/mode and was a basis for parametric fluorescence generation. The system was analyzed by the NLS solver incorporating the split-step Fourier method [48]. To increase the predictive accuracy of the model, interaction of multiple frequency components was simulated over the 41 THz bandwidth, 3 times wider than the modulation instability bandwidth at a given pump power level. Final result dependence on the simulation bandwidth is negligible, because the effect of parametric fluorescence on pump integrity depends primarily on the modulation instability bandwidth. The pump optical signal to noise ratio (OSNR) was 47 dB, estimated over the 0.1 nm resolution bandwidth, matching the typical OSNR of the amplified 1550 nm diode. The switch transfer response was mapped by varying both wavelength and power of the CW probe in the 1560-1575 nm and -40 dBm to -20 dBm ranges, respectively. The pump-signal interaction along the 520-m-long HNLF with the nonlinear parameter, γ, of 12.3 $W^{-1}km^{-1}$, the propagation loss of 1.1 dB/km and the global zero-dispersion wavelength (ZDW) of 1548 nm was simulated and used to calculate the power of all generated waves. Furthermore, the

HNLF had longitudinal ZDW fluctuations modeled after the experimentally measured fiber possessing the ZDW map shown in Figure 6.2(a). Due to severe effect of the ZDW fluctuations on the FPM, including the longitudinal ZDW profile is critical for an accurate modeling of the system. The experimentally obtained ZDW profile was modeled using 200 different fiber sections of equal length and with constant (but mutually varying) ZDW. The system response was acquired by successively solving the NLS for each fiber section. At the output of the HNLF, the pump was filtered using a 2 nm OBPF and detected. The extinction ratio (ER), defined here as the ratio of the pump power with signal present and absent was calculated and the resulting contour map is plotted in Figure 6.2(b). Note that the simulation results are in agreement with the experiment.

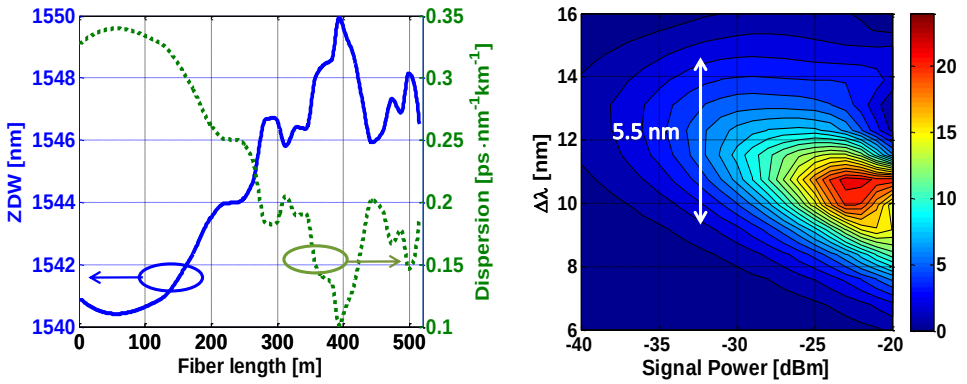

(a) (b)

Figure 6.2: The pump depletion simulated for a given longitudinal ZDW profile. (a) The longitudinal ZDW profile and the corresponding dispersion profile at the pump wavelength, used in the static transfer characterization. (b) Calculated ER power-wavelength contour map. $\Delta\lambda$ indicates wavelength offset between the pump and the control signal.

As seen in Figure 6.2(b), when the signal power equals -30 dBm, the optimum signal wavelength is 1566 nm. Furthermore, this selection guarantees the minimum 3

dB ER across the entire 5.5 nm bandwidth. In other words, the calculation indicates possibility of switch control by 1.4 ps signal shaped by a rectangular pulse with a peak power of -30 dBm, possessing a minimum 3 dB ER at the output. The map plotted in Figure 6.2(b) allows for a straightforward switch design: given the minimum extinction ratio and the desired switch speed (bandwidth), one can uniquely select the control power and the center frequency with respect to the pump.

Having characterized the bandwidth of the system using static analysis, further investigation of the switching response was performed in the time domain with pulsed input. There are several effects characteristic for the dynamic pulse interaction placing an additional challenge in a switch design, the first one being the dispersion induced pulse breakup. Namely, it is known how pulse propagation near the zero dispersion frequency is affected by the third-order dispersion [65], [66]. An interplay between the nonlinearity and the dispersion causes splitting of a pulse initially centered at the ZDW to a frequency down-shifted soliton-like wave and an up-shifted dispersive wave, leading to clear frequency separation. Wai et al. [66] suggested a solution to this impairment by controlling the pump position with respect to the ZDW or the pulse duration. Since the system bandwidth is drastically affected by the pump spectral position, it is preferable to refrain from using the pump wavelength as a free design parameter. Any pulse breakup could be avoided by increasing the pump pulsewidth, thus limiting the pump repetition rate and the device switching time. Another, preferred way to circumvent this impairment is to use a fiber with specifically tailored dispersion over the wavelength range of interest. For the purpose of this experiment, we chose to the minimize soliton radiation impairment by limiting the switching speed to 100 GHz,

dictating a 5 ps gating window. Other, equally important effects affecting switch performance are the walk-off of the interacting waves, soliton pulse compression and evolution. The average walk-off parameter d_{12} is estimated from [48], [49] $d_{12} = |\beta_2(\omega_p)\Delta\omega + \beta_3(\omega_p)\Delta\omega^2/2|$, where $\beta_2(\omega_p) = -1.9\cdot10^{-28}$ s^2/m and $\beta_3(\omega_p) = 4.1\cdot10^{-41}$ s^3/m, and is found to be 0.003 ps/m at the signal frequency and 0.0002 ps/m at the idler frequency.

The switching response is next characterized with a pulsed input. The 5.4 ps pump pulses with 100 ps period and 31.2 dBm peak power, were centered at 1554 nm. The signal consisted of transform-limited 2.3 ps pulses with 10 GHz repetition rate and was positioned at 1565 nm. The chosen temporal width of the signal pulse guarantees the temporal overlap of the interacting waves along propagation, however some extinction ratio deterioration, compared to the CW operation, is certainly expected. The signal peak power was varied from -30 dBm to -14 dBm using 4 dB steps while keeping the rest of the simulation parameters unchanged with respect to the static case. At the output of the HNLF, the pump was filtered using a 2 nm OBPF and both time and frequency domain outputs of the device were subsequently analyzed and plotted in Figure 6.3 and Figure 6.4.

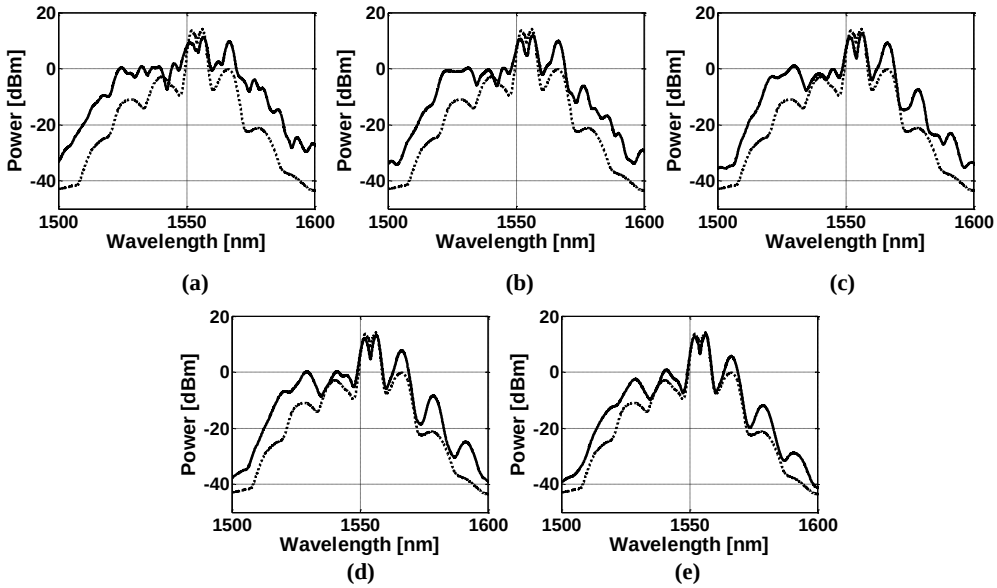

Figure 6.3: Simulated spectrum at the output of the switching system. Case when the signal is not present at the input (dotted curve) and the case when the signal is present (solid curve). The control signal peak power corresponds to: (a) -14dBm; (b) -18dBm; (c) -22dBm; (d) -26dBm; (e) -30 dBm.

The switching is achieved by energy transfer from the pump to the signal, the idler and higher order mixing waves via the four wave mixing process, as clearly seen in the spectra in Figure 6.3. In the absence of the signal, represented with dashed curve, only amplified spontaneous emission noise is present. Presence of the signal containing few photons within the envelope of the pulse is clearly distinguished from the noise as seen in Figure 6.3(e).

Time domain representation is plotted in Figure 6.4; the averaged pump waveform with the signal present and absent and the two corresponding histograms are included for completeness. These histograms were generated from 56730 samples, and obtained by repeating the NLS simulation seeded by independent noise source realizations, while maintaining the deterministic simulation parameters. We note that the main purpose of the histogram is ER and error estimation, rather than emphasis on

output pump wave statistical properties. The histogram shape strongly depends on the pump peak power, pump excess noise, the detection system impulse response (not included in the simulation) and the temporal width of the histogram window. Therefore, the study of the system statistical properties requires strict system characterization and might be the topic of the future work. To mimic experimental conditions, the samples were collected at the pulse center within a 1.5 ps timing window. The results indicate switching capability with a 2.2 attojoule-strong signal, as seen in Figure 6.4(e). Although not shown here, it is important to note that the noise performance improvement is achievable by the pump power reduction, with modestly higher signal powers. Finally, we emphasize that the case calculated here is still very far from the optimal switching design requiring specifically tailored fiber characteristics.

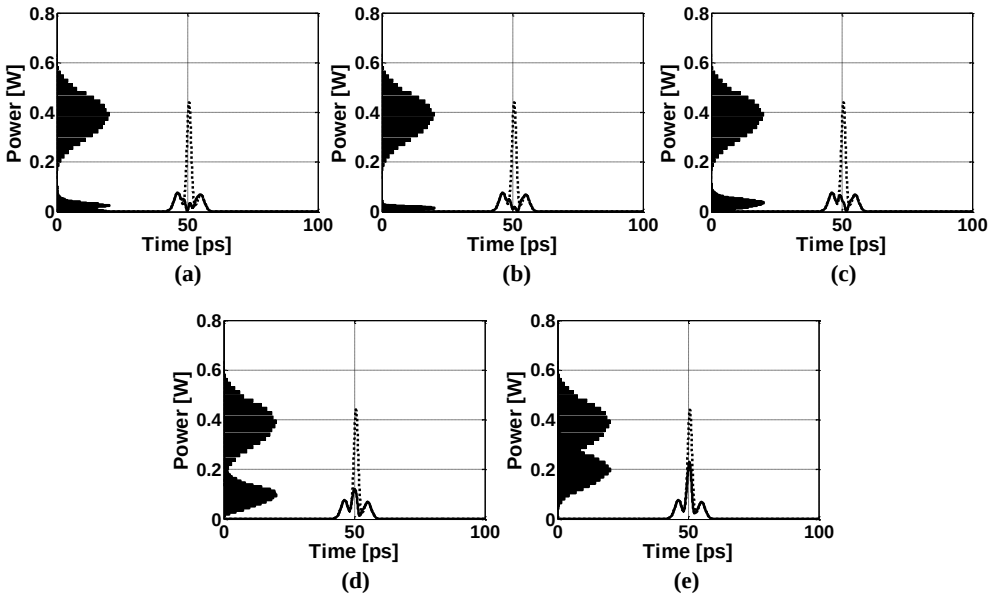

Figure 6.4: Simulated time response of the switching system. The case when signal is not present at the input (dotted curve) and the case when the signal is present (solid curve). The control signal peak power corresponds to: (a) -14dBm; (b) -18dBm; (c) -22dBm; (d) -26dBm; (e) -30dBm; with corresponding histograms.

In the final system characterization step, the switching performance was completed by measuring the ER. The average ER and the corresponding error were calculated using standard error estimation [67], [68]. The relative frequency f_i, the mean μ and the standard error estimate ε of two output power levels of the pump were calculated using histograms:

$$f_i = \frac{n_i}{n} \tag{106}$$

$$\mu = \sum_i m_i f_i \tag{107}$$

$$\sigma^2 = \sum_i \left(m_i - \mu\right)^2 f_i \tag{108}$$

$$\varepsilon = t\sqrt{\frac{\sigma^2}{n}} \tag{109}$$

where n is the total number of points and n_i is a number of points at the power level m_i and t is a number given by Student t distribution. For n = 56730 and 84% confidence interval, t number equals 1, while for 97.7% confidence interval, t = 2. Extinction ratio and the corresponding error were calculated using the following equation set [27]:

$$ER = \frac{\mu_1}{\mu_0} \tag{110}$$

$$\sigma_{ER}^2 = \left(\frac{1}{\mu_0}\right)^2 \sigma_1^2 + \left(\frac{\mu_1}{\mu_0^2}\right)^2 \sigma_0^2 + 2\left(\frac{\mu_1}{\mu_0^3}\right)\sigma_{01} \tag{111}$$

$$\sigma_{01} = \frac{\sum_i \left(m_{1i} - \mu_1\right)\left(m_{0i} - \mu_0\right)}{n} \tag{112}$$

$$\Delta ER = t\frac{\sigma_{ER}}{\sqrt{n}} \tag{113}$$

$$ER_{dB} = 10\log_{10}(ER) \tag{114}$$

$$\Delta ER_{dB} = \frac{10\Delta ER}{ER\ln(10)} \tag{115}$$

Additionally, the relation between the signal power and the photon number (energy) is given by:

$$N = \frac{P_{ave}T}{h\nu} \tag{116}$$

where T is the period of the signal, h is the Planck constant and ν is the signal frequency. The signal energy is calculated as the product of the signal average power P_{ave} and the period T ($E_s = P_{ave}T$).

Results of this characterization, for different input signal pulse energies are presented in the Table 6.1. The error in the ER measurement is represented with a 97.7% confidence interval. A measurement highlight is switching with a control pulse containing 17 photons on average, resulting in the 2.86 dB average ER.

To estimate the switching speed we analyze the pulse evolution. Because of the high input peak power and operation close to the ZDW of the fiber in the anomalous dispersion regime, the pump evolves into a high order soliton-like pulse. On the one hand, the pump evolution of this type has the advantage of pulsewidth reduction and peak power enhancement. The reduced output pulsewidth is important for temporal response of the system, being limited by the input pulsewidth only; higher peak power increases the system ER . On the other hand, higher order soliton pulses suffer from increased peak power fluctuations, due to the peak-power-dependent pulse compression, leading to increased pump output peak power fluctuations, as compared to the CW regime. Therefore, the limiting factor to switching speed increase is the input pulsewidth, allowing operation at 100 Gb/s.

Table 6.1: Optical switching simulation: summary of results

Pump peak power 31.2dBm			
Signal peak power [dBm]	Average number of photons	ER [dB]	Signal energy [aJ]
-30	17	2.86±0.02	2.2
-26	42	5.91±0.03	5.4
-22	110	10.30±0.08	14
-18	270	14.1±0.2	34
-14	670	12.3±0.2	84

In summary, our model predicts 100 GHz switching capability of the described system. While pump power has moderate power of 31.2 dBm, signal energy is significantly lower, reaching 2.2 aJ with 3 dB ER.

6.2. Experimental results

The theoretical system modeling presented in the previous section implies the possibility of pump switching at 100 GHz rate with 2.2 aJ-strong control signal. In the following sections we present the experimental verification of the predicted switching performance.

6.2.1 Picosecond switching at 10 GHz rate

After the design outlined in the previous section, the switching device was experimentally realized with the setup shown in Figure 6.5.

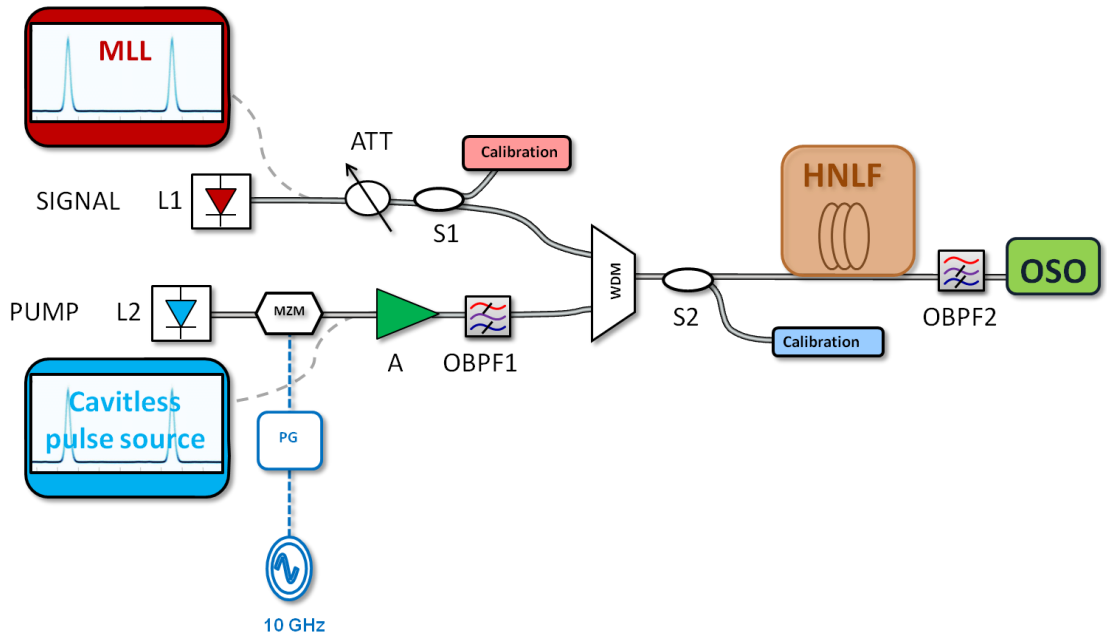

Figure 6.5: The experimental setup for switch characterization operated at 10 GHz rate. Acronyms: L-laser; MZM - Mach-Zehned modulator; PG- Pattern generator; A- Amplifier; OBPF-Optical band-pass filetr; VOA- variable optical attenuator; S-splitter; WDM - wavelength division multiplexer; HNLF-highly nonlinear fiber; OSO- optical sampling oscilloscope.

The temporal response of the system was characterized by positioning the pump and the signal according to parameters obtained from the static measurement and dynamic simulations. To capture the fast transients, the detection system incorporated a wide bandwidth optical sampling oscilloscope (OSO). The pump was generated using a cavity-less pulse source [62] centered at 1554 nm, producing 5.4 ps long pulses with a repetition rate of 10 GHz. The control signal was represented by a mode locked laser (MLL) at 1564 nm, with a pulsewidth of 2.4 ps and repetition rate of 40 GHz; its power was controlled by a variable optical attenuator (VOA). The pump peak power was

calibrated at the input of the HNLF and was set to 31.7 dBm with an error of $\pm$ 0.7 dB using a VOA. The average power of the control pulse was measured with an optical power meter at the calibration point in the signal arm, depicted in Figure 6.5; the calibration accounted for the power ratio between the measurement point and the input of the HNLF. At the output of the HNLF, the pump was filtered with two consecutive 2 nm OBPF, and was attenuated before being detected by the OSO.

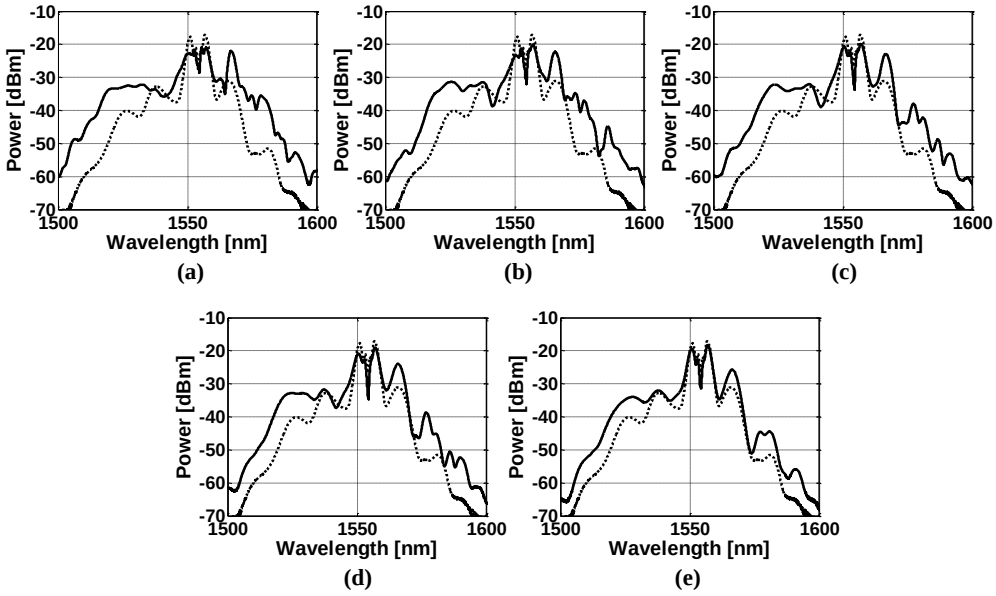

Figure 6.6: Measured spectrum at the output of the switching system. The case when signal is not present at the input (dotted curve) and the case when the signal is present (solid curve). The control signal peak power corresponds to: (a) -14.5dBm; (b) -18.5dBm; (c) -22.5dBm; (d)-26.5 dBm; (e) -30.4 dBm.

Experimental results from temporal and spectral domain measurements are shown in Figure 6.6 and Figure 6.7. We note an excellent agreement between simulation results shown in Figure 6.3 and Figure 6.4, and measurements, both in the temporal and the spectral domain. In the absence of the input signal, represented with a dashed curve in Figure 6.6, the output of the switch is characterized by the amplified

spontaneous emission noise. As predicted by the model, the presence of a weak, <N>=17-photon pulse [corresponding to Figure 6.6(e)] is clearly distinguished from noise in the spectral measurement.

The results of temporal response measurements are presented in Figure 6.7 where averaged output of the device, in presence and absence of the input (control) signal is plotted. Figure 6.7 also shows corresponding histograms for high- and low-level outputs with both input conditions. In this measurement, the high-level histogram experiences asymmetry coming from the noise induced pump depletion. The difference in the measured and the simulated histogram is attributed to the error in the pump peak power calibration, the temporal width of the histogram widow, pump excess noise and the impulse response of the system. The exact matching of the histogram shape requires a rigorous study and is out of the scope of this work. By varying the control signal energy from 2.2 aJ to 84 aJ, the experiment indicates pump switching with the ER ranging between 3.1 dB and 7.7 dB.

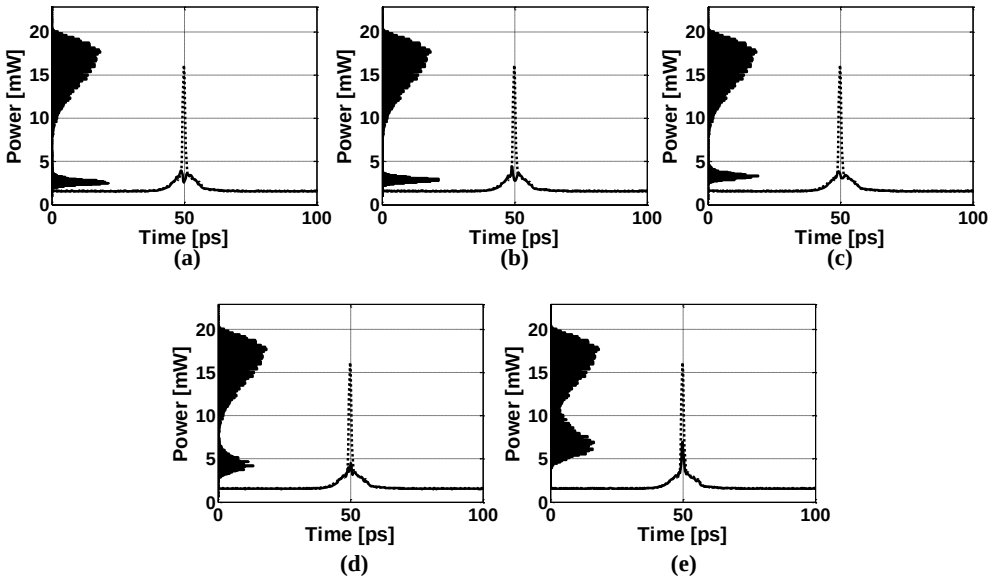

Figure 6.7: Measured temporal response of the switching system**.** The case when signal is not present at the input (dotted curve) and when the signal is present (solid curve). The control signal peak power corresponds to: (a) -14.5dBm; (b) -18.5 dBm; (c) -22.5dBm; (d) -26.5 dBm; (e) -30.4 dBm, with corresponding histograms.

The ER of the pump was measured following the method described in this section, and the error was estimated using the procedure described in Appendix A; The pump power was maintained at constant peak power (31.7 dBm), during the ER measurement. Results are summarized in Table 6.2 and Figure 6.8. In Table 6.2, results are presented with an error given within the 97.7 % confidence interval.

The pump input pulse energy was constant and maintained at 8.1±0.8 pJ throughout the measurement. In the presence of the control signal, the pump beam was switched and the ER of 3.10±0.03 dB and 5.40±0.05 dB was measured when the signal energy was at 2.2±0.2 aJ and 5.4±0.5 aJ level respectively. Equivalently, this corresponded to an average of 17±2 and 42±4 photons per control (signal) pulse. At

higher signal peak powers, we observe pump power noise reduction, as expected from the nonlinear transfer function of the system.

Table 6.2: Optical switching experiment: summary of results. Acronyms: P_{ave}-signal average power, P_{peak}-signal peak power, ER-extinction ratio, N-average photon number per pulse.

Pump peak power 31.7dBm				
P_{ave} [dBm]	P_{peak} [dBm]	ER [dB]	N	Signal energy [aJ]
-40.6±0.7	-30.4±0.7	3.10±0.03	17±2	2.2±0.2
-36.7±0.7	-26.5±0.7	5.40±0.05	42±4	5.4±0.5
-32.7±0.7	-22.5±0.7	6.69±0.07	110±10	14±2
-28.7±0.7	-18.5±0.7	7.37±0.08	270±30	34±3
-24.7±0.7	-14.5±0.7	7.71±0.08	670±60	84±8

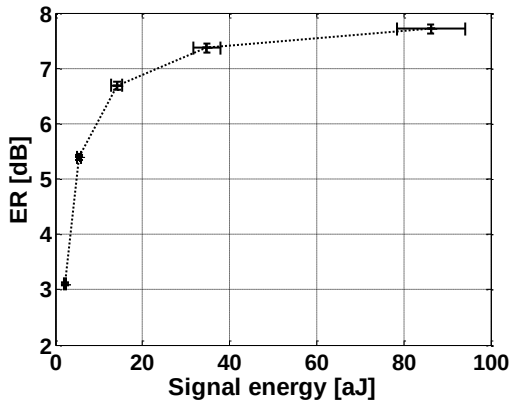

Figure 6.8: Measured extinction ratio vs. signal energy

At high control powers, the experimentally measured pump ER was lower than that predicted by the theory: at -22 dBm input signal, this difference was nearly 3dB. The main reason for discrepancy is attributed to the low sensitivity and the limited dynamic range of the OSO, as well as the timing jitter of the pump pulse used in the experiment.

As a final observation, we note that in contrast to the CW case, on the same platform [57], where the pump state is controlled with an average of 4 photons, this task becomes distinctly more challenging with a pulsed pump. The ER close to 3 dB has been achieved for a 2.2 aJ signal in this work, while the similar effect was accomplished with half the signal energy in the CW pump case. This discrepancy can be relieved by a further effort in fiber dispersion engineering.

6.2.2. Picosecond switching at 100 GHz rate

In the previous section, the switch performance was investigated in the high pump energy regime and its 100 GHz operation potential revealed. In this section, we show a confirmation of the 100 GHz switching capability using the experimental setup shown in Figure 6.9. A high repetition rate pulse source is created with two injection locked lasers [69]. The pump centered at 1552 nm and the signal positioned at 1541 nm, both with 100 GHz speed, are guided into the highly nonlinear fiber ($HNLF_2$) acting as a switching element. Frequency and time domain representations of the switch output are depicted in Figure 6.10.

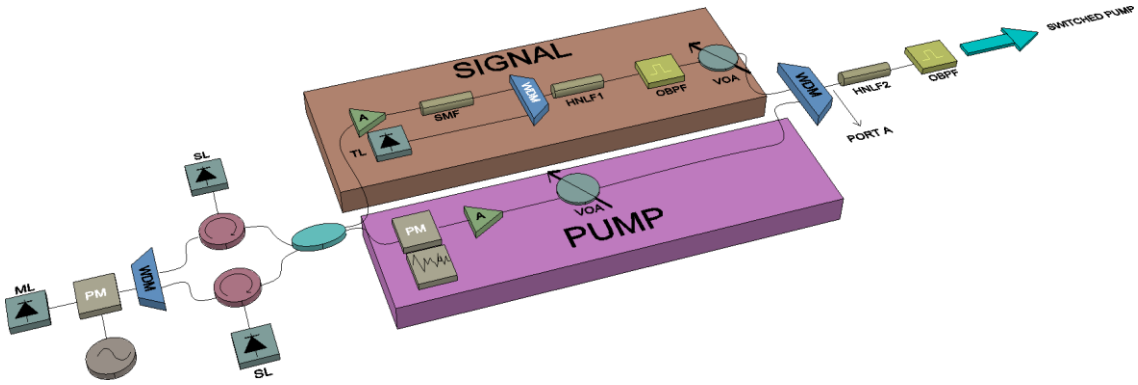

Figure 6.9: Experimental setup for the switch characterization operated at 100 GHz rate. The pump and the signal energy level is measured at a port A. Acronyms: ML, Master Laser. PM, Phase modulator. A, amplifier. WDM, Wavelength division multiplexer. SL, Slave laser. C, Circulator. TL, tunable laser. SMF, Single Mode Fiber. HNLF, Highly Nonlinear Fiber. OBPF, Optical Band Pass Filter. VOA, Variable Optical Attenuator.

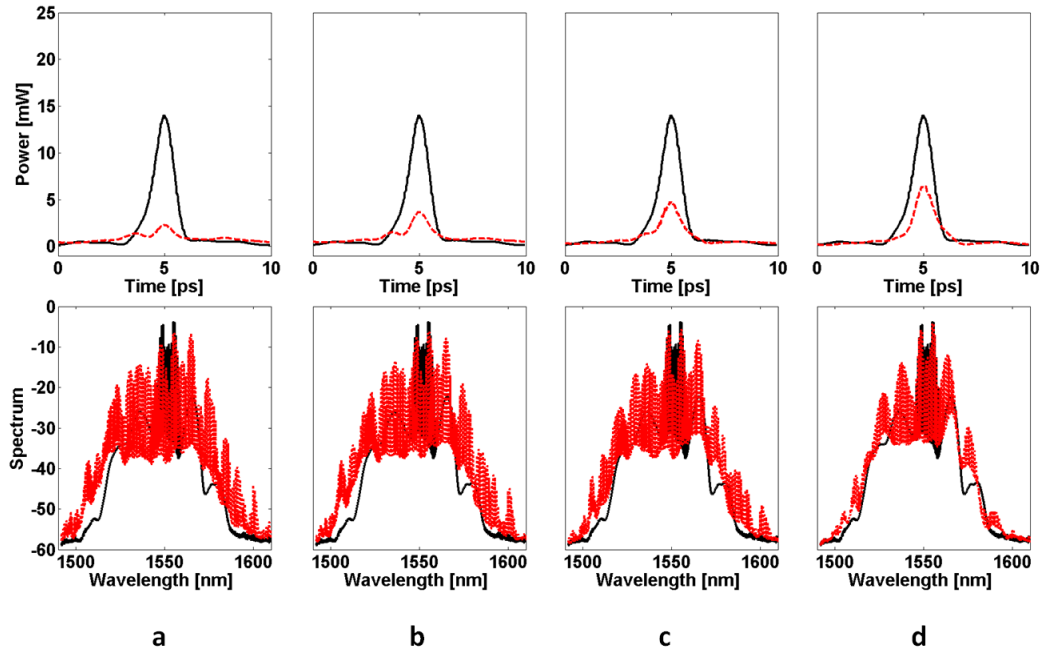

Figure 6.10: Pump bit-level switching operated at 100 GHz rate. The four wave mixing spectrum (down) and the pump pulse (up) at the output of the system with no signal at the input (black, solid curve) and with a signal (red, dotted curve) containing and average of: (a) 290; (b) 110; (c) 44; and (d) 17 photons per pulse. The average pump power was 29.7 dBm, corresponding to a 9.3 pJ pump energy per pulse.

Following the common approach to switch characterization, one could confirm viability of 100 GHz switching speed in this architecture, having 2.7 dB and 7.8 dB

extinction ratio achieved with 2.4 aJ and 40 aJ control signal energy respectively; this is indeed predicted by low-speed measurements. However this switch characterization method offers no insight into switched signal integrity and, therefore, practical application potential. Consequently, the next section is dedicated to investigation of the switched signal amplitude fidelity by performing the standard Bit Error Ratio (BER) measurement.

6.2.3. Switched signal amplitude fidelity

While the proposed switching scheme has numerous benefits, it is also a subject to certain limitations. Regarding the ER, the signal and the idler walkoff have a significant contribution its degradation. Depending on the fiber dispersion profile, the group velocity of the pump, the signal and the idler differ, ultimately resulting in a measurable finite temporal misalignment. Although increasing the signal pulsewidth might relieve the influence of the walk-off on the ER, it also elevates the signal energy. Thus, reliance on a HNLF with a low local dispersion over the wavelength range of interest is a preferred way of overcoming the described issue.

In addition to the aforementioned ER impairment mechanism, the pump amplitude noise is directly converted to the signal amplitude noise and further transferred to higher order idlers via gain fluctuation. Finally, it is the coupled signal/idler phase noise (via the XPM and FWM), impairing the system performance by means of a broadened switching window. Additionally, the pump phase noise is equally important because it leads to amplitude-phase noise conversion via the SPM and the

XPM, a non-negligible penalty in the high-saturation regime. In general, if not controlled, the phase noise of the three original waves present at the HNLF input decrease the overall ER when working with short signal pulses.

The output pump amplitude fidelity is highly sensitive to the mixer figure of merit (defined by the γPL product) and the input signal power, imposing a direct tradeoff between the high ER and the pump amplitude integrity at low input signal power levels. Furthermore, the output pump integrity additionally depends on the pump signal to noise ratio, pump excess noise, dispersion properties of the fiber and the pump pulse width. Lastly, while the effect of the parametric fluorescence on the switching performance strongly depends on the described parameters, one can certainly expect a $\gamma PL >> 10$ to result in the absence of the two well defined states. However, these limitations can obviously be controlled by reducing the pump power level.

The switch limitation difficult to predict by the static analysis comes from the third order dispersion induced pulse breakup. Indeed, in the presence of a finite β_3, the switching speed is limited by the input pump pulsewidth, and was found to correspond to 5.4 ps at the power level used in this experiment (31.7 dBm). This limitation can, in principle, be circumvented by engineering the HNLF with a tailored high-order dispersion over the wavelength range of interest.

In view of the switching extinction ratio, it is important to understand the limits on it by noise. Hence, the BER is a standard measurement offering insight into switched signal integrity. Significance of the BER measurement is clearly noticed in the recent publication of the optical switching device [70], where the device with the 8 dB extinction ratio experienced the BER minimum of 10^{-3}. Although important, the

extinction ratio alone offers no rigorous switched signal fidelity description; Nevertheless, the BER measurement is often ignored in recent publications.

To take into account the BER tester speed, we use the cavity-less architecture [62] for the pump and the signal pulse source operated at 10 GHz rate, and keep the pulse widths to 5 ps. The signal is intensity modulated in the Mach-Zehnder modulator with a 2^7-1 long pseudo random bit sequence (PRBS). To eliminate the effect of the preamplified receiver noise on the BER measurement, we keep the average power into the preamplifier and the detector constant, while varying the pump and the signal power into the highly nonlinear fiber.

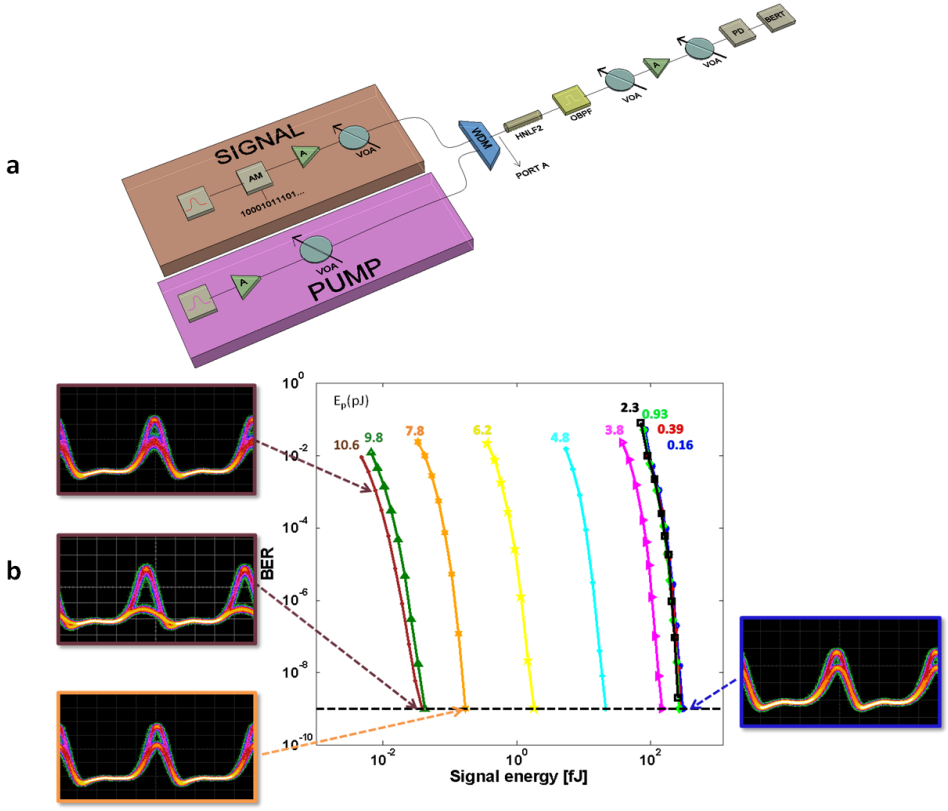

Figure 6.11: The bit error ratio measurement at 10 GHz rate. a) The experimental setup for the bit error ratio measurement. The pump and the signal energy level is measured at the port A. Measurements are conducted under identical operating conditions, corresponding to 5 ps the pump and the signal pulse width and constant power into the preamplified receiver. b) Bit error ratio measurement for different input pump and signal energy.

We also note that the reported power levels correspond to the power before the coupling loss, thus the power coupled into the fiber is 0.4 dB lower than the reported value.

This simple measurement method not only clarifies the error-free performance of the investigated switching architecture, but also reveals the switching dynamics evolution, as represented in Figure 6.11. In the high pump energy regime of 10.6 pJ/pulse, the error-free performance is achieved with as low as 38 aJ/bit signal energy, corresponding to 300 photons on average. Furthermore, the BER of 10^{-3} is reached with 7.6 aJ/bit signal energy, equivalent to only 60 photons on average. In this operating regime, the switching time is limited by the dispersion-induced pulse breakup to 5 ps. Performance at pump energies higher than those reported here is limited by the error floor originating from the noise-induced pump depletion. To achieve the same performance with the lower pump energy, it is necessary to increase the control signal energy. The error-free switching of a 7.8 pJ/pulse pump is feasible with a 170 aJ/bit signal energy. Finally, for the pump energy of 157 fJ/pulse, the error free performance was realized with a 298 fJ/bit signal energy and the BER of 10^{-3} with a 130 fJ/bit signal energy. It is worth noting that latter energy levels are comparable to recent reports of cavity switch architectures [32], [33], [70]; Even more importantly, this architecture preserves switched signal integrity, as demonstrated with BER measurements. In the low pump energy operating regime, the switching mechanism is dominated by an interplay of the four wave mixing process and the cross-phase modulation [71]. In this regime the pump pulse width shorter than 5 ps can be used and the extinction ratio can be further improved in a different system design, as discussed in [71]. Additional

feature of this experiment is increase in the switching extinction ratio with the pump and the signal energy increase, however this does not necessarily result in improved switched signal amplitude fidelity. This is clearly demonstrated in Figure 6.11(b) where two operating points having a similar ER significantly differ in the BER value. Our results clearly demonstrate that the ER alone offers incomplete switch performance characterization, making the BER critical measurement in the device portrayal.

6.3. Chapter summary

The aforementioned limitations are the major cause of performance trade-offs. However, if operated within the described limits, the switch performance is remarkable. With 100 GHz speed potential, the errorless switching is achieved at different pump-signal energy ranges. Ranging from 10 pJ pump- and 2 aJ signal-energy to sub-picojoule pump and signal energy, this device offers multitude of operating possibilities with errorless performance. Finally, contrary to well accepted notion of high energy requirement in $\chi^{(3)}$ structures, this switch offers error-free operation at energy levels comparable to those in cavity-based devices.

Chapter 6 in part is a reprint of the material as it appears in the Optics Express Journal, volume 22, issue 19, 23512-23527 (2014), titled "All-optical switching in a highly efficient parametric fiber mixer: design study" by Ana Pejkic, Ron R. Nissim, Evgeny Myslivets, Andreas O. J. Wiberg, Nikola Alic, and Stojan Radic. Chapter 6, in part is currently being prepared for submission for publication of the material by Ana

Pejkic, Evgeny Myslivets, Nikola Alic and Stojan Radic. The dissertation author was the primary investigator, and the primary author of these articles.

7. Parametrically-aided few photon detection at 10 Gb/s and beyond

With a rapidly growing number of users requiring secure communications, the interest in development of near-infrared single- and few-photon detectors is increasing constantly. Although quantum information applications have driven the recent advance of single-photon detector technology, many applications in spectroscopy, medicine and remote sensing, would certainly benefit from such a technological prospect.

Presently, these devices rely on photon-to-electron conversion and subsequent generation of a macroscopic signal with minimal noise generation. The bandwidth of the-state-of-the-art single-photon detectors is, therefore, limited to sub-Gigahertz ranges [26]. To operate at higher rates, current single- and few-photon detectors depend on multiplexing schemes, inevitably leading to performance degradation; this is due to the direct scaling of the detection efficiency, η, as η^N, where N is the required number of detectors. Despite the considerable progress, single- and few-photon detectors are limited to operation at sub-Gigahertz range. In this chapter, we introduce a novel method for few-photon detection based on the photonic sampler and mature telecommunication preamplified receiver technology, operating at 10 GHz rate and beyond.

7.1. Phase insensitive preamplified receiver: performance trade-offs

The role of the phase insensitive preamplified receiver in modern telecommunication systems is undisputable: it has long been recognized for its superior noise performance with respect to its direct detection alternatives [72] and simplicity of implementation with respect to its phase-sensitive counterparts [73]. However, when the signal energy approaches a few-photon limit, the amplified spontaneous emission noise becomes dominant performance deterioration mechanism, difficult to control. The fundamental noise limits are well investigated and statistical distributions, describing the preamplified receiver noise performance, identified. Namely, the signal, initially Poisson distributed, is known to follow the Laguerre distribution after amplification; the amplified spontaneous emission, on the other hand, is Bose-Einstein distributed [72]. Although the exact performance prediction requires quantum analysis, this statistical approach can still be employed for performance estimation [74].

To estimate the ideal detector performance (also referred to as a quantum noise limit), we employ the receiver operating characteristics (ROC) curve for an average photon number per observation interval N = 1, detector quantum efficiency η=1, spontaneous emission factor n_{sp} = 1, number of modes m = 1 and signal gain G = 100. In estimating the receiver operating characteristics, the dark count probability and the detection efficiency definitions are adopted from [75]. The dark count probability is defined as the probability of sending the logical "zero" bit state and detecting the "one" state, *P(1|0)*, while the detection efficiency is identified as the probability of sending

the logical "one" and receiving the logical "one" state, *P(1|1)*.Results are presented in Figure 7.1.

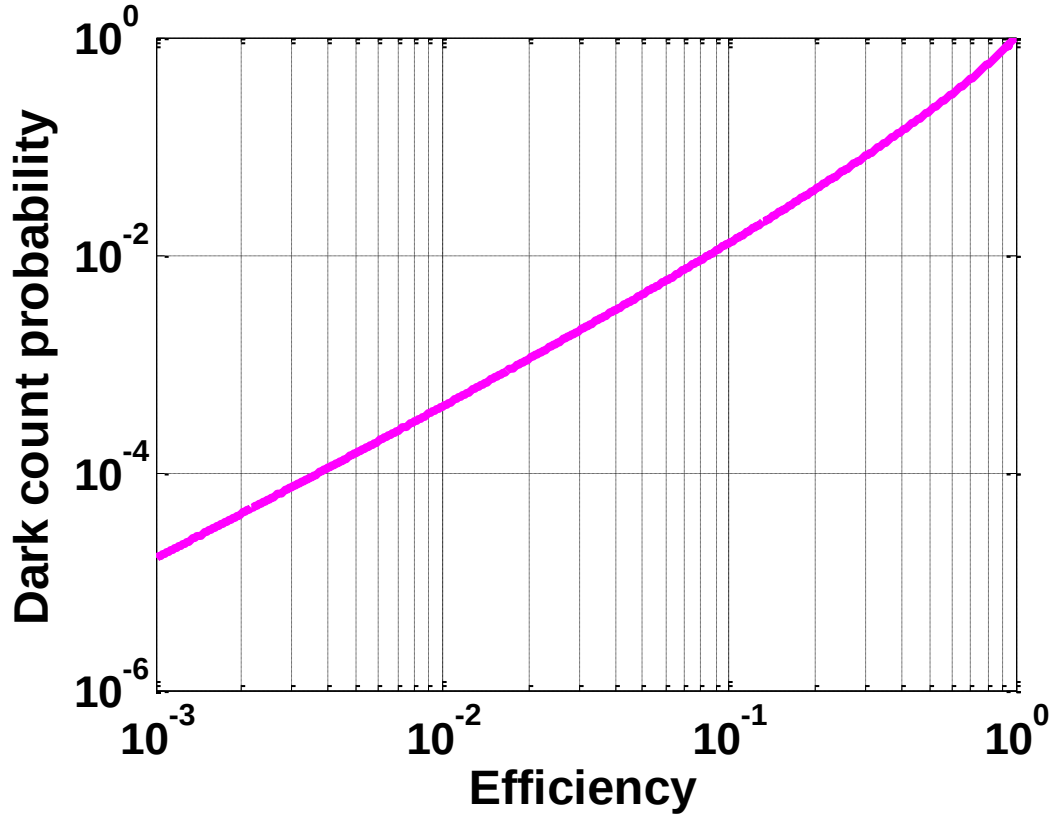

Figure 7.1: Theoretical receiver operating characteristics for the phase insensitive preamplified receiver. Average photon number is <N> = 1.

Variation of the threshold value allows receiver operation in a multitude of operating ranges. The detection efficiency η_{tot} = 8.5% is obtained for the dark count probability P_d = 0.01. The lower dark count is also achievable, but at the expense of the decreased detection efficiency: P_d = 0.001 is attained with η_{tot} = 1.85%, while P_d = 0.0001 is reached with η_{tot} = 0.37%. This single photon detection method has an

obvious limitation: the detection efficiency higher than 10% can only be accomplished with a disadvantage of the high dark count probability (P_d > 0.01). However, the performance increases with a rise in the average photon number, making the method attractive for few-photon detection.

To compare the detector performance with the available technology, we revisit the widely accepted detector Figure of Merit, introduced in Chapter 1.

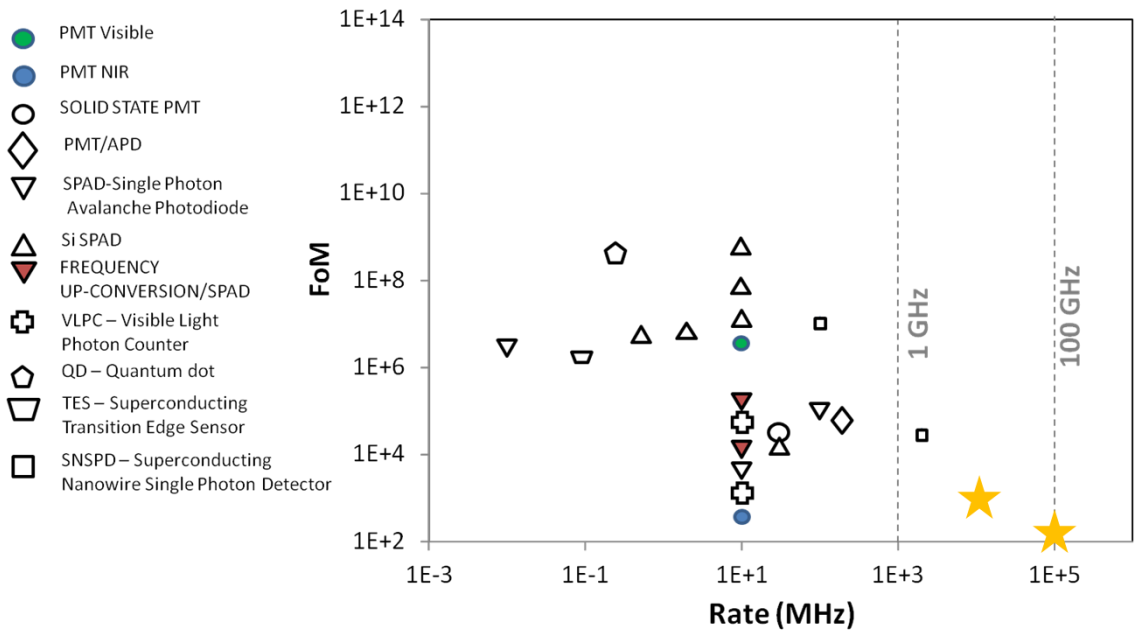

Figure 7.2: Single-photon detector technology comparison. Detector Figure of Merit as a function of maximum detector count rate. Yellow star represents this work.

Figure 7.2 represents the Figure of Merit represented as a function of the maximum count rate of the available single photon detector technology; the yellow star symbolizes preamplified receiver technology. It is clear that the Figure of merit decreases with speed, due to their inverse relation. The parameters used in the

preamplified receiver performance estimation are as follows: dark count probability P_d = 0.001, detection efficiency η_{tot} = 1.85%, timing jitter 1 ps and speed 10 GHz and 100 GHz respectively. It is clear that this technology covers the speed, currently out of reach of available technology. Additionally, the timing jitter depends largely on the pulse source employed. We use the value of 1 ps, similar to the pulse duration used in the experiment, however, this value is largely overestimated. One of the most interesting features is that the even at orders of magnitude higher speed the preamplified receiver can perform similarly to some existing single photon detector technology. Note that the detection efficiency definition varies in these reports, so the actual performance can be inferior to the reported.

7.2. Photonic sampler aided preamplified receiver: Enhancing a detection of a picosecond few-photon event

The main challenge in the detection of the picosecond optical event is the limited bandwidth of the state-of-the-art optical receiver technology. To circumvent the speed problem, current architectures rely on equivalent-time photonic sampling techniques with capability to resolve sub-picosecond events. While an equivalent-time measurement is important, its practical use is limited, because many disciplines require real time detection of fast, low-duty cycle events. To investigate the detection of such a signal in the real-time, we rely on conventional preamplified receiver technology,

consisting of an Erbium-doped fiber amplifier (EDFA), an optical filter, a detector, an electrical amplifier, an electrical filter and a real-time oscilloscope.

Previous theoretical and experimental work relates a preamplified receiver performance to three parameters: the optical filter bandwidth, the electrical filter bandwidth and the duty cycle [76]; having these parameters matched to the input pulse increases the receiver sensitivity. However, in many applications involving picosecond pulses, this task is impossible to accomplish, because the available receiver bandwidth is limited to 100 GHz range or less. To gain insight into the direct detection fundamental limits, we start with the detection process description. Namely, the result of the photon-to-electron conversion in the direct detection process is the average current $<I_{dd}(t)>$, typically represented as a product of the responsivity parameter R and a convolution of the optical power $P(t)$ with the detection system impulse response $h(t)$ [77]

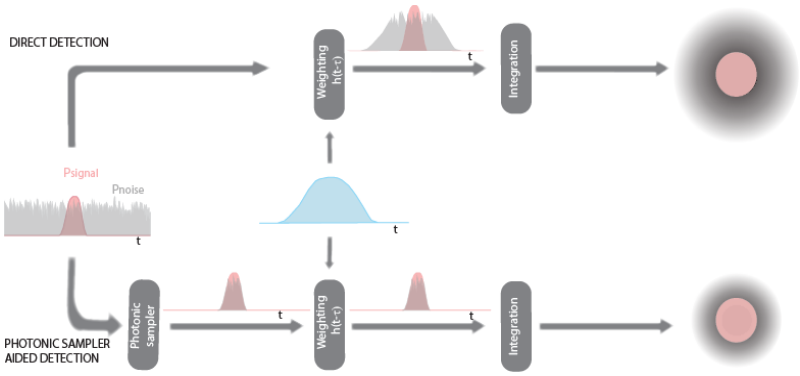

Figure 7.3: Photonic aided preamplified receiver operating principle. Conventional preamplified receiver: Short pulse (red) with high amplified spontaneous emission noise (grey) is falling onto a detector with an impulse response h(t) (blue). The average current can be represented as the integral of the sum of the signal and the noise over the detector impulse response time *h(t)*, corresponding to the area below the signal and noise pulses. Photonic sampler aided preamplified receiver: Short pulse (red) with high background noise (black) is photonically sampled prior to detection. The average current can be represented as the integral of the sum of the photonically sampled signal and noise over the detector impulse response time *h(t).*

$$< I_{dd}(t_0) >= R\int_{-\infty}^{\infty} P(\tau)h(\tau - t_0)d\tau = R\int_{-\infty}^{\infty} P_{signal}(\tau)h(\tau - t_0)d\tau + R\int_{-\infty}^{\infty} P_{noise}(\tau)h(\tau - t_0)d\tau \qquad (117)$$

If signal duration is much shorter than the detector impulse response time, *h(t)*, and if the noise is dominated by the optical noise rather than the electronic, a significant amount of optical noise is integrated in the detection process; this is typically the case in the preamplified few photon detection [78]. To increase the signal-to-noise-ratio (SNR), the receiver bandwidth should match the signal bandwidth [76]. Unfortunately, this sensitivity improvement method is sometimes unfeasible, because the detector bandwidth is restricted to tens of Gigahertz, thus limiting the pulse duration to tens of picoseconds or longer. Here, we propose an alternative way to approach this problem by reducing the amount of noise outside the signal duration window prior to detection, by a time windowing function. Similar method, namely the time-domain filter, was introduced previously in narrow-band-classical-signal detection as means of amplified spontaneous emission noise and timing jitter reduction [79], [80], [81]. Serving as a mainstay for this purpose, a photonic sampler can be implemented to increase the preamplified receiver sensitivity. In this process, noise is being time constrained to an interval corresponding to the signal duration, as depicted in Figure 7.3. Thus, any additional noise within the bit slot, typically deteriorating the detection process, is eliminated. This method allows for the detection of a pulse with duration proportional to the inverse of the amplifier bandwidth, while being limited only by the fundamental statistical properties of the amplified light wave [72].

The choice of the sampler pulse width is critical, because this parameter affects the performance improvement. If the sampling pulse shape follows that of the signal, the optimum performance is obtained when the two pulse widths are matched. On the one hand, if the sampling pulse with is wider than that of the signal, the excess noise will be added to the signal in the detection process. On the other hand, if the sampling pulse is shorter than the signal, no significant bit error ratio performance improvement is expected compared to the matched case, because the signal and the noise energy (or current) ratio remains constant; note, however, that this method has been used for the timing jitter reduction [82]. The optimum sampler temporal width should match that of the signal, because the optical filter introduces correlation in the noise samples [83] over the short time interval determined by the filter impulse response. However, in the absence of proper optical filtering, the photonic sampler can additionally improve the receiver performance, by taking multiple samples over the signal duration and adding them coherently. In this case, the noise correlation time is shorter than the signal duration, thus allowing for the noise averaging within a signal pulsewidth.

7.3. Real-time detection of a repetitive picosecond few photon event: experimental demonstration

Photonic sampling was introduced as a promising method for improving Analog-to-Digital Converters [84], [85], detection of time multiplexed telecommunication signals [86] and a wide-bandwidth equivalent time sampling [87]. In these applications, the main advantage with respect to conventional technology was

referenced to the speed and the timing jitter improvement. The present work extends the photonic sampler role to detection of the low duty cycle few photon event with a picosecond duration. We employ a photonic sampler based on the four wave mixing process in the highly nonlinear fiber [86] to study the preamplified receiver sensitivity improvement.

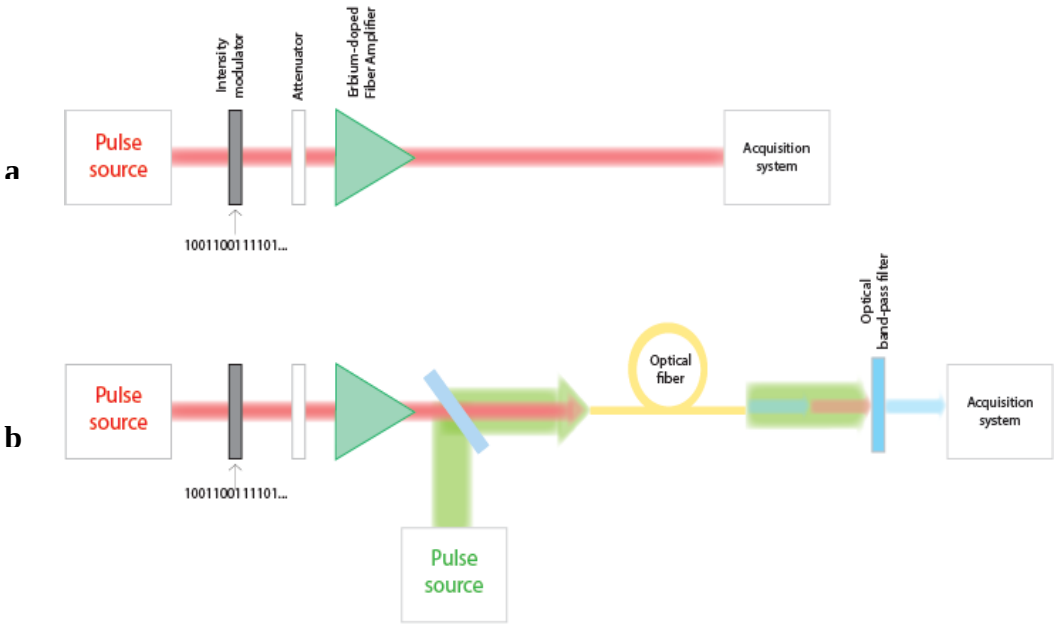

Figure 7.4: Fiber-based experimental setup for few-photon detection. a) Conventional preamplified receiver. The average photon number within the modulated input signal is measured at the amplifier input. b) Photonic sampler aided preamplified receiver. The amplified signal is combined with the sampling pump and parametrically sampled prior to detection.

Figure 7.4 represents the experimental setup employed to confirm the proposed hypothesis. The 1.5 ps-wide signal pulses, centered at 1557.4 nm, are produced by the cavity-less pulse source with 10 GHz repetition rate [62]. This pulse source is divided to create a signal and a sampling pump source. The signal is amplitude modulated with a 2^7-1-long pseudo-random bit sequence and then frequency converted to 1544 nm in the highly nonlinear fiber by means of the four wave mixing process. This HNLF is

characterized by the following global parameters: the fiber length of 182 m, the average zero dispersion wavelength of 1555 nm, the dispersion slope of 0.029 ps/(nm^{2}km) and the nonlinear parameter of 28 W^{-1}km^{-1}. The signal is then attenuated to -46.16 dBm and amplified in an Erbium-doped fiber amplifier. The signal average power is monitored at the EDFA input. The value reported in this measurement correspond to the power before the amplifier front loss. This loss is 0.5 dB, without the splice loss. The filter bandwidth at the amplifier output is varied, having the following values: 0.6 nm, 1 nm, 2 nm, 5 nm and 7 nm.

The amplified pulse is next detected either directly, with a standard telecom receiver, or photonically sampled prior to detection. The photonic sampling is performed in a highly nonlinear fiber by means of the four wave mixing process; the sampling pump pulse, centered at 1557.4 nm, is derived from the same cavity-less pulse source driving the signal. The amplified signal is combined with the sampling pump and guided into the 20 m long highly nonlinear fiber. The generated idler, centered at 1571 nm, is then filtered with a 20 nm filter, to remove the sampling pump and the signal, and detected with a 40 GHz photodiode, followed by a 33 GHz electrical amplifier, a low-pass filter and a real-time oscilloscope. The electrical filter bandwidth is varied at the real-time oscilloscope, having the following set of values: 11 GHz, 20 GHz, 25 GHz, 30 GHz and 33 GHz. The sampling rate of the real-time oscilloscope was set to 100 GS/s and 10^5 points are collected per acquisition, corresponding to 10^4 bits. The reported BER value is averaged over 6 measurements.

The amplified signal is directly detected by the detection system described above. In both the conventional preamplified receiver and the photonic sampler aided

preamlified receiver, we add the polarization beam splitter after the amplifier, to detect a single polarization. The measurement in both cases is performed under the same conditions and the BER value averaged over the identical number of measurements.

The well-known theory [76] of the detector sensitivity dependence on the optical and the electrical filter bandwidth is taken advantage of, to optimize the performance. In doing so, we set the average signal power level at the amplifier input to -46.16 dBm and measure the BER by varying the electrical and the optical filter bandwidth. The BER map is represented in Figure 7.5 for the direct detection and the photonic sampler aided detection.

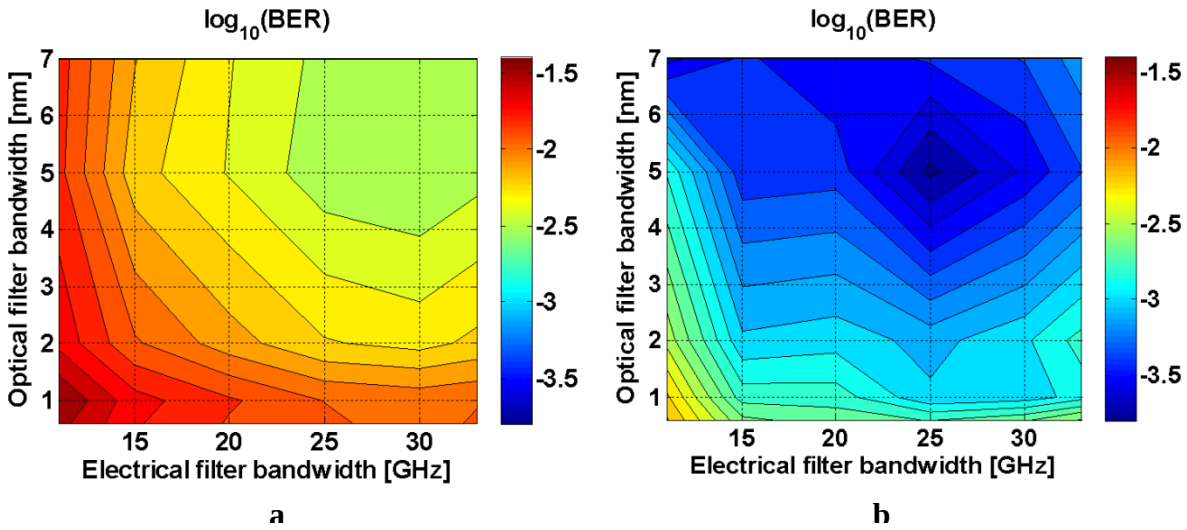

Figure 7.5: Bit Error Ratio as a function of the optical and the electrical filter bandwidth. a) Conventional preamplified receiver. b) Photonic sampler aided preamplified receiver.

As expected, the detailed study reveals the existence of an optimum electrical and an optical filter bandwidth for a direct detection receiver, found to be 30 GHz and 5 nm, respectively, and resulting in the BER of 0.0032. An equivalent measurement for

the photonic sampler aided receiver resulted in an optimum electrical and optical filter bandwidth of 25 GHz and 5 nm, respectively, with BER = 0.00018. As shown in Figure 7.5, the reported measurements fully support the proposed hypothesis: The photonic sampler aided detection resulted in an order of magnitude improvement in the BER compared to the direct detection.

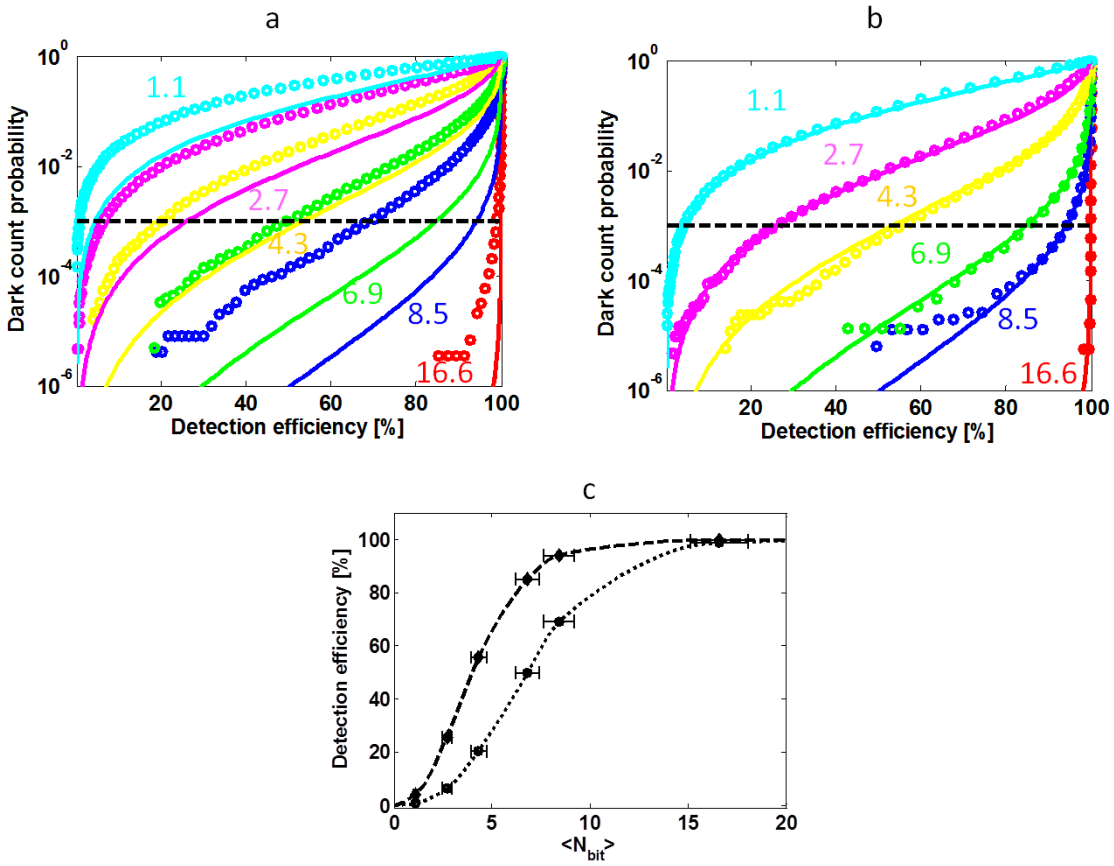

Figure 7.6: Receiver operating characteristics. The receiver performance is evaluated for two cases by measuring the dark count probability as a function of detection efficiency for different average photon number per bit. The measurement is performed by varying the threshold. The number of collected bits is higher than 10^5. The reported average photon number per bit is estimated at the EDFA input and after the front loss. a) Conventional preamplified receiver. Solid curve-Theory; Circles-Experiment. b) Photonic sampler aided preamplified receiver. Solid curve-Theory; Circles-Experiment. c) Detection efficiency versus the average photon number for dark count probability of 0.001. Photonic sampler aided preamplified receiver (dashed curve) and conventional preamplified receiver (dotted curve).

After identifying optimum operating conditions for both systems, we characterize the receiver performance by measuring the ROC curve at a different average photon number per bit. Figure 7.6(a) - Figure 7.6(b) represents the dark count probability, measured as a function of the detection efficiency by varying the detection threshold; the measurement is performed for a different average photon number per bit, at the amplifier input, ranging from 1.1 to 16.6.

In this measurement, the sampling rate was set to 100 GS/s, as in the case of the BER measurement. The number of bits per acquisition was 10^4 and was chosen for computational expediency. Therefore, the ROC curves are assembled by taking multiple single-shot measurements at distinct points in time to increase the total number of points. The total number of points was greater than 10^5.

The average photon number per bit is estimated from the average power. The average power of the PRBS-modulated signal is measured at the EDFA input. The average photon number per bit $<N_{bit}>$ of the classically attenuated signal is calculated with the following equation:

$$< N_{bit} >= \frac{< P > T}{hf} \tag{118}$$

where $<P>$ is the average signal power, T is signal period, h is Planck's constant and f is signal frequency. The average photon number per pulse corresponds to twice the average photon number per bit, with the factor of 2 originating from the PRBS modulation, having the same probability of 0 and 1.

Theoretical curves in Figure 7.6(a) and Figure 7.6(b) are acquired from the known statistical properties of the amplified light [72]. The amplified signal,

corresponding to the binary "one" state, is modeled by the Laguerre distribution; the amplified spontaneous emission, corresponding to the binary "zero" state, is modeled after the Bose-Einstein distribution. In this model, the average photon number per pulse at the amplifier input, after the front loss of 0.5 dB, is 2.1, 5.4, 8.5, 13.5, 17 and 33.2, and these values are used in the experimental model. To decrease the computation time, the amplifier gain is set to 20 dB. Other simulation parameters are as follows: detector quantum efficiency, $\eta = 1$; spontaneous emission parameter, $n_{sp} = 1.35$; and the number of modes, $m = 1$. This parameter set provided good matching of experimental results with theoretical predictions throughout all measurements.

To attain a better insight into the receiver performance, we represent the detection efficiency as a function of the average input photon number for a dark count probability of 0.001; the result is represented in Figure 7.6(c). When the average photon number per bit was set to 1.1, the detection efficiency for the direct detection receiver is 0.7%, while that of the photonic sampler aided detection is almost ten times higher, reaching 4%. Increasing the average photon number the detection efficiency increases, as expected from the amplified light statistical properties; still the photonic sampler aided detection performs better through the entire measurement range.

We note that the photonic sampler role was limited to only removing any noise outside the signal duration window. The sampler design [88] influence on the detector performance is beyond the scope of this work, but is an interesting topic for future studies. Additionally, an important feature of the photonic sampler aided detection is its parallel processing capability at room temperature, therefore supporting an order of magnitude speed increase [89].

In summary, our results prove significant preamplified receiver performance improvement by employing the photonic sampler prior to the detection of the low duty cycle few photon signal with a picosecond duration. This few photon detection method allows for a speed increase well beyond 10 Gb/s, in a temperature-control-free manner, by employing polychromatic sampling [89]. Although the proposed scheme has numerous benefits, it also has an obvious limitation; the fundamental statistical properties of amplified light pose a direct tradeoff between the dark count probability and the detection efficiency. However, it is also easily envisioned how an architecture similar to [89] has potential for additional noise reduction via averaging, therefore allowing further advances. Alternatively, replacing an EDFA with a phase sensitive amplifier [73] can, at least in principle, lead to noise-free amplification. With this novel noise mitigation method, we can pave a way to a new class of photonic sampler aided few photon detectors operating in the previously forbidden regime. This sensitivity improvement technique opens new opportunities in spectroscopy, medical, biomedical and remote sensing applications. Whether this fast photon detection method can satisfy strict requirements for quantum communication applications is still unclear; but if there is such a possibility, pursuing it could have profoundly transformative effects.

Chapter 7, in part or in full is currently being prepared for submission for publication of the material by Ana Pejkic, Daniel. J. Esman, Andreas O. J. Wiberg, Nikola Alic and Stojan Radic. The dissertation author was the primary investigator, and the primary author of this article.

8. Conclusion

8.1. Dissertation summary

Among major concerns in current optical networks are growing demand for wide bandwidth Internet services and ascending Internet traffic. Specifically, the bandwidth-limited electronic backend represents a noteworthy challenge, due to the rising power dissipation with speed increase. Additional concern is information security, a factor that can be detrimental for both corporations and an average Internet user. This dissertation endeavors to address both issues: we employ highly nonlinear fiber mediated photon-photon interaction by means of the four wave mixing process to design an efficient optical signal processing device. First, we revisit the saturated parametric mixer theory to enhance energy exchange among four wave mixing components. Next, we propose the all-optical switch as a high-speed and low-energy alternative to its electronic counterpart. Lastly, we introduce the photonic sampler aided preamplified receiver as a high-speed technique to detect a few-photon picosecond event.

Serving as a foundation of an all-optical switch, a saturated parametric mixer is implemented to mediate energy exchange among interacting waves. We revisit the saturated parametric mixer concept to gain more insight into the phase matched condition guiding the interaction. Recognizing mixer performance dependence on the longitudinal dispersion, we propose a new design, minimizing the pump power in Chapter 4. The design relies on the explicit longitudinal zero-dispersion wavelength

profile, ensuring the phase-matched interaction. However, due to directional phase matching dependence, the saturated parametric mixer response becomes non-reciprocal. The theoretically predicted directional performance variation is experimentally verified in Chapter 5. In this chapter, we characterize the parametric mixer ER and the bandwidth, to predict low energy device capability. These static measurements are used as a guide to design the optical switch. Its ability to switch a Watt-strong pump with only 17 photons within the signal envelope with a 3dB ER is confirmed in Chapter 6.2. Further, the predicted 100 GHz operating speed is experimentally verified, aided with a BER test characterizing the noise performance. The results corroborate error-free operation in a multitude of operating energy ranges, with a minimum of 100 GHz speed.

Finally, Chapter 7 is devoted to investigation of the high speed NIR detection of a few photon picosecond signal with a low duty cycle. Identifying the major noise contribution in the direct preamplified detection, we propose a novel scheme allowing for the noise reduction. The proposed scheme relies on the photonic sampler aided detection, responsible for removing any noise outside the signal duration. The predicted performance enhancement is experimentally validated at a different average photon number; as a performance highlight, we observe a rise in the detection efficiency from 0.7% (for direct detection) to 4% (for photonic sampler aided detection) for an average of 1.1 photon per bit.

8.2. Future directions

This dissertation explores the saturated parametric mixer role in optical switching. In the proposed scheme, the switching event is initiated in a multitude of pump and signal energy ranges with error-free performance. The main limitation is attributed to dispersion induced pulse breakup, limiting the speed to 100 GHz range. In the Chapter 8.2.1 we introduce methods for switch speed enhancement.

The following chapters introduce the phase sensitive amplification and noise averaging mechanisms as noise reduction opportunities in the photonically aided detection. Furthermore, we discuss additional speed increase possibility based on the polychromatic sampling and operation in the short-wave infrared wavelength region as possible research directions.

8.2.1. Optical switch speed enhancement

While a silica fiber is characterized with the sub-femtosecond response time, this fundamental speed limit is typically masked by dispersion effects. Indeed, the higher order fiber dispersion is recognized as a major obstacle to switch speed enhancement, causing a pulse breakup in the described operating regime. Although shortening the fiber length and increasing the peak power can alleviate the problem, this method also increases switch energy consumption. Pump wavelength offset with respect to the ZDW is also recognized as means of performance improvement, but this method additionally reduces the depletion bandwidth. An alternative way to circumvent

the problem is dispersion engineering. Namely, implementing a fiber with uniform dispersion over the wavelength range of interest can, at least in principle, avoid the speed constraint placed by the dispersion properties. In this case, the switch speed is limited by the depletion bandwidth, thus allowing faster operation.

8.2.2. Photonic sampler aided detection: Speed increase

While the work presented in Chapter 7 shows viability of few-photon detection at 10 GHz rate, additional speed increase is always desirable. A scheme offering such a functionality has already been implemented in classical photonic sampling demonstrations [89]. In this work, a polychromatic sampling is proposed as means of speed increase, beyond that determined by the receiver bandwidth.

An order of magnitude speed increase is expected in a similar architecture. N-frequency-shifted- and one-bit-delayed-pumps at low repetition rates can be combined with a preamplified high-speed signal to generate N idlers. The generated idler waves can then be detected independently by an array of N low-speed detectors to reconstruct the incoming signal. This architecture obliges a special care in fiber dispersion engineering, ensuring identical idler conversion efficiency of each generated copy.

8.2.3. Photonic sampler aided detection: Noise reduction methods

While photonically aided preamplified detection has an advantage of high-speed detection and low timing jitter, it is also a subject to some constraints. An obvious

preamplified receiver performance limit is placed by the statistical properties of the amplified light wave. The noise generated in the phase insensitive amplification process places an upper bound to the detection efficiency for a given dark count probability; for a single photon on average and dark count probability of 0.001, the detection efficiency is close to 2%. There are two noise reduction methods offering a possibility of detection efficiency increase:

a) Phase sensitive amplification

b) Noise averaging mechanisms

Phase sensitive amplification

Phase sensitive amplification has been deployed in a number of applications [90], [91], [92], [93], benefiting from its inherent low noise generation. This nearly noiseless amplification mechanism relies on the constructive interference of the phase synchronized signal and idler waves, effectively increasing signal gain by a factor of 4 with respect to phase-insensitive amplification. This also adds additional complexity to the phase-sensitive amplifier (PSA) design: the pump, the signal and the idler phase locking is a necessary step towards the low noise amplification. Fortunately, phase locking is readily achievable [93], thus allowing for an implementation of these devices.

Although, the PSA design has been improved significantly over the years, truly noise-free amplification is difficult to reach. The state-of-the-art PSA [92] was recently demonstrated, reaching the noise figure of 1.1 dB. Whether the photonic sampler aided

PSA preamplified receiver can bring this noise figure closer to the theoretical 0 dB limit, remains to be explored.

Noise averaging mechanisms

White noise averaging method has long been identified as means of detection performance improvement [94]. The technique exploits signal coherence and noise incoherence to extract the weak signal buried in high background noise. By adding two adjacent signal pulses of equal amplitude, the signal adds coherently, while noise adds incoherently, thus increasing the overall detection efficiency. However, in doing so, one also reduces the effective signal repetition rate, a consequence undesirable in many applications. Nevertheless, in medicine, pharmacy, industrial process control or remote sensing, this might be a useful aid in measurement uncertainty reduction.

8.2.4. Parametrically aided detection in the short wave infrared region

Many environmentally, biologically, medically and chemically significant molecules show strong absorption peaks in the short-wave-infrared (SWIR) region (1700 nm - 2100 nm) [95]. However, the SWIR region lacks the efficient detector technology, particularly single-photon detector technology. Indeed, to the best of our knowledge, no commercial photomultiplier or single photon avalanche photodiode technology exist beyond 1700 nm; superconducting single photon detector technology is commercialized, however, its performance is poor compared to the shorter

wavelength range [96]. Additional single photon detection methods relying on the frequency up-conversion have also been reported [97]. To extend the photonically aided detection to this practically important wavelength range, the EDFA can be substituted with the FOPA or Thulium amplifier. The lack of efficient detector in this wavelength band can be circumvented by frequency conversion from the SWIR to NIR in the FOPA and subsequent detection using more efficient NIR technology. Similar method was employed previously to design the SWIR transceiver in the classical regime [98],[99].

In this architecture, the photonic sampler offers few benefits over the direct detection method:

a) It can improve the optimally filtered wave detection in the same manner as described in this work and [98];
b) For the wavelength regions lacking the proper filtering technique (such as SWIR), the photonic sampler role can be extend further. If the noise within the signal duration is uncorrelated, the photonic sampling can be used to average the noise within the signal duration. By taking multiple samples within the signal full-width at the half maximum, and subsequently adding them coherently, the signal adds coherently, while the noise does not, thus effectively enhancing the performance. The maximal number of samples that can be averaged depends on the noise correlation time, typically determined by the optical bandwidth.

Although a significant work remains in efficient FOPA design, offering both distant wavelength translation and sampling, its contribution to efficient few-photon detection is evident.

Appendix A. Error estimation

Power meter used in the experiment was characterized with an error ΔP_{PM} = ± 3%, making the average and peak power error:

$$P_{ave} = P_{PM} \cdot R_{cal} = P_{PM} \frac{P_{cal1}}{P_{cal2}} \tag{119}$$

$$\frac{\Delta P_{ave}}{P_{ave}} = \frac{\Delta P_{PM}}{P_{PM}} + \frac{\Delta R_{cal}}{R_{cal}} = \frac{\Delta P_{PM}}{P_{PM}} + \frac{\Delta P_{cal1}}{P_{cal1}} + \frac{\Delta P_{cal2}}{P_{cal2}} = 0.03 + 0.03 + 0.03 = 0.09 \tag{120}$$

$$P_{peak} = P_{ave} \cdot R_{cal2} = P_{ave} \frac{P_{cal2\_1}}{P_{cal2\_2}} \tag{121}$$

$$\frac{\Delta P_{peak}}{P_{peak}} = \frac{\Delta P_{ave}}{P_{ave}} + \frac{\Delta P_{cal2\_1}}{P_{cal2\_1}} + \frac{\Delta P_{cal2\_2}}{P_{cal2\_2}} = 0.09 + 0.03 + 0.03 = 0.12 \tag{122}$$

$$P_{dBm} = 10\log_{10}(1000 P_W) \tag{123}$$

$$\Delta P_{dB} = 10 \frac{\Delta P_W}{P_W \ln(10)} \tag{124}$$

where P_{ave} is the average power; P_{PM} power meter power reading; R_{cal} calibration power ratio between calibration tap in the signal arm in Figure 6.5 and HNLF input for signal power calibration and calibration tap before the HNLF and HNLF input for pump power calibration; P_{peak} peak power; R_{cal2} calibration power ratio between the peak and the average power. The average number of photons in the signal pulse and the error were estimated using following equations:

$$\frac{\Delta N}{N} = \frac{\Delta P_{ave}}{P_{ave}} = 0.09 \tag{125}$$

The optical sampling oscilloscope was calibrated using CW light centered at 1554 nm. Measured transfer function represented is given by Eq. (121) obtained from the fit.

$$y = 1.1x - 1.6 \tag{126}$$

One method to calibrate peak power is by matching the value of the pulse peak power to the CW reference level using OSO. The ratio of the average power of the pulse and that of the CW reference (corresponding to the peak power of the pulse), labeled as R_{cal2} in the Eq. (116), is used to monitor the peak power. This was experimentally implemented at the calibration point before HNLF as depicted in Figure 6.5, where the average power of the pulse was measured. Additional calibration between the calibration port and the HNLF input was needed to have an accurate estimate of the peak power at the HNLF input.

Bibliography

[1] H. Kragh, "Photon: new light on an old name," *Arxiv: 1401.0293 [physics.hist-ph].*, 2014.

[2] D. Griffiths, Introduction to elementary particles, Wiley, 2008.

[3] M. O. Scully and M. S. Zubairy, Quantum optics, Cambridge University Press, 1997.

[4] [Online]. Available: http://www.maximumpc.com/article/features/12_things_you_didn%E2%80%99t_know_about_eniac.

[5] National Academy of Sciences, Making a world of difference: Engineering ideas into reality, National Academies Press, 2014.

[6] M. Greenstone and A. Looney, "A dozen economic facts about innovation," The Hamilton Project, Brookings Institute, 2011.

[7] H. Moravec, "“Robots” Power and Presence: Numerical Data for the Power Curve, Chap. 3.".

[8] M. P. Mills, "The cloud begins with coal: Big data, big networks, big infrastructure and big power," 2013.

[9] University of California San Diego, "Blackboard learn," [Online]. Available: www.ted.ucsd.edu.

[10] Massachusetts Institute of Technology, "MITOPENCOURSEWARE," [Online]. Available: http://ocw.mit.edu/courses/.

[11] Statista, [Online]. Available: http://www.statista.com/statistics/333861/connected-devices-per-person-in-selected-countries/.

[12] Cisco Systems, "The zettabyte era:trends and analysis," White paper, 2014.

[13] Sandevine, "Global Internet phenomena report," White paper, 2014.

[14] R. W. Tkach, "Scaling Optical Communications for the Next Decade and Beyond," *Bell Labs Technical Journal,* vol. 14, no. 4, pp. 3-10, 2010.

[15] R. J. Essiambre and R. W. Tkach, "Capacity trends and limits of optical communication networks," *Proceedings of the IEEE,* vol. 100, no. 5, pp. 1035-1055, 2012.

[16] E. Temprana, E. Myslivets, B. P.-P. Kuo, L. Liu, V. Ataie, N. Alic and S. Radic, "Overcoming Kerr-induced capacity limit in optical fiber transmission," *Science,* vol. 348, no. 6264, pp. 1445-1448 , 2015.

[17] K. Hinton, J. Baliga, M. Feng, R. Ayre and R. S. Tucker, "Power consumption and energy efficiency in the Internet," *Network, IEEE,* vol. 25, no. 2, pp. 6-12, 2011.

[18] M. P. Mills, "The cloud begins with coal: Big data, big networks, big infrastructure and big power," White paper, 2013.

[19] W. Vereecken, W. Van Heddeghem, M. Deruyck, B. Puype, B. Lannoo, W. Joseph, D. Colle, L. Martens and P. Demeester, "Power consumption in telecommunication networks: overview and reduction strategies," *IEEE Communication Magazine,* vol. 49, p. 62–69, 2011.

[20] G. Koutitas and P. Demestichas, "A review of energy efficiency in telecommunication networks," *Telfor Journal,* vol. 2, no. 1, pp. 2-7, 2010.

[21] R. S. Tucker and K. Hinton, "Energy consumption and energy density in optical and electronic signal processing," *IEEE Photonics Journal,* vol. 3, no. 5, pp. 821-833, 2011.

[22] P. W. Smith, "On the role of photonic switching in future communications systems," *IEEE Circuits and Devices Magazine,* vol. 3, no. 3, pp. 9-14, 1987.

[23] PwC, "Global Economic Crime Survey 2014," White paper, 2014.

[24] PwC, "US cybercrime: rising risks, reduced readiness," White paper, 2014.

[25] T. Beth, "Quantum information processing and communication," 2008.

[26] R. H. Hadfield, "Single-photon detectors for optical quantum information applications," *Nature Photonics,* vol. 3, pp. 696 - 705, 2009.

[27] A. Pejkic, R. R. Nissim, E. Myslivets, A. O. J. Wiberg, N. Alic and S. Radic, "All-optical switching in a highly efficient parametric fiber mixer: design study.," *Optics Express,* vol. 22, no. 19, pp. 23512-23527, 2014.

[28] E. Yüce, G. Ctistis, J. Claudon, E. Dupuy, R. D. Buijs, B. De Ronde, A. P. Mosk, J. M. Gerard and W. L. Vos, "All-optical switching of a microcavity repeated at terahertz rates," *Optics Letters,* vol. 38, no. 3, pp. 374-376, 2013.

[29] T. Volz, A. Reinhard, M. Winger, A. Badolato, K. J. Hennessy, E. L. Hu and A. Imamoglu, "Ultrafast all-optical switching by single photons," *Nature Photonics,* vol. 6, pp. 605-609, 2012.

[30] X. Han, Y. Weng, R. Wang, X. Chen, K. Luo, L. Wu and J. Zhao, "Single photon level ultrafast all-optical switching," *Applied Physics Letters,* vol. 92, p. 151109, 2008.

[31] D. Englund, A. Majumdar, M. Bajcsy, A. Faraon, P. Petroff and J. Vuckovic, "Ultrafast photon-photon interaction in a strongly coupled quantum dot-cavity system," *Physics Review Letters,* vol. 108, p. 093604, 2012.

[32] K. Nozaki, T. Tanabe, A. Shinya, S. Matsuo, T. Sato, H. Taniyama and M. Notomi, "Sub-femtojoule all-optical switching using a photonic crystal nanocavity," *Nature Photonics,* vol. 4, pp. 477-483, 2010.

[33] L. Lengle, M. Gay, A. Bazin, I. Sagnes, R. Braive, P. Monnier, L. Bramerie, T.-N. Nguyen, C. Pareige, R. Madec, J.-C. Simon, R. Raj and F. Raineri, "Fast all-optical 10GB/s NRZ wavelength conversion and power limiting function using hybrid InP on SOI nanocavity," in *ECOC*, 2012.

[34] P. Andrekson, H. Sunnerud, S. Oda, T. Nishitani and J. Yang, "Ultrafast, atto-joule switch using fiber-optic parametric amplifier operated in saturation," *Optics Express,* vol. 16, no. 15, pp. 10956-10961, 2008.

[35] A. Migdall, S. V. Polyakov, J. Fan and J. C. Bien, Single-photon generation and detection, Academic Press, 2013.

[36] C. R. Müller, B. Stoklasa, C. Peuntinger, C. Gabriel, J. Reháček, Z. Hradil, A. Klimov, G. Leuchs, C. Marquardt and L. L. Sánchez-Soto, "Quantum polarization tomography of bright squeezed light," *New journal of Physics,* vol. 14, p. 085002, 2012.

[37] A. I. Lvovsky and M. G. Raymer, "Continuous-variable optical quantum-state tomography," *Review of Modern Physics,* vol. 81, pp. 299-332, 2009.

[38] D. N. Fittinghoff, J. L. Bowie, J. N. Sweetser, R. T. Jennings, M. A. Krumbügel, K. W. DeLong, R. Trebino and I. A. Walmsley, "Measurement of the intensity and phase of ultraweak ultrashort laser pulses," *Optics Letters,* vol. 21, pp. 884-886, 1996.

[39] N. Matsuda, R. Shimizu, Y. Mitsumori, H. Kosaka and K. Edamatsu, "Observation of optical-fibre Kerr nonlinearity at the single-photon level," *Nature Photonics,* vol. 3, pp. 95-98, 2009.

[40] W. J. Munro, K. Nemoto and T. Spille, "Weak nonlinearities: a new route to optical quantum computation," *New Journal of Physics 7, 137 (2005).,* vol. 7, no. 137, 2005.

[41] M. Marklund and P. K. Shukla, "Nonlinear collective effects in photon-photon and photon-plasma interactions," *Reviews of Modern Physics,* vol. 78, no. 2, pp. 591-640, 2006.

[42] Y. R. Shen, Nonlinear Optics, Wiley, 1984.

[43] M. Fox., Optical Properties of Solids, Oxford University Press, 2001.

[44] P. W. Milonni and J. H. Eberly, Laser Physics, Wiley, 2010.

[45] P. N. Butcher and D. Cotter, The Elements of Nonlinear Optics, Cambridge University Press, 1990.

[46] R. W. Boyd, Nonlinear optics, Academic Press, 2008.

[47] E. D. Palik, Handbook of Optical Constants of Solids, Academic Press, 1998.

[48] G. P. Agrawal, Nonlinear Fiber Optics, Academic Press, 2007.

[49] M. E. Marhic, Fiber Optical Parametric Amplifiers, Oscillators and Related Devices, Cambridge University Press, 2008.

[50] E. G. Sauter, Nonlinear optics, Wiley, 1996.

[51] S. K. Das, M. Bock, R. Grunwald, B. Borchers, J. Hytti, G. Steinmeyer, D. Ristau, T. Vockerodt and U. Morgner, "Non-instantaneity of chi3 nonlinear

optical effects," in *Conference on Lasers and Electro-Optics 2012,* 2012.

[52] G. Cappellini and S. Trillo, "Third-order three-wave mixing in single-mode fibers: exact solutions and spatial instability effects," *Journal of the Optical Society of America B,* vol. 8, no. 4, pp. 824-838, 1991.

[53] M. E. Marhic, G. Kalogerakis and L. G. Kazovsky, "Gain reciprocity in fibre optical parametric amplifiers," *Electronics Letters,* vol. 42, no. 9, 2006.

[54] F. Yaman, Q. Lin, S. Radic and G. P. Agrawal, "Impact of dispersion fluctuations on dual-pump fiber-optic parametric amplifiers," *IEEE Photonics Technology Letters,* vol. 16, no. 5, pp. 1292-1294, 2004.

[55] S. Radic, "Parametric amplification and processing in optical fibers," *Laser and Photonics Review,* vol. 2, no. 6, pp. 498-513, 2008.

[56] B. P.-P. Kuo and S. Radic, "Highly nonlinear fiber with dispersive characteristic invariant to fabrication fluctuations," *Optics Express,* vol. 20, no. 7, pp. 7716-7725, 2012.

[57] R. Nissim, A. Pejkic, E. Myslivets, B. P.-P. Kuo, N. Alic and S. Radic, "Ultrafast optical control by few photons in engineered fiber," *Science,* vol. 345, no. 6195, pp. 417-419, 2014.

[58] E. Myslivets, N. Alic and S. Radic, "High resolution measurement of arbitrary-dispersion fibers: dispersion map reconstruction techniques," *Journal of Lightwave Technology,* vol. 28, no. 23, pp. 3478-3487, 2010.

[59] M. Karlsson, "Four-wave mixing in fibers with randomly varying zero-dispersion wavelength," *Journal of the Optical Society of America B,* vol. 15, no. 8, pp. 2269-2275, 1998.

[60] M. E. Marhic, K. K. Y. Wong, M. C. Ho and L. G. Kazovsky, "92% pump depletion in a continuous-wave one-pump fiber optical parametric amplifier," *Optics Letters,* vol. 26, no. 9, pp. 620-622, 2001.

[61] A. Pejkic, R. R. Nissim, E. Myslivets, A. O. J. Wiberg, N. Alic and N. Radic, "A study of a saturated parametric mixer non-reciprocity dependence on the pump wavelength," in *Optical Fiber Communication Conference 2015,* 2015.

[62] A. O. J. Wiberg, L. Liu, Z. Tong, E. Myslivets, V. Ataie, B. P.-P. Kuo, N. Alic and S. Radic, "Photonic preprocessor for analog-to-digital-converter using a cavity-less pulse source," *Optics Express,* vol. 20, no. 26, pp. B419-B427, 2012.

[63] D. J. Esman, A. O. J. Wiberg, E. Temprana, E. Myslivets, B. P.-P. Kuo, N. Alic and S. Radic, "A fully frequency referenced parametric polychromatically sampled analog-to-digital conversion," in *Conference on Optical Fiber Communication,* 2014.

[64] Y. Chen, "Four-wave mixing in optical fibers: exact solution," *Journal of the Optical Society of America B,* vol. 6, no. 11, pp. 1986-1993, 1989.

[65] M. J. Potasek and G. P. Agrawal, "Nonlinear pulse distortion in single-mode optical fibers at the zero-dispersion wavelength," *Physical Review A,* vol. 33, no. 3, pp. 1765-1776, 1986.

[66] P. K. A. Wai, C. R. Menyuk, H. H. Chen and Y. C. Lee, "Effect of axial inhomogeneity on solitons near the zero dispersion point," *Journal of Quantum Electronics,* vol. 24, no. 2, pp. 373-381, 1988.

[67] J. Mandel, The Statistical Analysis of Experimental Data, Dover, 1984.

[68] J. R. Taylor, An Introduction to Error Analysis: The Study of Uncertainties in Physical Measurements, University Science Books, 1997.

[69] R. Slavík, F. Parmigiani, L. Grüner-Nielsen, D. Jakobsen, S. Herstrøm, P. Petropoulos and D. J. Richardson, "Stable and efficient generation of high repetition rate (>160 GHz) subpicosecond optical pulses," *IEEE Photonics Technology Letters,* vol. 23, no. 9, pp. 540-542, 2011.

[70] D. Vukovic, Y. Yu, M. Heuck, S. Ek, N. Kuznetsova, P. Colman, E. Palushani, J. Xu, K. Yvind, L. K. Oxenløwe, J. Mørk and C. Peucheret, "Wavelength conversion of a 9.35 Gb/s RZ-OOK signal in an InP photonic crystal nanocavity," *Photonics Technology Letters,* vol. 26, no. 3, pp. 257-260, 2014.

[71] J. Luo, J. Yu, W. Wanga, J. Guoa, B. Hana and E. Yanga, "All-optical logic NOT gate based on cross phase modulation in highly nonlinear fiber using per-chirped pulse probe," in *Communication and Photonics Conference,* 2010.

[72] E. Desurvire, Erbium-doped fiber amplifiers: principles and applications, Wiley-

Interscience, 2002.

[73] Z. Tong, C. Lundström, P. A. Andrekson, C. J. McKinstrie, M. Karlsson, D. J. Blessing, E. Tipsuwannakul, B. J. Puttnam, H. Toda and L. Grüner-Nielsen, "Towards ultrasensitive optical links enabled by low-noise phase-sensitive amplifiers," *Nature Photonics,* vol. 5, p. 430–436, 2011.

[74] P. L. Voss, R. Tang and P. Kumar, "Measurement of the photon statistics and the noise figure of a fiber-optic parametric amplifier," *Optics Letters,* vol. 28, no. 7, pp. 549-551, 2003.

[75] G. R. Osche, "Optical detection theory for laser applications," Wiley, 2002.

[76] M. Pfennigbauer, M. Pauer, P. J. Winzer and M. M. Strasser, "Performance optimization of optically preamplified receivers for return-to-zero and non return-to-zero coding," *AEU International Journal of Electronics and Communications,* vol. 56, no. 4, pp. 261-267, 2002.

[77] P. J. Winzer and A. Kalmar, "Sensitivity enhancement of optical receivers by impulsive coding," *Journal of lightwave technology,* vol. 17, no. 2, pp. 171-177, 1999.

[78] P. M. Becker, A. A. Olsson and R. J. Simpson, Erbium-Doped Fiber Amplifiers: Fundamentals and Technology, Academic Press, 1999.

[79] H. Sanjoh, K. Tsuzuki and Y. Yoshikuni, "Time-Domain Filtering to Reduce Signal-Spontaneous Beat Noise for a Pulse-Type Multiwavelength Light Source," *IEEE Photonics Technology Letters,* vol. 15, no. 5, pp. 757-759, 2003.

[80] S. Boscolo, S. K. Turitsyn and K. J. Blow, "Time domain all-optical signal processing at a RZ optical receiver," *Optics Express,* vol. 13, no. 16, pp. 6217-6227, 2005.

[81] Y. Chen, B. L. Mark, R. Burnham and H. Verdun, "Reducing ASE Effect in Coherent Detection by Employing Double-Pass Fiber Preamplifier and Time-Domain Filter," *IEEE Journal of Quantum Electronics,* vol. 45, no. 10, pp. 1289-1296, 2009.

[82] S. Boscolo, S. K. Turitsyn and K. J. Blow, "Time domain all-optical signal processing at a RZ optical receiver," *Optics Express,* vol. 13, no. 16, pp. 6217-

6227, 2005.

[83] W. B. Davenport and W. L. Root, "An Introduction to the Theory of Random Signals and Noise," McGraw-Hill Book Company, Inc., 1958, pp. 182-183.

[84] P. W. Juodawlkis, J. C. Twichell, G. E. Betts, J. J. Hargreaves, R. D. Younger, J. L. Wasserma, F. J. O'Donnell, K. G. Ray and R. C. Williamson, "Optically Sampled Analog-to-Digital Converters," *IEEE TRANSACTIONS ON MICROWAVE THEORY AND TECHNIQUES,* vol. 49, no. 10, pp. 1840-1853, 2001.

[85] A. Khilo, S. J. Spector, M. E. Grein, A. H. Nejadmalayeri, C. W. Holzwarth, M. Y. Sander, M. S. Dahlem, M. Y. Peng, M. W. Geis, N. A. DiLello, J. U. Yoon, A. Motamedi, J. S. Orcutt, J. P. Wang, C. M. Sorace-Agaskar, M. A. Popović, J. Sun, G.-R. Zhou, H. Byun, J. Chen, J. L. Hoyt, H. I. Smith, R. J. Ram, M. Perrott, T. M. Lyszczarz, E. P. Ippen and F. X. Kärtner, "Photonic ADC: overcoming the bottleneck of electronic jitter," *OPTICS EXPRESS,* vol. 20, no. 4, pp. 4454-4469, 2012.

[86] A. O. J. Wiberg, C.-S. Brès, B. P.-P. Kuo, J. M. C. Boggio, N. Alic and S. Radic, "Multicast Parametric Synchronous Sampling of 320-Gb/s Return-to-Zero Signal," *IEEE PHOTONICS TECHNOLOGY LETTERS,* vol. 21, no. 21, pp. 1612-1614, 2009.

[87] P. A. Andrekson and M. Westlund, "Nonlinear optical fiber based high resolution all-optical waveform sampling," *Laser and Photonics Reviews,* vol. 1, no. 3, p. 231–248, 2007.

[88] A. O. J. Wiberg, Z. Tong, L. Liu, E. Myslivets, N. Alic and S. Radic, "Chirp optimization of pulsed parametric amplifier," in *Conference on Lasers and Electro-Optics*, San Jose, 2013.

[89] A. O. Wiberg, C.-S. Bres, B. P.-P. Kuo, J. M. Chavez Boggio, N. Alic and S. Radic, "Polychromatic sampling for high-speed real-time processing," in *Optical Fiber Conference*, 2010.

[90] A. Zavatta, J. Fiurasek and M. Bellini, "A high-fidelity noiseless amplifier for quantum light states," *Nature photonics,* vol. 5, pp. 52-56, 2010.

[91] R. Slavík, F. Parmigiani, J. Kakande, C. Lundström, M. Sjödin, P. A. Andrekson, R. Weerasuriya, S. Sygletos, A. D. Ellis, L. Grüner-Nielsen, D. Jakobsen, S.

Herstrøm, R. Phelan, J. O'Gorman, A. Borgis, D. Syvridis, S. Dasgupta, P. Petropoulos and D. J. Richardson, "All-optical phase and amplitude regenerator for next-generation telecommunications systems," *Nature photonics,* vol. 4, pp. 690-695, 2010.

[92] Z. Tong and S. Radic, "Low noise optical amplification and signal processing in parametric devices," *Advances in Optics and Photonics,* vol. 5, no. 3, pp. 318-384, 2013.

[93] L. Liu, Z. Tong, A. O. J. Wiberg, B. P.-P. Kuo, E. Myslivets, N. Alic and S. Radic, "Digital multi-channel stabilization of four-mode phase-sensitive parametric multicasting," *Optics Express,* vol. 22, no. 15, pp. 18379-18388, 2014.

[94] R. N. Donough and A. D. Whalen, Detection of signals in noise, Academic Press, 1995.

[95] M. Ebrahim-Zadeh and ,. I. T. Sorokina, Mid-Infrared Coherent Sources and Applications, Springer, 2008.

[96] "scontel," [Online]. Available: http://www.scontel.ru/sspd/.

[97] G.-L. Shentu, X.-X. Xia, Q.-C. Sun, J. S. Pelc, M. M. Fejer, Q. Zhang and J.-W. Pan, "Upconversion detection near 2 μm at the single photon level," *Optics Letters,* vol. 38, no. 23, pp. 4985-4987, 2013.

[98] F. Gholami, *Band translation to short-wave infrared range: generalized mixer design for sensing,* 2013.

[99] J. M. Chavez Boggio, S. Zlatanovic, F. Gholami, J. M. Aparacio, S. Moro, K. Balch, N. Alic and S. Radic, "Short wavelength infrared frequency conversion in ultra-compact fiber device.," *Optics. Express,* vol. 18, no. 2, pp. 439-445, 2010.